This is to certify that the
dissertation entitled

Temperature Measurement Of Aqueous Ammonium Chloride Solution During Solidification Process Using Laser-Induced Fluorescence

presented by

Mohammad Behshad Shafii

has been accepted towards fulfillment
of the requirements for the

Ph.D. degree in Mechanical Engineering

M. M. Mohseni Kabrani
Major Professor's Signature

Oct. 12, 2005
Date

DATE DUE	DATE DUE	DATE DUE

Temperature Measurement Of Aqueous Ammonium Chloride Solution During Solidification Process Using Laser-Induced Fluorescence

By

Mohammad Behshad Shafii

A DISSERTATION

Submitted to
Michigan State University
in partial fulfillment of the requirements
for the degree of

DOCTOR OF PHILOSOPHY

Department of Mechanical Engineering

2005

ABSTRACT

Temperature Measurement Of Aqueous Ammonium Chloride Solution During Solidification Process Using Laser-Induced Fluorescence

By

Mohammad Behshad Shafii

A wide variety of products are now made of metal alloys. The superior properties of these alloys permit products to be used in very demanding environments where other materials would fail. The major quality issues for these alloys are melt-related defects, such as segregation defects and freckles. Buoyancy-induced fluid flow during solidification, which is primarily responsible for most forms of defects (chimneys), is not directly controllable. If buoyancy-induced fluid flow is left uncontrolled, natural convection will contribute to nonuniform distributions of alloy constituents and grain structure in castings. Materials with acceptable defects can be produced only by trial-and-error and their acceptability is determined by costly inspection. The quantitative measurement of the temperature field during the solidification process will enhance our understanding of the natural convection phenomena, and provide benchmark temperature data valuable to other analytical and numerical studies.

Aqueous ammonium chloride is a popular low temperature analog to metal alloys because of its transparent nature. A two-color laser induced fluorescence (LIF) technique was developed to measure instantaneous whole field temperature distribution above the mushy zone during uni-directional solidification of aqueous ammonium chloride that was cooled from below. The temperature resolution was improved and doubled by using two temperature sensitive dyes having opposite signs in their sensitivity. The fact that the

intensity of one dye increased and the other decreased with decreasing temperature, resulted in a higher temperature sensitivity (4% K^{-1}) in the two-color LIF two-dye approach compared to all previous implementations of the two dye approach (maximum of 1.7% K^{-1}). This was an important outcome of this study.

In this study, in order to understand some of the observed flow features during the solidification processes of the ammonium chloride solution, two different optical diagnostic techniques (PIV and MTV) were used to obtain the velocity fields in these regions.

The temperature mapping relied on the temperature dependence of fluorescence intensity, estimated from the intensity ratio of two temperature sensitive dyes. By using this technique, temperature fields of some of the complex flow features, such as plumes and wisps, were obtained that had not been available before.

Along with the fundamental study based on temperature measurements, a novel technique was also found to enforce the chimney formation at desired locations in the mushy zone during the solidification process of ammonium chloride. This was done by placing metallic nucleators in particular arrangements on the bottom cooling plate. The effects of the arrangement and size of the nucleators on the plume structure and solidification process was investigated. Results showed that it is possible to obtain a relatively large area free of chimneys in the final product of the solidification process by placing the nucleators in certain arrangements. The fact that the flow was calm and the temperature was uniform laterally above this area after t=60 min suggested that the solidification process was taking place uniformly at mush-melt interface, resulting in a better quality of the final product.

This book is dedicated to my mother and father

Mrs. Behnoosh Shafii and Dr. Ahmad Shafii

I want to thank you for always being there for me. You gave me the strength and wisdom to face any obstacle head on and this book was one of them. I LOVE YOU.

ACKNOWLEDGMENTS

I would not have been able to complete this journey without the aid and support of countless people over the past few years.

First of all, I would like to thank my mom (Behnoosh), dad (Ahmad) and sisters (Behnaz, Mahnaz, and Negah) who provided a lot of moral support.

I express my gratitude to my advisor, Dr. Manoochehr Koochesfahani, for his continuous support of my work and for all the hours spent on the improvement of this thesis. Much of the research that is presented here would not have been possible without the encouragement from my supervisor.

I would like to give many thanks to the committee members: Dr. Benard, Dr. Cloud, Dr. Dykman, and Dr. Golding, who gave me quite a few constructive comments on my thesis.

Graduate school isn't the most important thing in life, but good friends, good times and happiness are. I wish to thank my colleagues who provided a lot of technical support and made my time in the PhD program more fun and interesting. This includes Chee Lum, Shahram Pouya, Hu Hui, and Jill Drexler.

Finally, and most importantly, my deepest thanks to my wonderful wife, Parmoon, for all her patience with me and my changing moods. Your support was essential to the completion of my program.

Financial support for this work was provided by NASA grant NAG-8-1690.

TABLE OF CONTENTS

LIST OF FIGURS

Images in this thesis are presented in color

LIST OF TABLES

NOMENCLATURE

Abbreviations

CCD	Charge Coupled Device
DC	Direct Current
DDL	Double-Diffusive Layer
LED	Light Emitting Diode
LIF	Laser Induced Fluorescence
MTV	Molecular Tagging Velocimetry
MTVT	Molecular Tagging Velocimetry and Thermometry
PIV	Particle Image Velocimetry
RMS	Root Mean Square
TC	Thermocouples
TLC	Thermo-Chromic Liquid Crystal

Symbols

b	Length of the sampling volume
C	Concentration
C_{NH4Cl}	Concentration of ammonium chloride
D	Mass diffusivity of the solution
f	Constant in modified Poiseuille equation
Fo	Fourier number ($D \times t/L^2$)
g	gravity

G	Modified Grashof number $G = 2\sqrt{2}(Gr)^{0.25}$
Gr	Grashof number $\left(\frac{g\beta x^3(T_o - T_\infty)}{\nu^2}\right)$
h	Mushy zone height
H	Height of the container
I_o	Incident laser intensity
K	Average permeability of the mush
K_a	Dissociation constant
K_{opt}	Optical constant
K_{spec}	Constant that depends on the physical property of a dye
L	Radius of the source area or Width of the container
Le	Lewis number (α/D)
P	Pressure
Q	Fluorescence quantum yield or Volume flow rate
Ra_H	Rayleigh number based on H, $Ra_H = \frac{Kg\beta H\Delta C}{D\nu}$
r_1	Radius of the chimney
r_2	Radius of the plume when it exits the chimney
S	Signal (number of electrons)
t	Time
T_o	Temperature of the base flow (source)

T_∞	Surrounding temperature
V_r	Velocity in r direction
V_z	Velocity in z direction
x	Distance from the source in the vertical direction
z	Path through which the fluorescence intensity travels
α	Thermal diffusivity or Wave number
β	Temperature sensitivity of a dye
β_C	Solutal expansion coefficients
β_T	Thermal expansion coefficient
ε	Absorption coefficient of the fluorescent dye
μ	Viscosity of the ammonium chloride solution
ρ_B	Bulk density of ammonium chloride solution,
ρ_E	Density of the ammonium chloride solution at the eutectic point
ρ_P	Density of the plume at the exit of the mushy zone
ρ_o	Reference density
ν	Dynamic viscosity
τ	Lifetime
σ_{shot}	Shot noise

Chapter 1

Introduction

A wide variety of products are now made of metal alloys such as automobile engine blocks and the compressor and turbine section of an aircraft engine. These alloys make products strong enough so that they can be used in very demanding environments where other materials would fail. The major issues for these alloys are melt-related defects such as segregation defects and freckles formed during the solidification process. The solidification process of a binary melt can be influenced by fluid motion in the liquid. The solidification of binary alloys from a melt is a process that involves fluid flow and the growth process. As the alloy solidifies, a mushy zone appears at the chilled wall of a mold and a number of phenomena are associated with the formation of this mush. The mushy zone is made of numerous dendrites that constitute a porous network that coarsens as the solidification proceeds. An important feature of solidification in the mushy region pertains to rejection of one of the chemical constituents into the liquid. Solute rejection induces composition gradients which, in combination with existing temperature gradients and a gravitational field, may induce buoyancy driven convection in the mush (plumes) and the parent melt (fingers). As the mushy zone grows, small chimneys are formed, from which discrete plumes of interdendritic melt emerge. These plumes have a very complex flow structure. Since the coupled solid-liquid flow causes structural and chemical inhomogeneities in final solidified products, a fundamental understanding of the multiphase transport phenomena is required. This can be achieved by computing the appropriate conservation laws or, experimentally measuring the

temperature, concentration and velocity fields in the system. Semi-transparent analog alloys have been used for experimental studies because they permit optical access to the sample, which has proven to be useful for flow visualization and morphological studies. Aqueous ammonium chloride is such a system that behaves in a very similar manner to metallic alloys.

Mathematical models developed by Worster (1991), Neilson and Incropera (1991) and Schneider and Beckermann (1995), qualitatively described the temperature and concentration fields in the mushy layer and in the liquid by solving coupled and nonlinear governing equations based on some assumptions, such as two-dimensional flow, axisymmetric conditions, isotropic permeability in the mush, and local thermodynamic equilibrium. Some of these assumptions are too limiting; for example, the plumes have helical motion, therefore assuming two-dimmentional and axisymmetric flow might not be appropriate. As will be discussed later, the system is not in thermodynamic equilibrium at early stages of the solidification process because substantial fluid under-cooling exists above the cooled bottom plate. Instability analysis conducted by Feltham and Worster (1999) showed that a laminar flow in the melt could trigger instability of mush-melt interface by inducing a flow in the porous mush and melt. It was also shown that perturbed heat flux from the melt into the mush-melt interface could cause the growth of instability in the mushy layer. Stability analysis of Heinrich *et al.* (1989) revealed that there are critical container widths, below which convection can be suppressed.

Recent experiments by Chen and Chen (1991) and Magirl and Incropera (1993) suggested that plume convection and chimneys start forming at the liquidus interface due

to the perturbations induced during the transition from finger convection to plumes. Worster (1992) mathematically identified two instability mechanisms: 'Boundary layer' and 'Mushy-layer' modes. In boundary-layer mode the fluid within the interstices of the mushy layer is stagnant and the instability occurs above the mushy layer in the fluid region. Salt-finger convection occurs as a result of this mode and is confined to the compositional boundary layer. The solid fraction does not get perturbed in this mode. The mushy-layer mode is a mode that is related to the solid-fraction perturbations. It was shown that this mode is the cause of the formation of the plumes. These mathematical results can be explored experimentally by embedding nucleators in the cooled bottom plate to cause the channels to form at these approximate locations (will be discussed later). It should be noted that the solutal buoyancy force becomes a dominant factor despite the presence of the stabilizing thermal force. This solutal buoyancy force then causes large-scale convection to be induced in the bulk fluid.

Separate from fundamental issues, some researchers have investigated process-control options to suppress defects formation (such as freckles and chimneys) in unidirectional solidified ingots of binary alloy solutions. Buoyancy forces, which are mainly responsible for the formation of chimneys and freckles, are not easily controllable. Kou *et al.* (1978) performed a numerical analysis, which was confirmed by experiments, to predict macrosegregation in a rotated vacuum arc remelted ingots of Sn-Pb. Due to the upward concavity of the liquidus and solidus interfaces, Pb-rich segregates formed in the center of the ingot. This concavity caused the denser Pb-rich interdendritic liquid to flow downward and radially inward towards the center line. This indicated that during the solidification process there was a remelting of the dendrites, which, in effect,

left a freckle along the center line. Centrifugal forces due to the rotation of the ingot prevented the denser Pb-rich fluid to flow toward the center line creating a more uniform composition profile radially. In fact, they mentioned that by choosing a proper rotational speed of the ingot, the freckles could be significantly reduced. It was also shown that at a high solidification rate, the macrosegregation was slight and centrifugal force had little effect on the macrosegregation.

Sample and Hellawell (1982) showed that the slow rotation of the cylindrical ingot about an inclined axis retarded the formation of chimneys and associated macroscopic composition changes during the solidification process of ammonium chloride solution; however, for higher rotational speeds some chimneys were formed at the mold walls. They concluded that for freckles to form there must be a convective circuit within the bulk liquid and interdendritic liquid, and there must be a flow of more dense solution into the dendritic network around the chimneys to feed the plumes. Therefore, any interruption in this convection circuit could suppress the chimney formation. In another set of experiments, Sample and Hellawell (1984) investigated the mush-melt interface of ammonium chloride that was punctured to various depths by slowly punching a pointed quill into the mushy zone. These artificially created channels failed to propagate and form chimneys and were overgrown and closed within 2 to 4 minutes. However, they could create a new plume, and from that a new chimney, by lowering down an open capillary to within 1 to 2 mm of the growth front and extracting some liquid up the tube. They also observed that blocking an established chimney by a quill could close the chimney and prevent the formation of the plume at that location.

By solving complex and strongly coupled governing equations, Neilson and Incropera (1990, 1993) supported the findings of Sample and Hellawell (1982). They indicated that the quality of unidirectionally solidified binary alloys may be enhanced through an intermittent rotation of the mold, which restricts freckling to the centerline and outer radius of the casting. Experimental observations of Garimella *et al.* (1995) showed that low-amplitude vibration to the test section reduced the mushy zone thickness and the number of chimneys for all concentrations of ammonium chloride solution cooled from below. They also mentioned that the chimneys' suppression was influenced by vibration amplitude rather than by frequency of oscillation.

Since thermal buoyancy force is one of the main forces that plays an important role in the creation of the plumes, it is important to understand and measure the temperature distribution in the solution during the solidification process. Some techniques have been used to carry out temperature measurements during the solidification process of ammonium chloride.

Thermochromic liquid crystal paints (TLC) used in a Hele-Shaw cell (Solomon and Hartley 1997) enabled simultaneous visualization of temperature field at the walls and the solid fraction in Hele-Shaw cells based on the assumption that the painted TLC on the walls responded to the flow in the interior due to the rapid diffusion of heat across the narrow gap. They visualized isotherms both within the mushy layer and in the liquid region. Distortions in these isotherms revealed flows in the system. Other temperature measurements have been done by thermocouples. Measured temperature histories on the test section midline at selected heights (Magirl and Incropera 1993) and at the side wall

(Wirtz *et al.* 1998) could reveal consistent decay in local temperature, with pronounced decay occurring at the location closest to the chill plate.

Past experimental, analytical and numerical studies have established that the convective phenomena present can best be described in terms of complex dynamic velocity fields. Most experimental methods applied to date have been poorly suited to accurately measure these phenomena and do not provide for whole-field measurements of the 2-D temperature distribution. The temperature measurement carried out by Solomon and Hartley (1997) using TLC paints was in the Hele-Shaw cells, in which one of the side walls was coated with TLC. The measured temperature was not the actual temperature of the fluid due to the fact that the fluid is motionless along the sidewalls. In addition, the convection phenomenon and the plume structure are different in Hele-Shaw cells compared to those in conventional size containers due to the fact that flow between closely-spaced parallel plates is affected by wall drag.

This work is the continuation of the work done by Wirtz (1998) and Lum *et al.* (2001) who obtained velocity vectors in the ammonium chloride solution during its solidification process using a molecular tagging velocimetry (MTV) technique. This current work can be divided into two main goals.

The primary goal of this work was to develop a diagnostic technique to obtain temperature maps of the ammonium chloride solution during its solidification process. Laser induced fluorescence (LIF) technique was selected to obtain instantaneous two-dimensional temperature maps of the whole solution. The use of LIF provides verification of the modeling approaches of some of the previous work, provides benchmark temperature field data valuable to other analytical and numerical studies, and

enhances our understanding of thermosolutal convection processes. Since some of the flow features such as plumes and wisps have small temperature difference across them, the temperature sensitivity of the LIF technique was improved upon for the first time by choosing two temperature sensitive dyes. The detailed temperature fields quantitatively characterizing the complex structures previously observed in such solidification will be valuable relative to the development and refinement of numerical models. The energy equation was simplified and solved numerically based on some assumptions and appropriate boundary conditions (obtained from measurements) to obtain temperature fields of a plume.

The secondary goal of this work was to investigate the effects of the arrangement and the size of the nucleators on the plume structure and solidification process. Nucleators are small metallic blocks that are placed on the bottom cooling plate. Wirtz (1998) showed that plumes could be forced to form above the nucleators for one particular arrangement. The LIF technique was used to obtain temperature fields of some of the interesting flow features for some of the nucleators' arrangements. To obtain velocity fields and profiles, particle image velocimetry (PIV) and molecular tagging velocimetry (MTV) were also used.

In the upcoming chapters of this work, the experimental methodology of the solidification process of the ammonium chloride solution will be discussed. Different diagnostic techniques for velocity and temperature measurements will be explained. The LIF technique including dye selection and spectral conflicts will be discussed. In later chapters, the effect of the size and the arrangements of the nucleators on the solidification

process will be detailed and some of the temperature and velocity fields of the interesting features of the flow will be presented.

Chapter 2

Methodology of the solidification process

In this chapter the phase diagram of aqueous ammonium chloride will be described, the variation of the pH of the ammonium chloride solution with percent weight of ammonium chloride will be presented (needs to be known for the LIF technique) and the experimental methodology of the solidification process will be detailed.

2.1 Ammonium chloride characteristics

Ammonium chloride is a popular low temperature analog due to the transparent nature of the fluid. Also, the temperature range at which solidification occurs provides a means for studying the convective mechanisms present in s solidifying system.

The equilibrium diagram for ammonium chloride is shown in Figure 2-1, where the dashed lines indicate the initial concentration and the final equilibrium temperature of the aqueous ammonium chloride, while the dot above the liquidus line indicates the initial starting conditions used for all experiments in this study (26% wt). The aqueous ammonium chloride solution was initially kept at 23°C. When the temperature at the bottom plate reaches the liquidus temperature (18.6° C), which is determined by the composition of the salt solution (26% wt), ammonium chloride crystals begin to form and continue growing as cooling progresses. The process will continue along the liquidus line, which implies that as the fluid gets cooler, ammonium chloride crystals precipitate out of the solution forming a mushy zone since the weight percentage of the fluid must

reduce to maintain equilibrium. The mushy zone is composed of solid dendrites and interdentritic liquid, and it separates fully solidified and liquid regions during solidification. The permeability of the mushy zone is non-uniform and anisotropic. The mushy zone is commonly treated as a porous medium. The eutectic region is a mixture of both ice and ammonium chloride and it is in solid form.

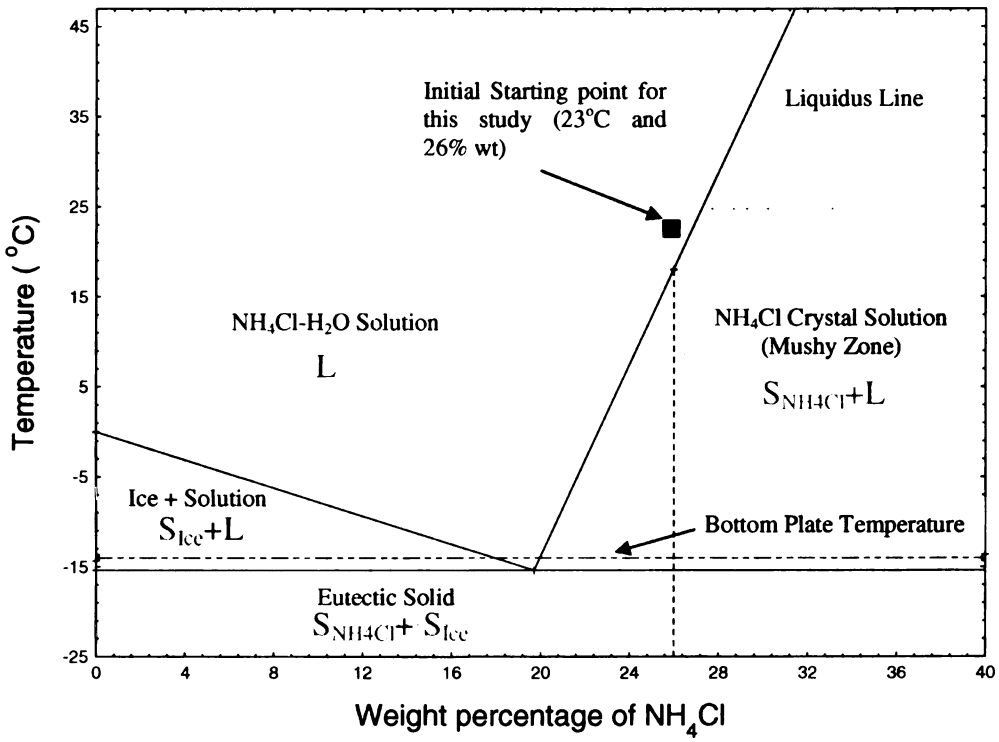

Figure 2-1: Equilibrium diagram of ammonium chloride

Since the fluorescence intensity of some dyes is greatly affected by pH variation (this will be discussed later), the pH of the ammonium chloride solution needs to be known prior to the test. Figure 2-2 shows the pH variation of ammonium chloride solution as a function of percent weight of ammonium chloride dissolved in the solution.

Measurement of pH was carried out by continuously adding a known amount of ammonium chloride to the distilled water with initial pH of seven and measuring the pH values with a pH meter (Omega PHH-12, accuracy of ± 0.05 pH). The final pH value of 26% wt ammonium chloride solution is about 4.3 pH. The lack of data points between pH 5 and 7 occurs because of the high sensitivity of the pH to the percent weight of ammonium chloride in this range.

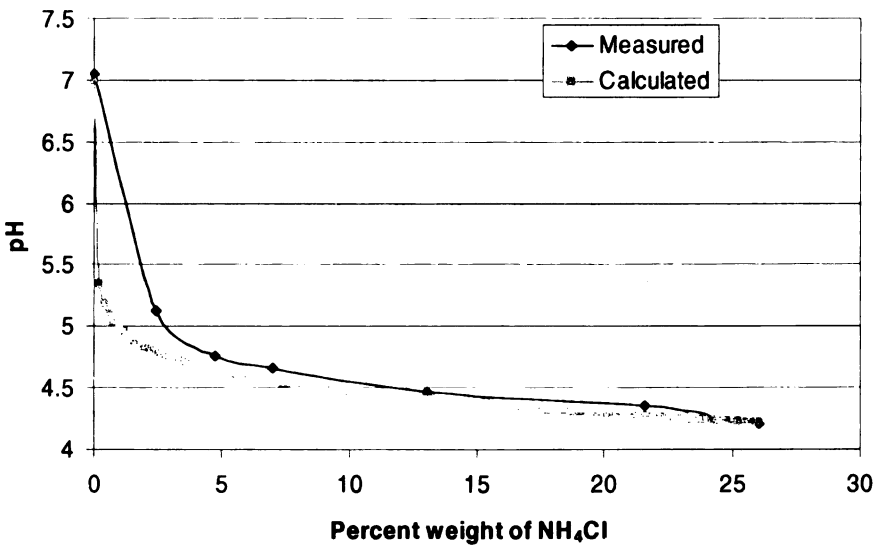

Figure 2-2: Measured pH of the solution as a function of percent weight of NH_4Cl

The pH of the solution can also be calculated (shown by red squares) from the following equations:

$$[H^+] = \sqrt{K_a \times C_{NH_4Cl}} \qquad (2\text{-}1)$$

$$pH = -\mathrm{Log}_{10}([H+]) \qquad (2\text{-}2)$$

where K_a is the dissociation constant and C_{NH4Cl} is the concentration of ammonium chloride in the solution in mol/lit. The value of the dissociation constant for ammonium chloride is 5.56×10^{-10}. Since the temperature of the solution changes during the solidification process, it is important to know the pH variation of the solution with temperature.

The variation of the pH of 19% wt ammonium chloride solution with temperature is shown in Figure 2-3. pH is normalized by pH_o. pH_o is the pH of the solution at room temperature (20° C) and is equal to 4.4 for 19% wt of the ammonium chloride solution. It should be noted that 19% wt ammonium chloride was used in order to avoid crystal formation of ammonium chloride during the calibration process. It can be seen that the pH increases slightly as the temperature decreases. This variation is related to the fact that the dissociation constant of ammonium chloride is slightly temperature dependent. Since the pH of the solution is slightly temperature dependent, a fluorescent dye should be chosen such that the emission intensity of the dye does not change with variation in pH. This will be described in the following chapters.

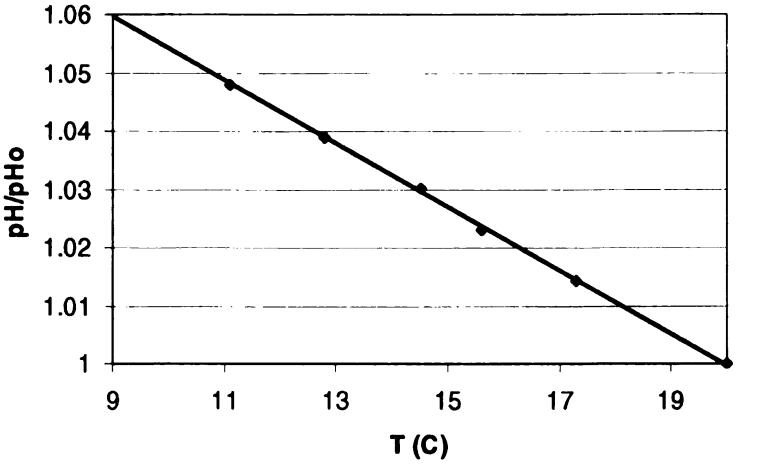

Figure 2-3: Measured pH variation of ammonium chloride solution with temperature

2.2 A description of the Solidification of ammonium chloride in water

This temperature measurement work is the continuation of the work done by Wirtz (1998) and Lum *et al.* (2001) who obtained velocity vectors in the ammonium chloride solution during its solidification process. A schematic of the container used to conduct experiments is shown in Figure 2-4. The solidification system utilized is exactly the same as the one described in Lum *et al* (2001).

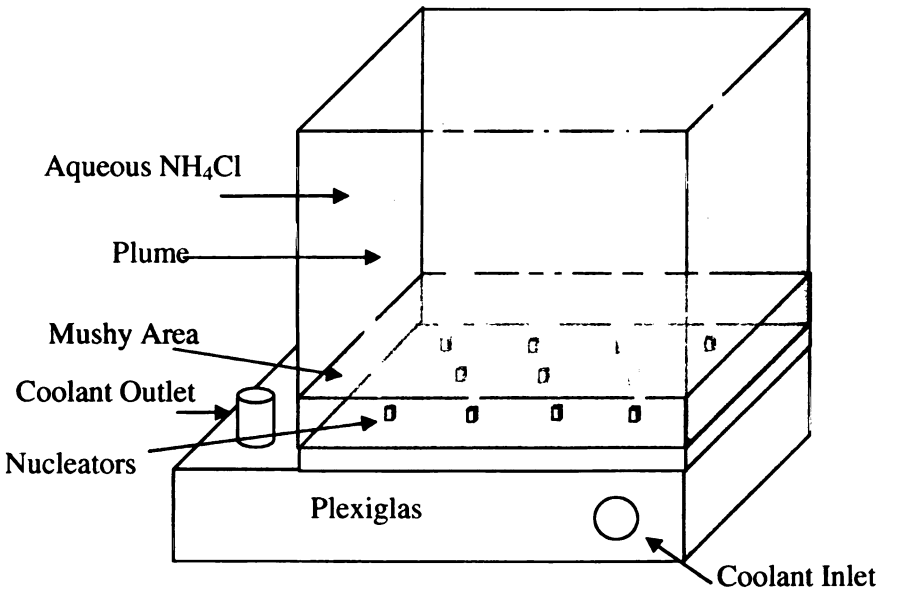

Figure 2-4: Schematic of the container

The cooling of the fluid in the container is achieved through the use of a base stainless steel plate as a heat transfer medium, which is exposed to a coolant bath on one side to provide for the cooling and aqueous ammonium chloride on the other side within the test section. An enclosure made of 1/4" quartz glass measuring 52 × 89 ×100 mm is

placed over the stainless steel base plate and sealed with high vacuum grease and gaskets to form the test section. Quartz glass is used due to the fact that it absorbs very little of the laser energy and thus is suitable for the transmission of laser beams in two-color LIF technique and results in less attenuation.

During initial experimental trials, Wirtz (1998) observed that convective plumes caused by the instabilities developed within the test section in a random manner. However, each experimental trial would yield approximately 11 chimneys within the test section. Eleven square nucleators were embedded in a regular manner in the base stainless steel plate to induce finite disturbances to the formation of the mush (Wirtz 1998). These nucleators would cause the channels to form at those approximate locations. A schematic of the stainless steel plate and the coordinates of the stainless steel nucleators are provided in Figure 2-5. This resulted in the formation of many ascending water-rich fingers and the formation of ammonium chloride crystals, which would form on the bottom of the test section to make up the mushy region.

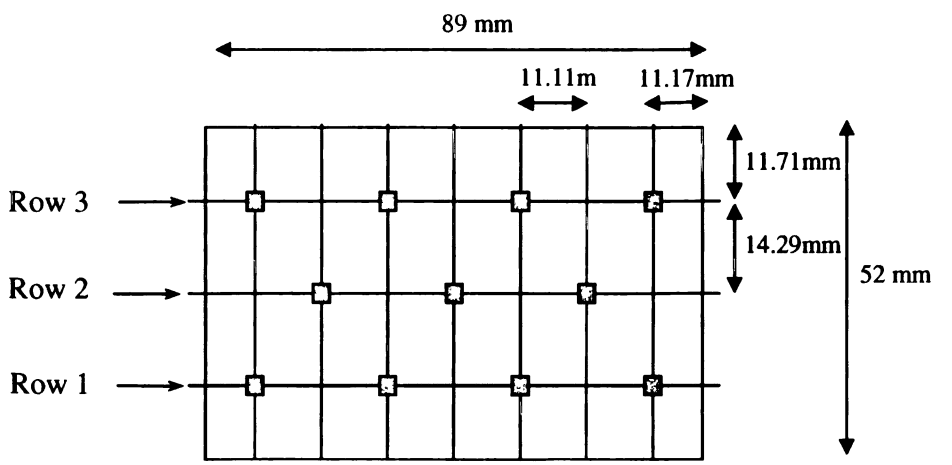

Figure 2-5: Schematic of the stainless steel plate

After the ammonium chloride solution was poured into the container (26% wt NH_4Cl), it was cooled from the bottom by means of a heat exchanger. The thermobath circulated constant temperature coolant (-19°C) through the cooling chamber and this caused the base stainless steel plate to be at a constant temperature of -14°C. The cooling fluid is a 50% mix of water and generic automotive anti-freeze (ethylene glycol), which was refrigerated by this thermobath (Neslab, RTE-140) and pumped through insulated tubing into the cooling chamber. To reduce the heat transfer to the surroundings, the cooling chamber was covered with appropriate insulations. The cooling provided to the test section would then initiate the crystallization process. Rapid growth of the mushy layer at the initial stages of cooling indicated the presence of substantial fluid under-cooling (temperature of the fluid with known concentration is below liquidus line shown in Figure 2-1). The proof of the existence of sub-cooled fluid will be presented later. As seen in Figure 2-6, which was obtained by Lum (2001) using a shadowgraph technique, four minutes into the solidification process, small fingers started to form around the nucleators and could be seen rising. At 6 minutes, more fingers maintained their solutal identity and were able to rise higher. Due to the large Lewis number of ammonium chloride, the water-rich fingers retained their compositional identity and were clearly visible to the top of the test section before they would begin to collapse (Magirl and Incropera 1993). The Lewis number is a measure of the ratio between characteristic lengths for diffusion of heat and diffusion of mass and can be defined as:

$$Le = \alpha / D \qquad (2\text{-}3)$$

where α is the thermal diffusivity and D is the mass diffusivity of the solution. The time when plumes are first formed is difficult to determine since this transition from fingers to plumes is continuous. Fingers are defined as plumes when they become more vigorous and their size is perceptibly larger than their surrounding neighboring fingers. This evolution of plumes usually start after 13 min into the process. Initially, there were 2 or 3 plumes and later the number of plumes increased. As neighboring plumes competed for the supply of water-rich fluid from within the mush, surrounding fingers started to decrease in quantity. At around 20 minutes, it became apparent that the plumes were developing above the nucleation sites. Most of the time 11 plumes were formed right above the 11 nucleators. This is consistent with the mathematical results obtained by Worster (1992) about mushy-layer instability mode. It was shown that this mode is the cause of the formation of the plumes. This instability mode happens when the solid fraction is perturbed. These nucleators located on the bottom plate below the mushy layer perturbed the solid fraction and from the consequence of that, the plumes were formed above these nucleators. As the salt-rich fluid adjacent to a plume was cooled, it descended as a sheath along the plume. These sheaths could not traverse the plume bends, causing these sheaths to separate from the plume (wisps) and descended freely (Figure 2-7). Other observed regions were the double-diffusive layers shown in Figure 2-7. Double diffusive layers were formed about 90 min into the process. These layers are diffusive interfaces, which are slightly inclined from horizontal due to the vertical motion of the plume. The formation of double diffusive layers (DDL) is a result of the interaction between the vertical concentration gradient and the horizontal temperature gradient (Appendix A), both induced by plume convection (Chen 1997).

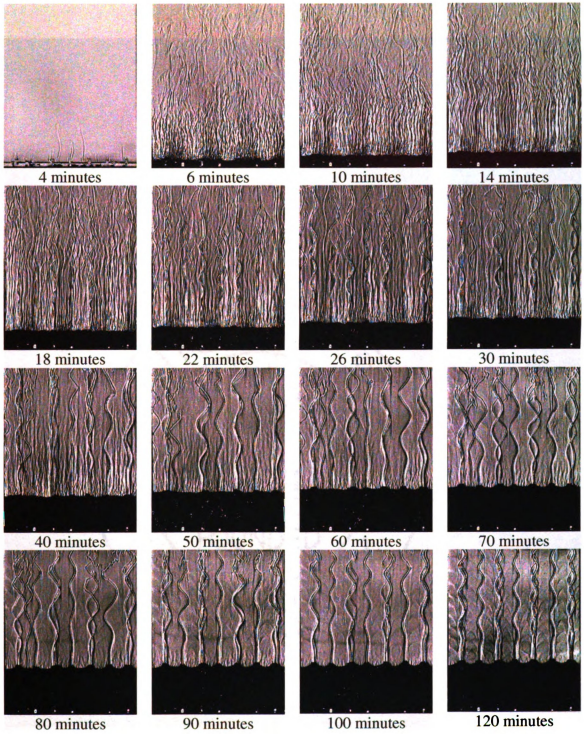

Figure 2-6: Visualization of solidification process at different times (Lum *et al.* 2001)

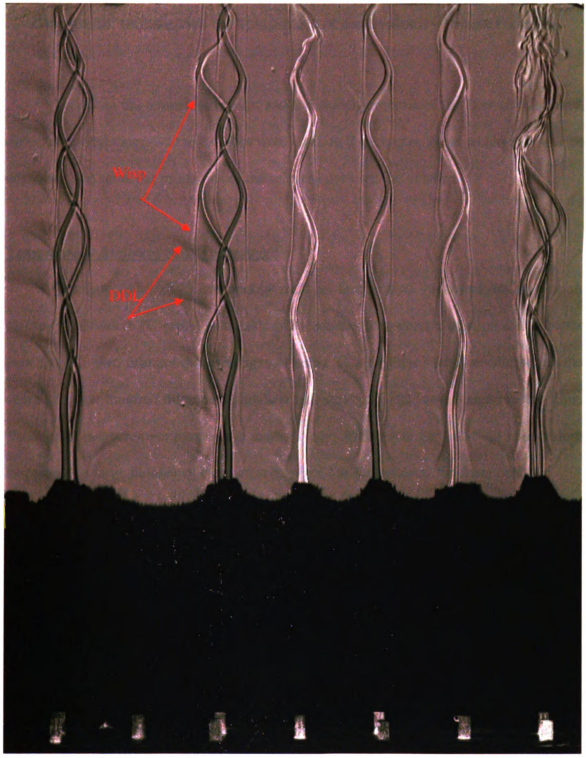

Figure 2-7: Shadowgraph image of plumes and the described wisps and DDLs

Chapter 3

Diagnostic techniques for temperature and velocity measurements

To obtain the temperature maps and the velocity vectors of the flow in this study, different optical diagnostic techniques were used. In this chapter, these techniques will be described and some the properties of the selected dyes will be detailed.

Temperature Measurement Techniques

Thermocouples (TC) are widely used as temperature measurement probes. A carefully calibrated TC probe is capable of measuring temperature with precision better than ± 0.1K. Two primary disadvantages of using TCs are their spatial resolution, on the order of a few hundred microns at smallest and their physical intrusiveness in the flow. Their point measurement nature also makes it very difficult to get full-field temperature mapping as a large number of them must be placed and monitored simultaneously.

Thermo-chromic liquid crystal (TLC) materials have been used as a nonintrusive tool for full-field, temperature measurement. The TLC-based technique is based on the optical properties of TLC materials. At the heart of LC based thermography systems are liquid crystal materials called thermochromic liquid crystals (TLCs). Fundamentally, a liquid crystal is a thermodynamic phase that is between the pure solid and pure liquid phases of matter and exists in some organic compounds under certain conditions. At temperatures below the TLC's event temperature, a TLC will be in the solid state and will appear transparent. When a TLC is at its event temperature, illuminated by white light and viewed under fixed optical conditions, the TLC material will reflect a unique

wavelength of visible light (i.e., color). As the temperature rises through the TLC's bandwidth, the reflected color of the TLC will change. Finally, when the temperature exceeds the TLC's clearing point temperature, the material will enter the pure liquid state and will revert back to being transparent. The molecular structure of a TLC gives the material two indices of refraction, causing the material to become birefringent. Birefringence will cause the selectively reflected light emerging from a TLC to become elliptically polarized. The reflected color spectrum for most TLC materials will vary continuously from the longer wavelengths (i.e., red) corresponding to the event temperature to shorter wavelengths (i.e., blue) corresponding to the clearing point temperature. Additionally, a TLC material will also transmit a significant amount of the incident light with virtually no modification. Viewing TLCs against a non-reflecting (i.e., black background prevents this transmitted light from adversely affecting the interpretation of the selectively reflected light. By knowing the relationship between the reflected color and the temperature, one can obtain the full-field, temperature map. The major shortcoming in using TLC is that one has to calibrate each point of test section to take into account the influence of the illuminating light variation. Since the color of the TLC may also depend on the viewing angle and the location of the tested area, the temperature calibration has to be repeated each time the CCD camera is displaced. The TLC materials can be made in the form of microencapsulated liquid and used as tracer particles in flow visualization. In our experiment, microencapsulated TLC materials are difficult to use in whole field temperature measurement since the calibration of TLC is challenging prior to the test (due to the solidification of ammonium chloride and also due to continuous change of index of refraction of the fluid). As will be shown later in PIV

measurements section, another problem that one might encounter using these microencapsulated TLC particles is that, as they penetrate in mushy zone they become nucleation sites and crystals form around them. This can change the mushy zone structure and causes lack of TLC particles in some flow structure.

The Laser Induced Fluorescence (LIF) technique is based on fluorescence of molecules and atoms, which is induced by absorption of a photon. This absorption causes a transition from ground state to an excited state. Part of the absorbed energy is released as re-emitted light (fluorescence) during spontaneous transition from the excited state to the ground state. The fluorescence occurs at a longer wavelength than that of the absorption. LIF technique has been widely used for both flow visualization and scalar measurements (concentration and temperature) of fluid flows in recent years (Koochesfahani and Dimotakis 1985; Koochesfahani *et al.* 2000, and Sakakibara and Adrian 1999). If the fluorescence intensity of a dye is temperature dependent, fluorescence intensity of known concentration of the fluorescent dye can be calibrated versus temperature. This calibration curve can be used to obtain a temperature map in the imaged area (Kim and Kihm 2001). In the next sections the LIF technique will be explained in detail and some difficulties associated with the inherent spectral conflicts will be discussed.

3.1 Laser Induced Fluorescence (LIF)

When the laser beam passes through a liquid medium seeded with an organic fluorescent dye, the fluorescence intensity is affected by the absorption of the incident laser beam and by the re-absorption of the fluorescence itself across the absorbing

medium. According to Beer's law, the expression for the fluorescence signal captured by camera can be expressed as

$$I_f = K_{opt}\varepsilon_1 QCI_o e^{-C(\varepsilon_1 b+\varepsilon_2 z)} \quad (3\text{-}1)$$

where K_{opt} is an optical constant, C is the molecular concentration of the fluorescent dye, ε_1 is absorption coefficient of the fluorescent dye when it is exposed to a laser and b is the length of the sampling volume along the path of the excitation beam. ε_2 is the absorption coefficient of the fluorescent dye when it is exposed to its own emission light and z is the path through which the fluorescence intensity travels in the solution and gets reabsorbed by the dye, I_o is the incident laser intensity, and Q is the fluorescence quantum yield. If the concentration is low enough, the above equation can be rewritten as

$$I_f = K_{opt}\varepsilon_1 QCI_o \quad (3\text{-}2)$$

Both the absorption coefficient ε_1 and quantum yield Q can be temperature dependent.

Lemoine *et al.* (1999) used an equation for fluorescence quantum yield based on the A_{21} spontaneous emission Einstein coefficient and presented the following equations:

$$Q = K_{spec} e^{\beta/T} \quad (3\text{-}3)$$

substituting (3-3) in (3-2) results in

$$I_f = K_{opt} K_{spec} I_o C e^{\beta/T} \quad (3\text{-}4)$$

where K_{spec} depends on the spectroscopic and physical property of the dye and constant β is the temperature sensitivity of the dye that can be found during the calibration process. The LIF technique can be applied in two different ways, one-color LIF technique and two-color LIF technique (known as ratiometric method), as described below.

One-color LIF technique

In one-color LIF, only one color band of the emission spectrum of a temperature sensitive dye is used to measure temperature (Figure 3-1).

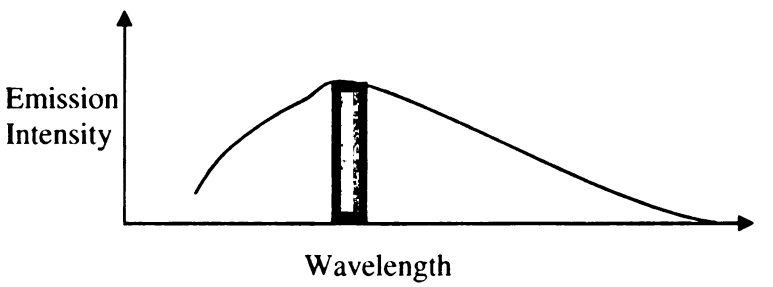

Figure 3-1: Emission spectrum of one dye with one color band (high lighted as green).

Equation (3-4) can be presented in terms of intensity ratio. Assuming laser intensity I_o and molecular concentration of the fluorescent dye to be constant, equation (3-4) can be rewritten as

$$\ln\left(\frac{I_f(T)}{I_f(T_o)}\right) = \beta\left(\frac{1}{T} - \frac{1}{T_o}\right) \qquad (3\text{-}5)$$

where T_o is the reference temperature and $I_f(T_o)$ is fluorescence intensity at reference temperature. This equation is the base equation for temperature measurement of one-color LIF technique (Lemoine *et al.* 1999). The drawback of using the one-color LIF technique is that it is very difficult to maintain the incident laser intensity uniform throughout the process. During the solidification process of ammonium chloride the index of refraction of fluid continuously changes resulting in non-uniform unsteady laser illumination field and inaccurate temperature measurements. Examples of inaccurate temperature maps will be displayed later.

Two-color LIF technique

The two-color LIF technique can be used to eliminate the effect of laser intensity variation in the system. In this technique two color bands are chosen. These two color bands can be chosen either from emission spectra of two fluorescence dyes (two-color LIF two-dye approach, Figure 3-2 a), or from emission spectrum of one dye at different locations on its emission spectrum (two-color LIF one-dye approach, Figure 3-2 b). These color bands should usually be chosen such that the intensity of one is temperature sensitive and the other temperature insensitive (Sakakibara and Adrian 1999). The fluorescence signal of temperature sensitive dye provides the temperature distribution in the measurement region and that of the temperature insensitive dye provides the intensity distribution of the incident illumination laser light. As will be described later, for the purpose of this research, two temperature sensitive dyes (with opposite temperature dependency) are used to increase the temperature sensitivity and also take into account the non-uniformity of the illumination light.

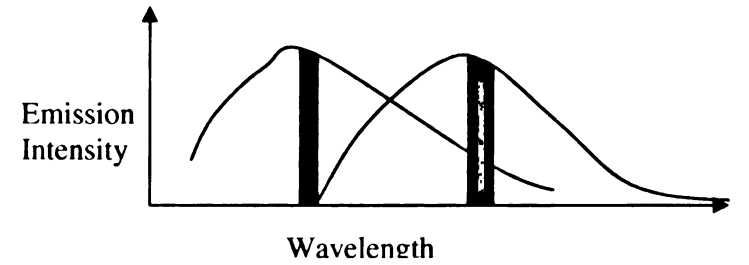

(a)

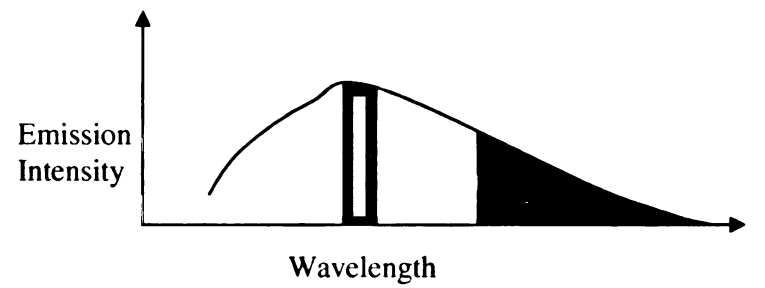

(b)

Figure 3-2: Two color LIF technique. (a) two-color two-dye, (b) two-color one-dye (the two color bans are shown as green and red regions)

If two color bands are detected by two aligned cameras, the fluorescence signal detected on the first color band may be written as in equation (3-6)

$$I_{f1} = K_{opt1} K_{spec1} I_o C_1 e^{\beta_1 / T} \qquad \textbf{(3-6)}$$

and on the second one

$$I_{f2} = K_{opt2} K_{spec2} I_o C_2 e^{\beta_2/T} \tag{3-7}$$

the fluorescence ratio can be written as

$$R_f = \frac{I_{f1}}{I_{f2}} = \frac{K_{opt1} K_{spec1}}{K_{opt2} K_{spec2}} \frac{C_1}{C_2} e^{\frac{(\beta_1 - \beta_2)}{T}} \tag{3-8}$$

C_1 is equal to C_2 when two color bands are chosen from the emission spectrum of one dye (two-color LIF one-dye approach). To eliminate K_{opt}, K_{spec} and C a reference temperature T_o needs to be defined. By knowing T_o and corresponding fluorescence intensity ratio, one can modify the equation (3-8) to obtain

$$\frac{R_f(T)}{R_f(T_o)} = e^{\frac{(\beta_1 - \beta_2)}{T} - \frac{(\beta_1 - \beta_2)}{T_o}} \tag{3-9}$$

or

$$\ln\left(\frac{R_f(T)}{R_f(T_o)}\right) = (\beta_1 - \beta_2)\left(\frac{1}{T} - \frac{1}{T_o}\right) \tag{3-10}$$

The value of $(\beta_1-\beta_2)$ can be calculated from the calibration curve and it is desired to be as large as possible. The larger this number is, the more sensitive the ratio intensity becomes to temperature variation. The advantage of using two-color LIF one-dye approach is that, even if the concentration of the dye changes during the process, equations (3-9) and (3-

10) are still valid because the ratio of C_1 over C_2 is always 1. This might not be true for two-color LIF two-dye approach. If, during the process, the concentration of one of the dyes changes locally, then the ratio of C_1 over C_2 is no longer constant and equations (3-9) and (3-10) are not valid. The other advantage of two-color LIF one-dye approach, as shown in equation (3-1), is that if a low concentration of the dye is used then there is no need to be concerned about the spectral conflicts (will be explained later). A main difficulty in this approach is finding a dye which has two color bands on its emission spectrum: one sensitive and the other insensitive to temperature variation. Usually when a dye is temperature sensitive all color bands on its emission spectrum are temperature sensitive.

3.1.1 Dye selection in two-color LIF one-dye approach

In order to find out if this approach could be used to measure temperature of the solution during the solidification process, Rhodamine B was selected and tested as a temperature sensitive dye for this approach. Rhodamine B is a useful dye because its fluorescence is not pH dependent (over pH ranges above 6), but is temperature dependent. Experimental results obtained by Coppeta and Rogers (1998) indicated that Rhodamine B is one of the most temperature quenched dyes and over a temperature range of 0-60 ^{o}C the fluorescence intensity changes by approximately –1.54% per degree Celsius. Figure 3-3 shows the variation of the emission spectrum of Rhodamine B, dissolved in ammonium chloride solution, with temperature. The emission spectrums of all dyes presented in this paper were obtained by using a spectrophotometer (Hitachi 4500) located in Michigan State University's (MSU) Chemistry department.

Figure 3-4 shows the variation of the average normalized intensity of Rhodamine B solution with temperature for different color bands of the emission spectrum (computed from Figure 3-3). I_o is the intensity at a reference temperature, usually at ambient temperature (20°C). It can be seen that for the color band that is in the 670-700 nm range normalized intensity is less sensitive to temperature variation (minimum slope) and the color band 575-585 nm maximum sensitivity (maximum slope) will be obtained.

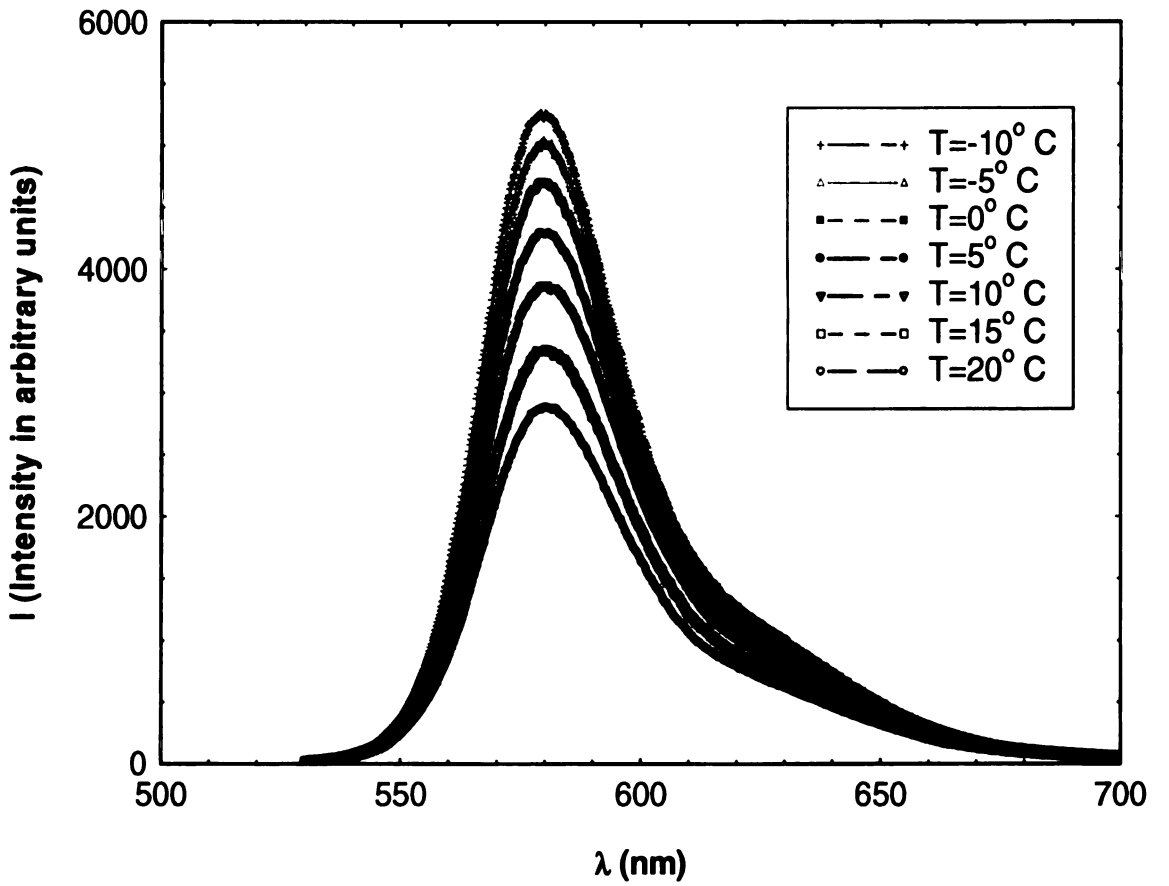

Figure 3-3: Emission spectra of Rhodamine B
Solution of: 5×10^{-6} mol/lit Rhodamine B and 19% wt NH_4Cl (excitation=488 nm)

Using a single dye such as Rhodamine B in a two-color LIF one dye approach resulted in poor temperature sensitivity. For example if two color bands are chosen, one 575-585 nm (high temperature sensitive band) and the other one 670-700 nm (low temperature sensitive band), taking the ratio of these normalized intensity bands results in a low temperature sensitivity curve (at best 0.33% change in normalized intensity ratio per degree C). It means that a 1°C temperature variation corresponds to about 0.33% variation in the normalized fluorescence ratio. Therefore, a two-color LIF two-dye approach needs to be considered instead. To do so, two appropriate dyes need to be selected. In order to select two dyes, one should avoid spectral conflicts.

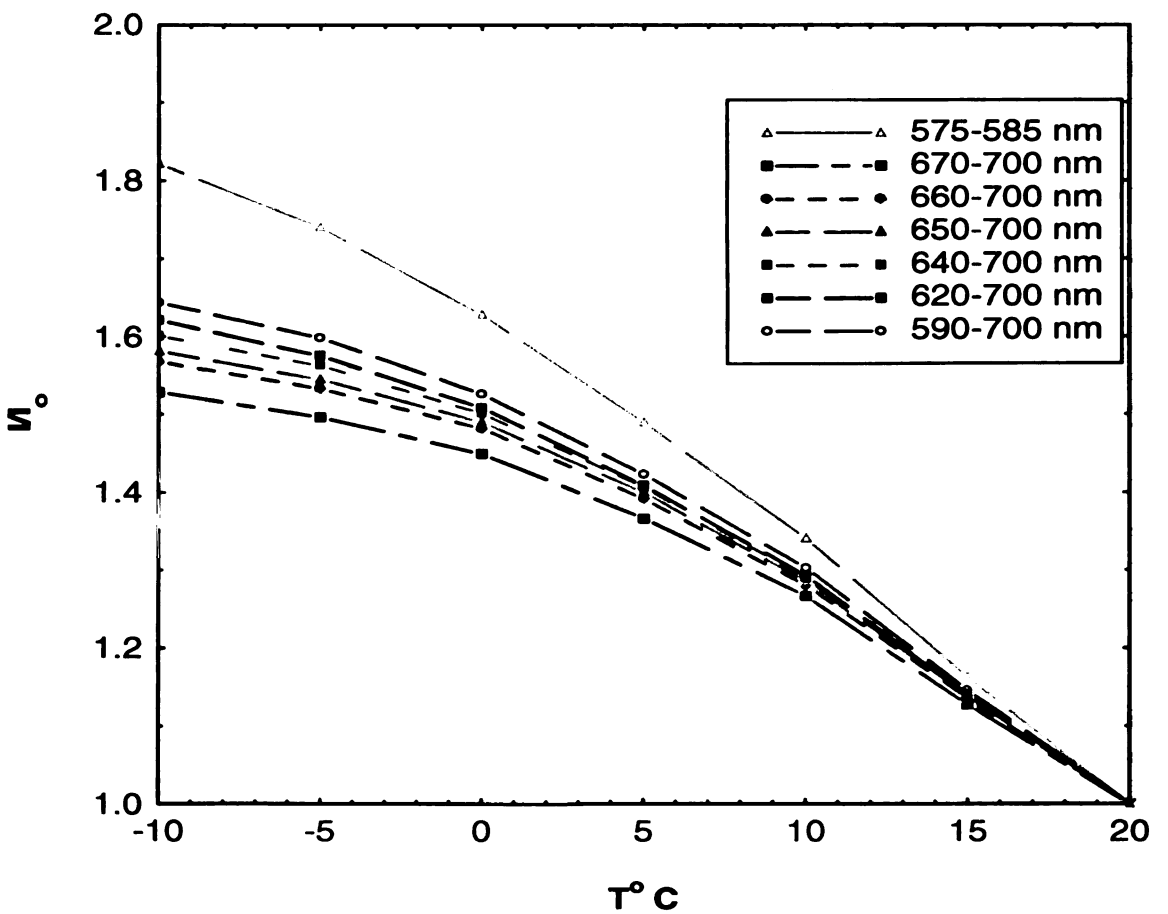

Figure 3-4: Average intensity ratio vs. temperature for different ranges of wavelengths

3.1.2 Spectral conflicts in two-color LIF two-dye approach

There are two main spectral conflicts that one would usually face when choosing two dyes and those are related to the overlap between absorption and emission bands (Coppeta and Rogers 1998). The first is shown in Figure 3-5 (a), where there is an overlap between the emission bands of each dye (conflict type I). As shown, some of the fluorescence from dye 1 will appear in intensity measurement of dye 2 and vice versa. This implies that, unless optimal filtering is used, one could mistakenly measure fluorescence from dye 1 as light from dye 2 and fluorescence from dye 2 as light from dye 1, resulting in inaccurate temperature measurement. One should select two dyes such that the emission spectra have minimum overlap.

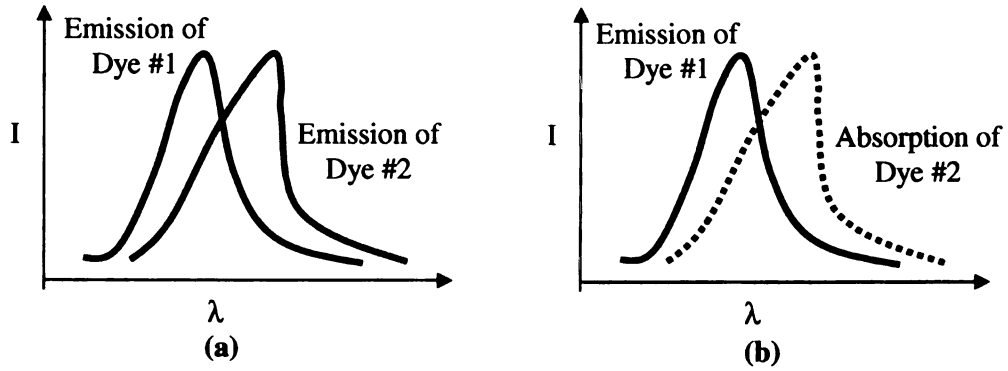

Figure 3-5: Spectral conflicts. (a) Conflict type I, (b) Conflict type II

The second type of spectral conflict occurs when the emission band of the first dye and the absorption band of the second dye (or the emission band of the second dye and the absorption band of the first dye) have an overlap (Figure 3-5 (b)). This means the fluorescence of the first dye gets absorbed by the second dye or vice versa, making the value of the fluorescence ratio become a function of optical path length. One way to

decrease the effect of this conflict is to use low concentration of both dyes. However, low concentrations of dyes will decrease the fluorescence intensity, thereby causing the need for a more powerful laser source or very sensitive cameras.

3.1.3 Selected dyes in two-Color LIF two-dye approach

Many researchers have chosen fluorescent dyes such that one is temperature sensitive and the other is insensitive to temperature variation (Sakakibara and Adrian, 1999; Kim and Kihm 2001). The most common dyes used so far in two-color LIF two-dye approach are Rhodamine B (temperature sensitive) and Rhodamine 110 (temperature insensitive). When these two dyes are mixed in the solution, it has been reported that the maximum sensitivity (rate of change of the ratio intensity with temperature) of 1.6-1.7% K^{-1} can be obtained and the resulting random error is 1.0 K. Since some of the flow features investigated in this study had a temperature difference of less than 2^{o} C across, it was found necessary to improve the sensitivity of the LIF technique to resolve these features. After careful research and investigation, fluorescein and kiton red were chosen as the two fluorescent dyes in the two-color LIF two-dye approach. As will be shown later, the combination of these dyes will improve the sensitivity of this technique to 4% K^{-1}. By choosing appropriate CCD cameras, the random error can be reduced to 0.2^{o} C. In temperature measurement LIF techniques it is very important to find fluorescent dyes that are sensitive to temperature variation but insensitive to pH variation. If the pH of the solution changes during the process and the dye is pH sensitive, then the measured temperature values would be inaccurate. In the next section, the pH dependency of these dyes will be discussed.

3.1.4 pH dependency

Fluorescein is a temperature sensitive dye that has been used by many researchers (Coppeta and Rogers 1998). It is also one of the pH dependent dyes. Figure 3-6 shows the relative absorption and emission spectra versus wavelength for both Fluorescein and Kiton Red. Kiton Red does not exhibit a pH dependent absorption over the range of 3 to 10 pH units. It should be noted that Rhodamine B could have been chosen as one of the temperature sensitive dyes instead of Kiton Red. The reason for using Kiton Red is because its absorption and emission spectra are farther shifted to the right in comparison with Rhodamine B. This reduces spectral conflicts (as described before) when used in combination with Fluorescein.

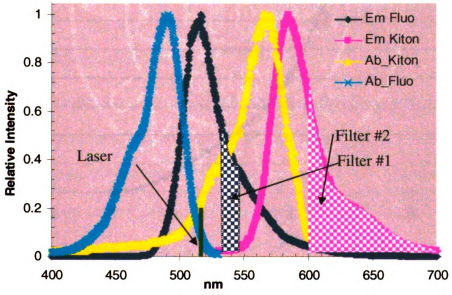

Figure 3-6: Emission (Em) and absorption (Ab) spectra of Fluorescein and Kiton Red (Excitation=514 nm, pH=8)

The absorption band of fluorescein is a function of pH over the range of 3 to 8 pH units.

Figure 3-7 shows the intensity variation of fluorescein with pH. The largest change in intensity versus pH occurs in the range of 6 to 7 pH units. The fluorescence intensity remains constant after a pH of 7.4. As will be discussed later, in order to operate in the pH-independent range of fluorescein, the pH of all ammonium chloride solutions was raised to 7.8 by adding Sodium Hydroxide (NaOH). Based on Coppeta and Rogers's (1998) findings, Kiton red's emission intensity is pH independent over the range of 3 to 10 pH units.

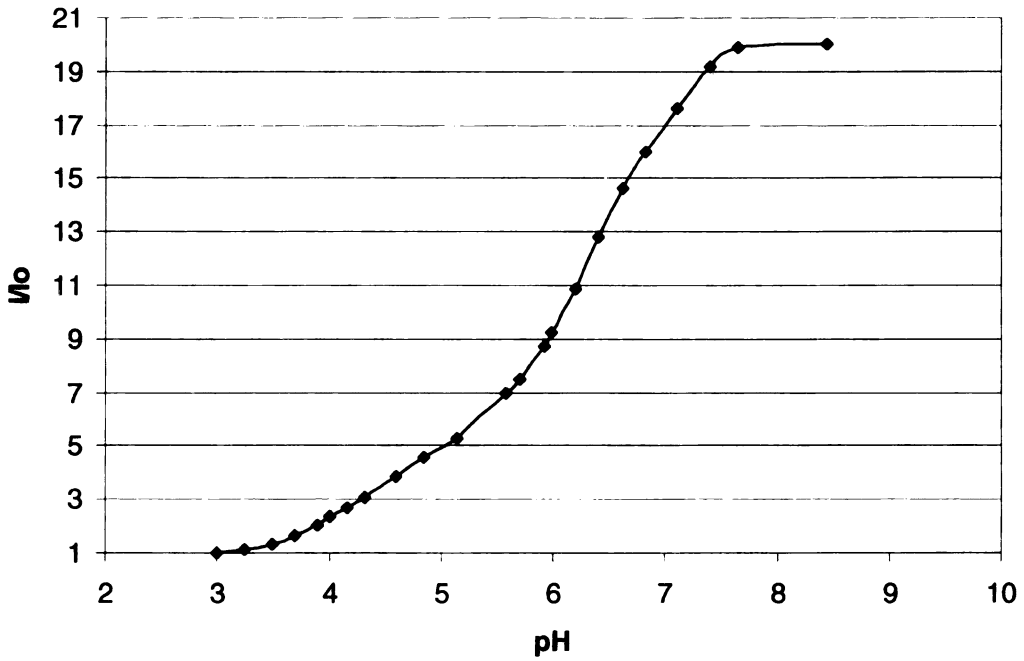

Figure 3-7: Intensity variation of Fluorescein with pH.
(excitation=514 nm, concentration=10^{-6} mol/lit))

3.1.5 Temperature dependency

Both Fluorescein and Kiton red are temperature sensitive dyes. To minimize the spectral conflicts mentioned before, two spectral bands were selected using two optical filters. One spectral band was detected by using a narrow band pass filter (535-545 nm half bandwidth). This filter detects the emitted intensity of Fluorescein in the solution. The reason for choosing such a color band is to avoid detecting the excitation wavelength of the laser, which is at 514. The other filter used is a long pass filter ($\lambda > 600$), which detects the emitted intensity of Kiton red. As can be seen in Figure 3-6, there is a spectral conflict on the emitted color band of the Fluorescein. The emitted light at the chosen color band (535-545 nm) of Fluorescein is partially absorbed by Kiton red. To reduce this conflict (as shown in calibration curves later), the concentrations of Fluorescein and Kiton red were minimized to be 5×10^{-7} mol/lit.

3.1.6 Calibration process

To obtain the relation between the measured fluorescence intensity and the solution temperature, the container used for visualizing the solidification process was also used (see Figure 2-4) in the temperature calibration. The test section was filled with the solution (Ammonium Chloride 19% wt, $5\text{x}10^{-7}$ mol/lit Fluorescein and $5\text{x}10^{-7}$ mol/lit Kiton Red). Nineteen percent by weight NH_4Cl was used to avoid solidification during the calibration process. The temperature could be lowered down to -15°C without solidifying the ammonium chloride (see Figure 2-1). In order to have a uniform temperature, the solution in the container was stirred continuously.

The solution was excited by an argon-ion laser at 514nm and two Pulnix cameras (TM-9701) recorded fluorescence images from fluorescein and kiton red by means of the two described filters in front of their optical lenses. To find the value of the fluorescence intensity, 30 sequential images were averaged to obtain a time averaged intensity image. The value of the fluorescence intensity represents an averaged intensity of a small region of 32 × 32 pixels of this image. Figure 3-8 shows measured intensity variation of both dyes with temperature for different solutions (with and without NH_4Cl) and different optical paths L.

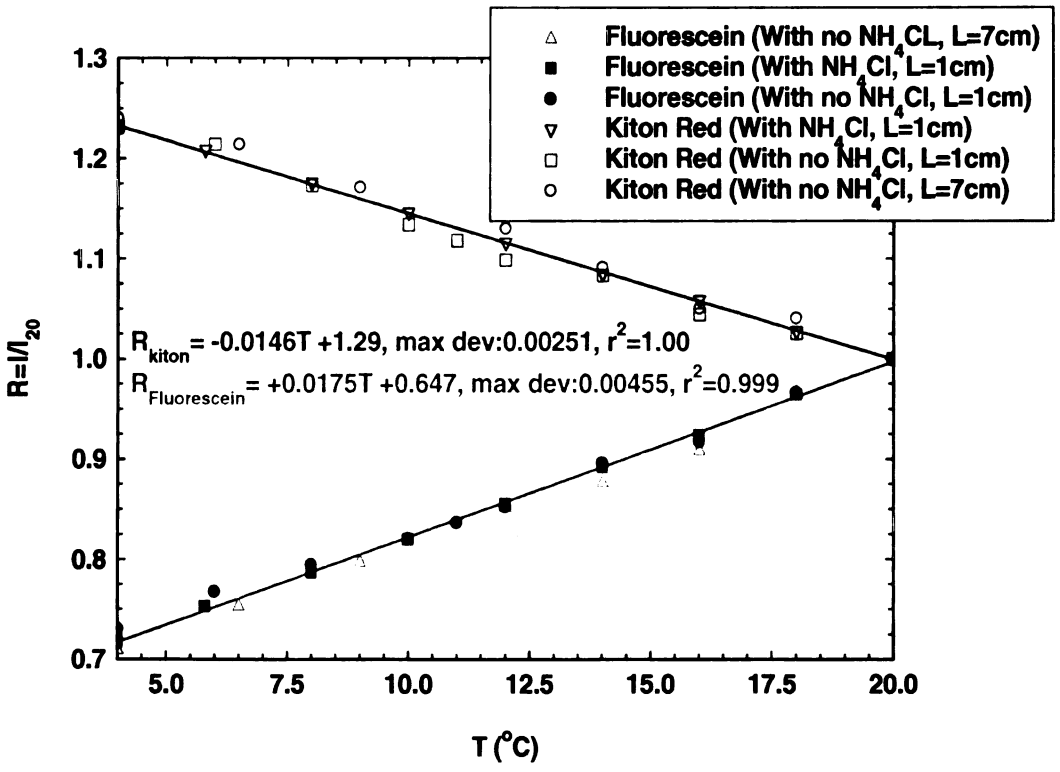

Figure 3-8: Intensity variation of Kiton Red and Fluorescein with Temperature (excitation=514 nm, concentration=5×10^{-6} mol/lit)

The measured intensities of these two dyes are individually normalized by their intensity at 20°C. The temperature was not lowered below 3°C because experimental results obtained by Wirtz (1998) suggested that the temperature of the mush/melt interface was always above 4°C. The intensity of fluorescein decreases with decreasing temperature while that of the kiton red increases.

Figure 3-9 presents the same calibration data in terms of the normalized intensity ratio of kiton red over fluorescein. It can be seen that the optical path length has little effect on the calibration curve and the error resulted from the optical path length at worst case is less than 0.4° C. This error is mainly related to the spectra overlap and re-absorption of the emitted light as passing through the solution before detection by the cameras. However, in order to obtain the best accuracy and minimum error possible, for each experiment an appropriate calibration curve corresponding to its optical path length L was used to find the temperature map of the solution.

The fact that the intensity of one dye increases and the other decreases with decreasing temperature, results in a higher temperature sensitivity (4% K^{-1}) in the two-color LIF two-dye approach compared to all previous implementations of the two dye approach (maximum of 1.7% K^{-1}). This means that a 1°C temperature variation corresponds to about 4% variation in the total fluorescence ratio. This is an important outcome of this study.

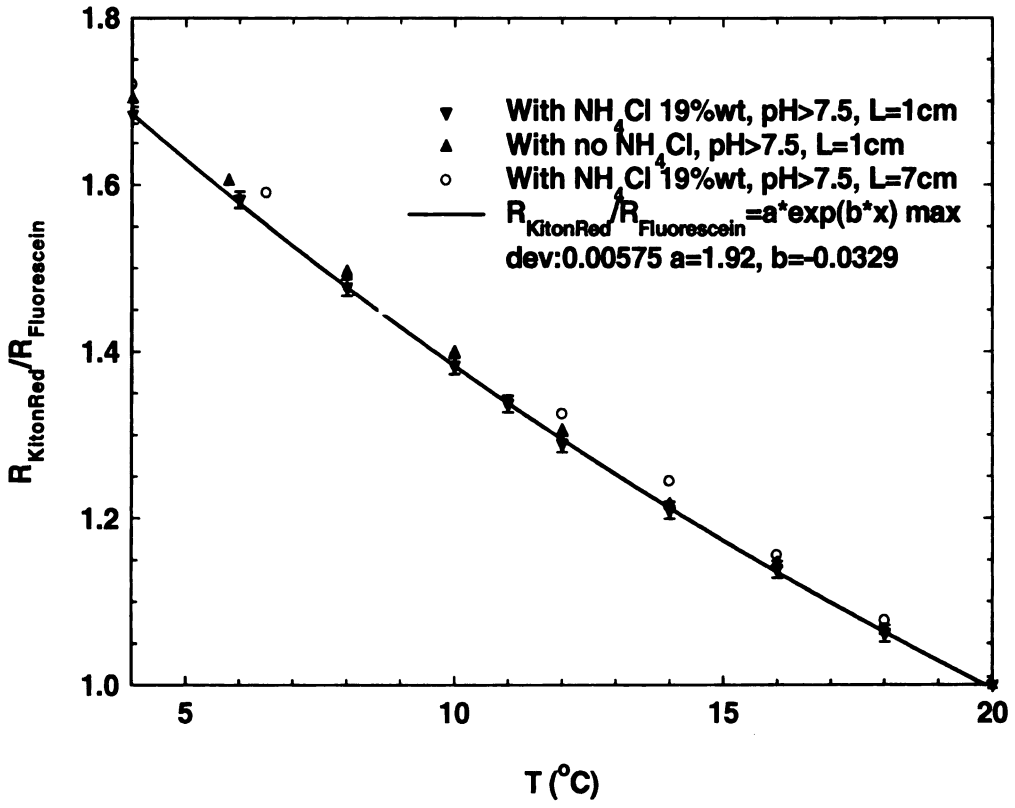

Figure 3-9: Variation of the Intensity ratio of Kiton Red and Fluorescein with temperature.(Excitation: 514 nm (5×10^{-7} mol/lit))

These two dyes were used to measure the temperature distribution in two-dimensional planes during solidification of ammonium chloride solution. In most of our experiments the optical path length of the imaged area was 3 cm; therefore, the calibration curve with the green line (Figure 3-9) was used to minimize the error associated with the optical path length. As already mentioned, two-color LIF was used so that the intensity non-uniformities could be taken into account. A good example of these non-uniformities of this laser is given below.

Since the index of refraction of a finger or a plume is different than that of the surrounding fluid as the plume or finger rises vertically in a helical motion, the curved

edges of it causes the laser sheet to diverge and converge results in dark streak patterns in certain areas of the image (Figure 3-10).

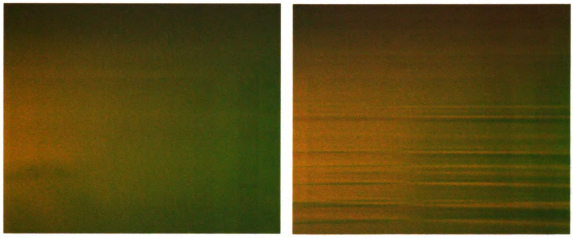

(a) **(b)**

Figure 3-10: Fluorescent intensity of the imaged area. (fluorescein and kiton red mixture) (a) Before solidification, (b) During solidification

The two-color LIF technique can suppress the effect of these streaks on the measured temperature values. Figure 3-11 (a-b) shows the measured temperature values if only fluorescein (one-color LIF) or kiton Red (one-color LIF) were used individually as in a single dye approach. Figure 3-11 (c) shows the temperature measurement results when the two-color LIF was used. It is clear that the two-color LIF reduced many of the artifacts caused by the streaks on temperature maps, resulting in more accurate results. The reason for the remaining streaks is the slight miss-alignment of the two cameras, which was done in the empty container to capture the images of approximately the same area in the flow field. It was realized later that after the solution was poured into the container, due to difference in index of refraction and the optical path, the images captured by two cameras became slightly misaligned. Due to this slight misalignment,

some streaks still remained in the final temperature map. To get the best results, the cameras were aligned while the solution was already in the container for all of the experiments.

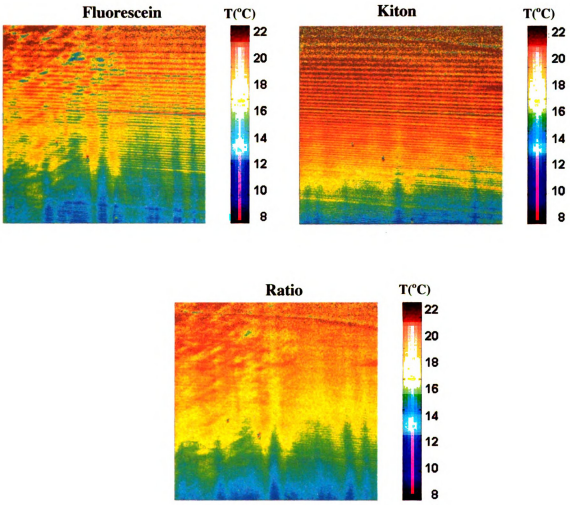

Figure 3-11: The temperature measurement values if only (a) Fluorescein (one-color LIF) or (b) Kiton Red (one-color LIF) is used. (c) The temperature measurement results when the intensity ratio (two-color LIF) is used.

3.1.7 Error analysis

The digital CCD cameras are the most important part of the system and their noise characteristics have a direct impact on the measurement accuracy of the fluorescent emission intensity. There are two major noise sources that one should be aware of: shot noise and dark current noise. The laser intensity variation was less than 0.1%, but was not important since a ratiometric approach was used.

Shot noise

Shot noise constitutes the major part of the total noise and is the noise associated with the random arrival of photons at any detector. Since the time between photon arrival is governed by Poisson statistics, the RMS in number of photons collected during a given period of time is (Eastman Kodak Company 2001):

$$\sigma_{shot} \approx \sqrt{S}$$

where σ_{shot} is the shot noise and S is the signal, both expressed in either electrons or photons. For example, a 10000-electron exposure will have a shot noise of 100 electrons. This implies that the best signal-to-noise ratio possible for a 10,000 electron signal is 10,000/100 = 100. This corresponds to 1.0% uncertainty in measured instantaneous intensity. The only way to reduce this noise is to use a camera with larger full-well capacity. The full-well capacity is the maximum number of electrons generated before the camera is saturated.

Dark current noise

Dark current is the result of imperfections or impurities in the depleted bulk silicon. Electrons can be freed from CCD material through thermal vibration of the CCD and then trapped in the CCD. The most effective way to reduce dark current is to cool the CCD. Using small exposure times also reduces this noise. Although the average dark signal can be subtracted out, the shot noise associated with this signal cannot. As in the case of photon shot noise, the amount of dark current shot noise is equal to the square root of the dark signal

$$\sigma_{shot} \approx \sqrt{D}$$

The image resulting from subtraction of a raw image and a dark frame is more than this by a factor of $\sqrt{2}$ since both images have the dark noise embedded in them. The dark signal, D (electrons/pixel/s), is a characteristic of the camera which is given by the manufacturer.

A simple test was performed to evaluate the total noise of the 8-bit Pulnix cameras (TM-9701). These cameras were originally used for some of the experiments before new 12-bit PixelFly cameras were purchased. An LED (light emitting diode) was placed in front of a Pulnix camera's lens and 150 images were taken. Figure 3-12 shows the time variation of the recorded intensity normalized by average intensity, $I_{average}$ (100 counts in this case). The LED was energized by a DC power supply (Power Designs TP 340A) with voltage stability better than 0.02%. The stability of the luminous intensity of

the LED was measured by a photodiode and the RMS of the output voltage of the photodiode was 0.1%.

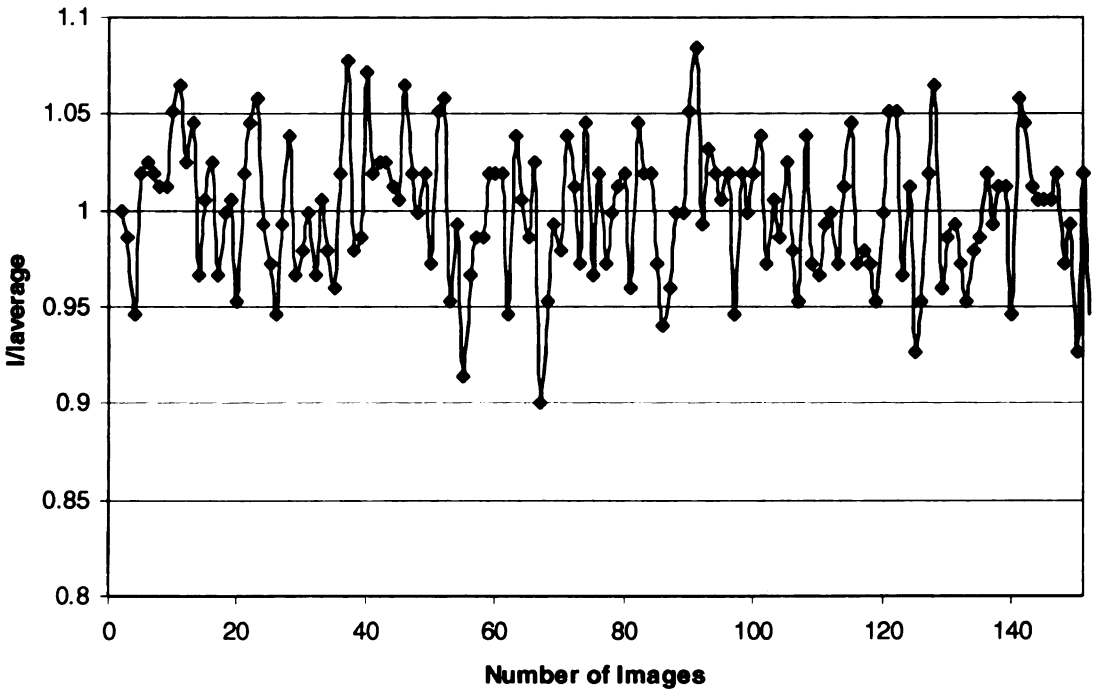

Figure 3-12: Intensity variation of a pixel vs. number of images

Since the uncertainty of the output voltage of the photodiode itself was 0.1%, it was concluded that stability of the LED luminous intensity was at least better than 0.1%. The intensity of a selected pixel was measured and plotted against the number of images. From Figure 3-12 the standard deviation was found to be 3.5 counts, or 3.5% of the average intensity value. This standard deviation results in 0.8°C uncertainty in temperature measurement in the two-color LIF technique (using fluorescein and kiton red as fluorescent dyes). This uncertainty can be reduced by using CCD cameras with lower shot noise (higher full well capacity), such as the Pixelfly cameras (The Cooke Corporation), which have half of the shot noise of the Pulnix cameras (Appendix E).

Averaging the images also reduces the total uncertainty by a factor of the inverse square root of the total number of averaged images. Pulnix cameras were used initially for some of the experiments and an averaging technique was used to reduce the total uncertainty of the temperature values. However, in order to obtain better signal to noise ratio, two new cameras (Pixelfly cameras) were purchased later on and used for the rest of the experiments. These cameras have a full-well capacity of 20,000 electrons. If half of this capacity is used, the related shot noise would cause 1% uncertainty in measured intensity. The combination of shot and dark noises for these cameras will result in a $0.4^{O}C$ uncertainty in temperature measurement in two-color LIF technique (using fluorescein and kiton red as fluorescent dyes). The uncertainty resulted from these cameras is half of that of Pulnix cameras. Another advantage of using these cameras is their resolution. These cameras (1022x1394 pixels) have four times more pixels than those of Pulnix cameras (480x640 pixels). Therefore, by spatial averaging (averaging of four pixels) one can reduce the uncertainty of this technique to $0.2^{o}C$ per equivalent pixel of a Pulnix Camera. Therefore, at pixel level, PixelFly cameras perform much better than Pulnix cameras.

Velocity Measurement Techniques

In this study, in order to understand some of the observed flow features during the solidification processes of the ammonium chloride solution, such as the flow field above a portion of the mushy zone where no plume existed and also the flow field between two

adjacent plumes (will be discussed later), two different optical diagnostic techniques were used to obtain the velocity fields in these regions.

3.2 Particle Image Velocimetry (PIV)

PIV measures whole velocity fields by taking two images shortly after each other and calculating the distance that the individual particles traveled within this time. From the known time difference and the measured displacement the velocity is calculated. The most common way of measuring displacement, is to divide the image plane into small interrogation spots and cross-correlate the images from the two time exposures. The spatial displacement that produces the maximum cross-correlation statistically approximates the average displacement of the particles in the interrogation cell. The PIV images were processed using an in-house correlation code written in C (MTV code). In order to reveal the flow motion, generally the flow is seeded with particles which will scatter the light sheet and are imaged two or more times from the side by a CCD camera. However, in this study, neutrally buoyant particles (i.e. impurities) that already existed in the ammonium chloride solution were used for velocity measurements and no additional particles were seeded in the flow. The size of the impurities or particles in the solution was less that 20 μm. The resulting double or multi-exposed image, taken in a known time interval, provided a displacement record of the particles within the measurement plane, which is then analyzed and scaled to velocity. The velocity information produced in this way tends towards the instantaneous velocity distribution, as camera exposure time is smaller than the delayed time between two images.

As will be discussed later, due to the lack of seeding particles in the plumes during the solidification process of ammonium chloride solution, PIV technique could not

be used to obtain velocity information in the plumes. Therefore, Molecular Tagging Velocimetry (MTV) technique was chosen as an alternative technique to obtain the velocity profile of the plumes.

3.3 Molecular Tagging Velocimetry (MTV)

Molecular Tagging Velocimetry (MTV) is a whole-field optical technique which uses molecules that can be turned into long lifetime tracers upon excitation by photons of an appropriate wavelength. Typically a pulsed laser is used to tag the regions of interest and those tagged regions are interrogated at two successive times within the lifetime of the tracer by taking two successive images. The displacement of the tagged region between the two interrogation times is determined and the measured Lagrangian displacement vector provides the estimate of the velocity vector. A description of this measurement technique is given by Gendrich and Koochesfahani (1996) and Koochesfahani (1999).

There are several chemicals which can be applied as tracer molecules for MTV. Caged fluorescent compounds are fluorescent molecules covalently modified by the addition of a chemical group that renders them nonfluorescent. This modification has the additional property that it can be removed by exposing the molecule to ultraviolet light, which cleaves the bond between the modifying group and the fluorescent molecule, restoring the original molecule and its fluorescence. Caged fluorescein is one of these chemicals. After cleaving the bond, fluorescein molecules can be tagged by an additional laser (Argon Ion 488 nm). Thus, for uncaged fluorescent dyes, two sources of photons are needed, one to break the cage (UV laser) and the other to excite the uncaged fluorescent

dye (Argone Ion laser). The use of caged fluorescein and similar compounds was first introduced by Lempert *e. al.* (1995). The advantage of using this chemical is that the fluorescence of the uncaged dye persists (practically infinite) for a very long time and can be interrogated for very low flow velocity. One of the disadvantages of using this chemical is that the cage-breaking process is irreversible. The other disadvantage of using this chemical is that it requires two laser sources and makes it more expensive to use.

The bleaching method is another way to measure velocity vectors in the flow. The bleaching method uses a high energy UV laser to bleach tracer molecules in a certain region of interest. The principle of determining the velocity is the same as the caged fluorescent dyes. A fluorescent dye such as fluorescein will be excited by a laser (Argon Ione) and then get bleached by high energy UV laser. The bleached area (dark area) will be interrogated within an illuminated (bright) area. The bleaching technique has the same advantages and disadvantages as the caged fluorescent dyes.

In this work, MTV based on phosphorescent tracers was utilized. The phosphorescent compound (MTV Triplex) used for the purpose of this research consists of a lumophore, 1-Br-Np; an alcohol, cyclohexanol; and a sugar, cyclodextrin; and is collectively known as 1-BrNp.Mβ-CD.ROH. The concentrations of the MTV triplex used in this study are $2 \times 10^{-4} M$ for Maltosyl-Cyclodextrin, $0.06M$ for alcohol and a saturated amount of bromo-napthalene was added (Gendrich *et al.* 1997). This tracer was added into the ammonium chloride solution. Due to the small concentrations of the tracer, the solidification process was not affected by the presence of the tracer. When excited with an excimer laser (308nm), these tracers emit light that has a lifetime of ~5ms. In this

case, only one source of photons (laser) is needed, and the excitation/emission process is reversible.

Line or grid patterns created with the laser can be imaged at two successive times and are correlated to obtain the velocity profiles, or the velocity vectors of the plumes (Lum, 2001). Line tagging written into the flow field provides a measurement of the velocity component perpendicular to the line and it provides one dimensional velocity values. An example of line tagging is shown in Figure 3-13. As will be shown later, this method was used to obtain velocity profiles of some plumes.

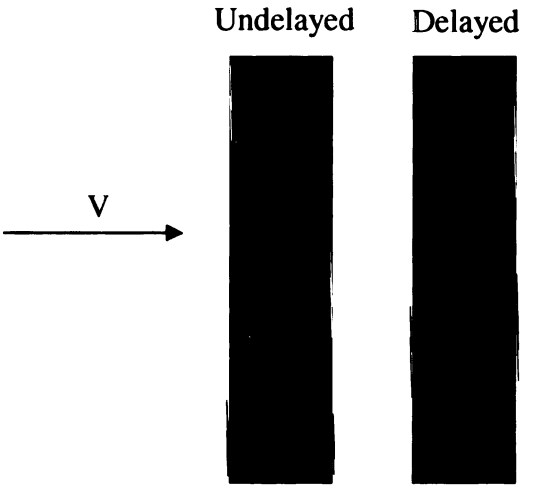

Figure 3-13: Example of undelayed and delayed lines for line tagging MTV (Δt = 35 ms)

The typical concentration of the ammonium chloride solution is 26% by weight, whereas the highest concentration of the three components of the MTV triplex is less by at least three orders of magnitude (in molar concentration). To confirm this, experiments with and without using the tracer were performed by Lum *et al.* 2001. A comparison between the experiments did not indicate any change in behavior including the variation of mushy

zone height with time. Thus, the solidification behavior is not noticeably influenced by the presence of the tracer molecules.

Chapter 4

Optical setups

In this chapter, the three different experimental setups for LIF, PIV and MTV techniques will be described.

4.1 Optical setup for LIF

The experimental setup for the LIF technique is shown schematically in Figure 4-1.

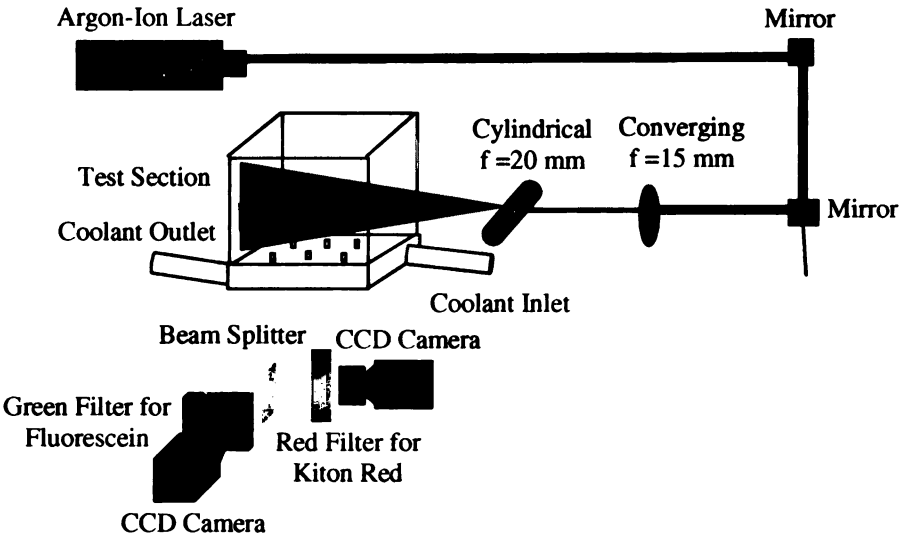

Figure 4-1: Schematic of the optical setup for LIF technique

The main objects in this setup are an argon-ion laser, mirrors to direct the laser beam, a converging lens, a cylindrical lens to create a laser sheet with a thickness of 0.3 mm, a beam splitter, two CCD cameras (Pulnix TM9701, 30 frames/s or PixelFly, 12

frames/s), and two optical filters (Edmund Industrial Optics). The excitation wavelength of the argon-ion laser is set to 514 nm with a power of 1.5 Watts. The test section is the same as the one described in Figure 2-4. The width of the sheet is 0.3mm. The CCD cameras are mounted on translational stages and adjusted to capture images of approximately the same area in the flow field (within one pixel). This can be done by subtracting the two images from two cameras simultaneously and aligning the cameras until the resulting image has minimum intensity values (subtracting two identical images results in an image with pixel values of zero count). To obtain sub-pixel accuracy after aligning the cameras, a calibration plate, which has an equally spaced grid pattern at 1-mm intervals on its surface, is placed in the plane of the laser sheet (the plane in which temperature is measured) and illuminated by a halogen lamp. One image captured from one camera is assumed to be the base image and the other image captured by the other camera is assumed to be the deformed image. The displacement between grid points on the base image and the deformed image gives a mapping equation. This mapping equation maps the location of all pixel points of the deformed image on to the base image. The displacement between grid points of base image and deformed image is found using an in-house correlation code written in C (MTV code). This correlation code was developed at the TMUAL (Turbulent Mixing and Unsteady Aerodynamics Laboratory, Gendrich *et al.* 1997) at Michigan State University and can produce a sub-pixel accuracy of 0.1 pixels. After obtaining the displacements between each grid point in the base image and that in the deformed image, a 3^{rd}-order polynomial function was fitted by the least-squares method (MATLAB Code) to find the mapping equation. Since the intensity ratio obtained from two cameras is needed to obtain the temperature map, a bi-linear

interpolation scheme was used to obtain intensities at sub-pixel locations. This alignment procedure is the same for both Pulnix cameras and PixelFly cameras. The framing rate of the 8-bit Pulnix cameras is 30 frames/second and that of the 12-bit PixelFly cameras is 12 frames/second. Pulnix cameras have a special resolution of 480×640 pixels and PixelFly cameras have a special resolution of 1024×1392 pixels. It should be noted that the laser sheet should not intersect with the mushy zone during the solidification process, because the resulting reflection from the mushy zone contaminates the true LIF signals. The procedure of synchronizing the Pulnix and PixelFly cameras is detailed in Appendix B.

Some bleaching effects were observed at early stages of the solidification process (0 to 8 min) where convection was slow above the fingers. The intensity of fluorescein would drop 1% at some locations on the imaged plane when it was exposed to the laser sheet for more than 2 seconds. To eliminate this effect, a shutter was used to minimize the amount of time that fluorescein was exposed to the laser sheet (less than 0.5 second).

4.2 Optical setup for PIV

The experimental setup is similar to that of the LIF technique except that only one camera is used to capture scattered light from the particles (Figure 4-2). It should be noted that there is no need for an optical filter in this setup since the particles scatter light with the same wavelength as that of the laser sheet. The same in-house correlation code used to find displacement between grid points of the base image and the deformed image in the aligning procedure is used to find the average velocity of the interrogating cell in the PIV technique. As mentioned before, this results in a sub-pixel accuracy of 0.1 pixels.

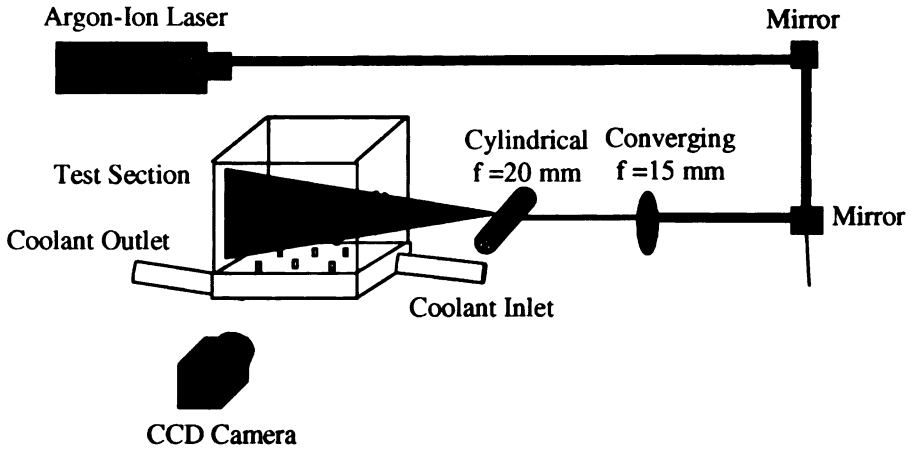

Figure 4-2: Schematic of the optical setup for PIV technique

4.3 Optical setup for MTV

In this work, a line tagging technique was used to obtain velocity profiles of some plumes. Creating the appropriate line tagging pattern for velocity measurements involves a setup of optics. To make fine laser lines, two lenses were used to manipulate the laser beam and to make a laser sheet that is as thin as possible. As shown in Figure 4-3, a VFL (Variable Focal Length) setup consisting of a 150mm and 50mm cylindrical lens were used to increase the aspect ratio of a 20ns, 100mJ/pulse beam from an excimer laser (Lambda Physik LPX 220 iCC filled with XeCl). The thickness of the laser sheet passing through this optical setup would be about 0.5mm. To obtain multiple laser lines, the laser sheet is passed through a beam blocker to create the line patterns. The beam blocker is basically a plate with an array of slots that are very thin. This optics setup was used to measure the flow field near the mushy zone where the velocities are slow - on the order of 0.5mm/s. In order for the smaller features within the flow field to be resolved, the beam blocker with the slot spacing of 0.8mm and slot width of 0.15mm was used.

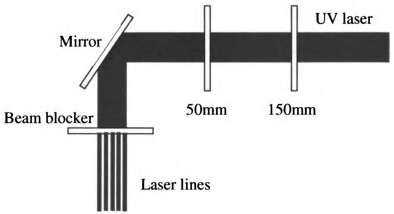

Figure 4-3: Optical setup for MTV technique

In imaging the fields of view, an intensified camera and various electronics were used in order to detect the tagging pattern in low light conditions. A 105mm Micro Nikkor (*f* / 2.8) lens with an additional close-up lens was used in conjunction with an intensified camera (DiCam-Pro). This is a 12-bit, high-resolution (1280×1024 pixels), gated, intensified camera with a fast-decay phosphor (P46). The detector was operated in the dual-frame mode, where two full-frame images of luminescence are acquired in quick succession from the same laser pulse (the delayed time can be specified manually in the software). A four Channel Digital Delay/Pulse Generator (SRS) was used to generate 5Hz TTL pulses to synchronize the camera and laser. For this work, the first frame integrates the fluorescence signal of MTV Triplex for a period of 0.2ms starting at a 0.2 ms delay after the laser pulse, whereas the second frame integrates the phosphorescence signal for a period of 5 ms starting at 35 ms delay after the laser pulse.

As will be discussed later, the MTV technique was used to measure the velocity profile of two adjacent plumes simultaneously. In order to be able to adjust the container such that the laser lines passed through the center of the plumes, the container was placed on rotational and translational stages. During the experiments, the stages were moved and

rotated such that the maximum displacement of the line tagged region in the delayed images was obtained at the location of the plumes and this was done visually. Maximum displacements indicated that the laser lines were passing through the center of both plumes. Schematic of the test section is shown in Figure 4-4.

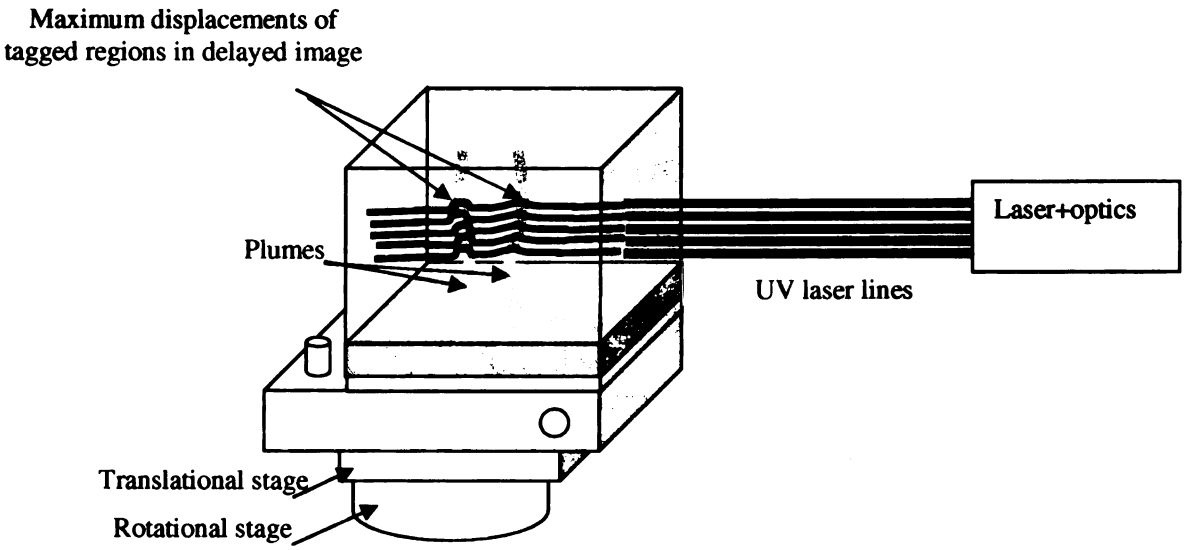

Figure 4-4: Schematic of the test section for MTV technique

Chapter 5

Temperature maps of the plumes

After aligning the two Pulnix cameras, the ammonium chloride solution was poured in the container (26% wt NH_4Cl, $5x10^{-7}$ mol/lit Fluorescein, $5x10^{-7}$ mol/lit Kiton Red) and cooled from the bottom. The thickness of the mushy zone as a function of time is plotted against that obtained by Lum *et al* (2001) to show the consistency between all experiments (Figure 5-1). Due to the small concentrations of fluorescent dyes, the physical properties do not change significantly. Therefore, the thermal and flow behavior of the solution with fluorescent dyes is the same as the one without fluorescent dyes.

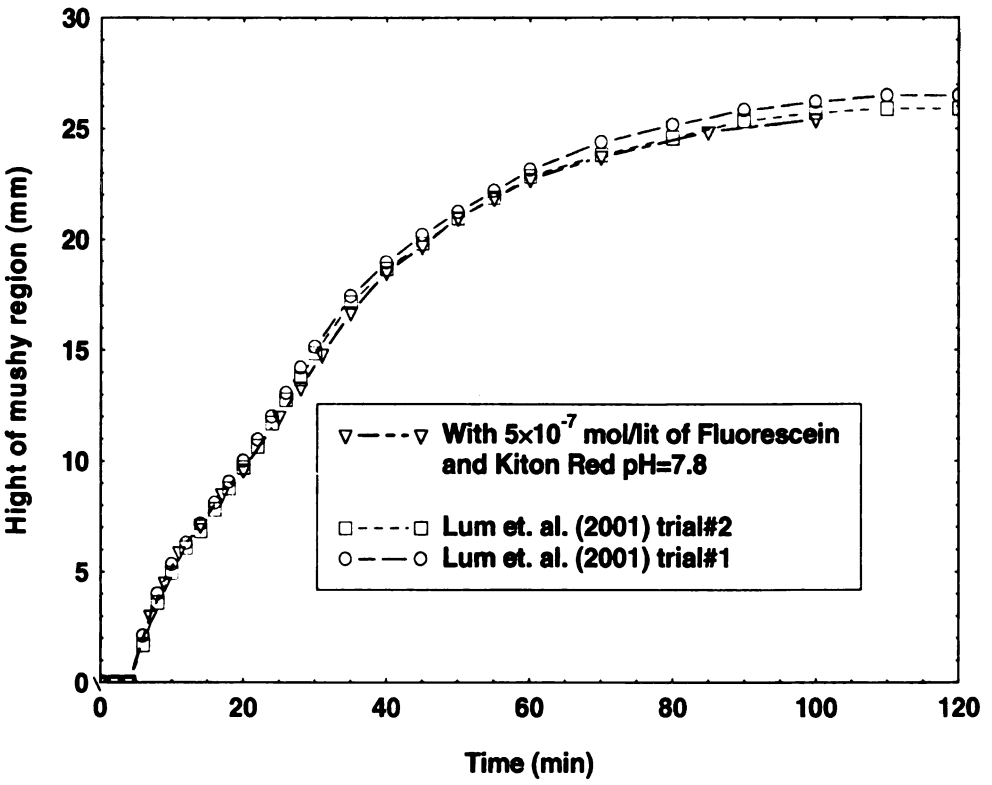

Figure 5-1: Height of mushy region vs. time

As mentioned before, one of the interesting flow features of the solidification processes of ammonium chloride solution is the formation of the fingers and the plumes. In order to characterize the detailed temperature field of these features, the LIF technique was used to obtain the temperature map of a plume in the test section. The imaged area is 2.5×1.9 cm^2 and located above the second nucleator on the first row (Figure 5-2). The imaged area was selected above a nucleator because, based on Wirtz (1998) observation, a plume would form above it. The bottom left corner of the imaged area is at (18mm, 11.71mm, 22.5mm). The origin as shown in Figure 5-3 is located at the front bottom left corner of the test section. The spatial resolution of the measurement in the plane of illumination is, therefore, 40 μm per pixel. The exposure time used in this case was 15 ms.

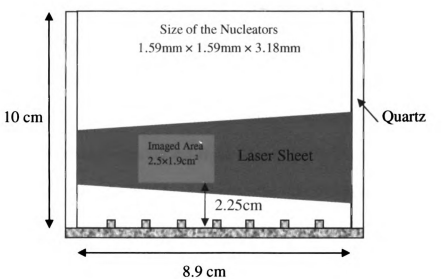

Figure 5-2: The location and size of the imaged area

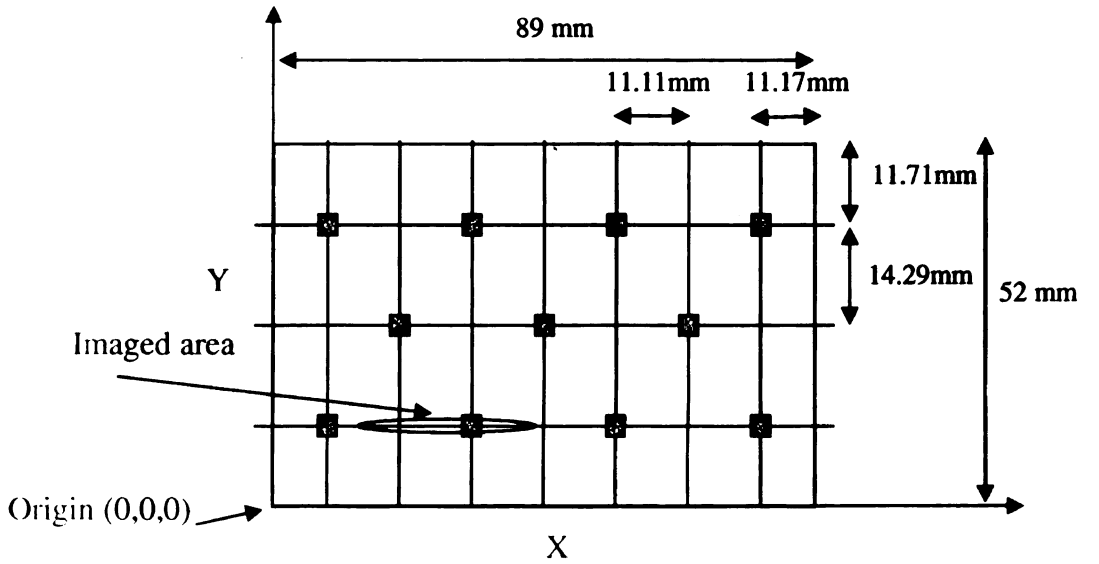

Figure 5-3: The location of the origin and the imaged area

Temperature maps corresponding to this imaged area during the solidification process at different times are shown in Figure 5-4 (a-l). The temperature maps are presented in three different ways. The ones in the left column (Figure 5-4 a,d,g and i) show the instantaneous temperature maps of the plume. The ones in the middle column (Figure 5-4 b,e,h and k) were obtained from averaging ten successive intensity images in time (300 ms). The last columns on the right (Figure 5-4 c,f,i and l) are a result of filtering in space and were obtained from filtering the time averaged temperature maps (middle temperature maps) using Wiener method (8×8 pixels). The color bars display temperature values between 4°C to 24°C.

At t=17 min there are four fingers in the imaged area and one of them seems to have lower temperature than the rest of the fingers (the third finger from the left above ,1.5cm). This finger is right above the described nucleator and will become a plume after t = 20 min. Plume has a signature characterized by its temperature. Its temperature is

cooler than the surrounding fluid. The reason for not seeing as many fingers in the temperature maps as in the shadow graph technique is because, in the shadow graph technique the field of view is integrated across the depth of the test section; whereas, in the LIF technique the resultant temperature maps are obtained from a single plane (the thickness of the laser sheet is small).

At t=30 min while the plume strengthens, adjacent fingers weaken and continue to decline in number. The temperature of the plume is also cooler since the mushy zone has grown (1.5cm in height) and it is getting close to the bottom of the imaged area (0.75 cm below the imaged area).

At t=40 min three of the four fingers subside and only one finger survives as a plume. The mushy zone height is about 1.8 cm and is reaching towards the bottom of the imaged area (0.45 cm below the imaged area). The missing portion of the plume on the top portion of this temperature map is due to the helical motion (Appendix C) of the plume, causing the center of plume to move out of the illuminated sheet.

At t=60 min, one distinct plume can be observed. At this time the mushy zone is right below the imaged area and there is a layer of cooled liquid (thickness of 0.3mm) right above the mushy zone around the plume exit. The feature on the right side of the plume is speculated to be a finger that is about to form. At this time the temperature of the plume at the exit of the mush is about 7.8^{o} C and the mush interface has a temperature of 8.4^{o} C.

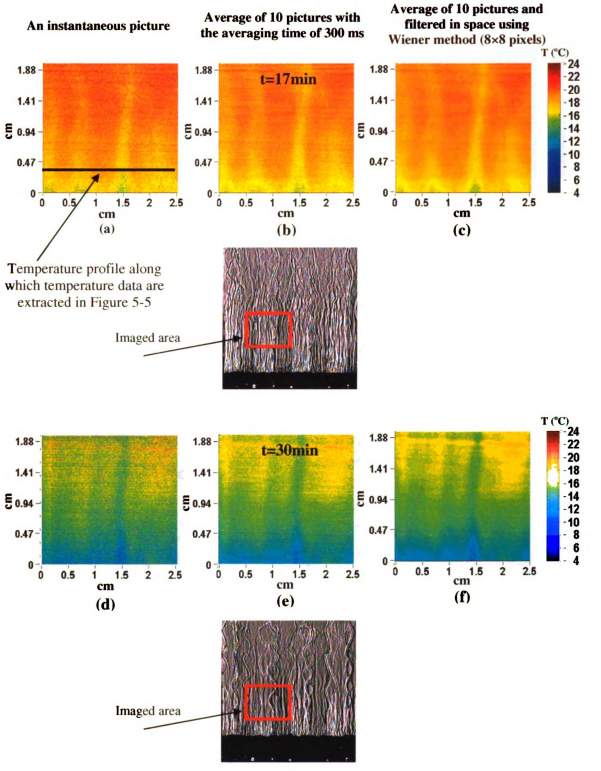

Figure 5-4: Temperature maps corresponding to the imaged area during solidification process

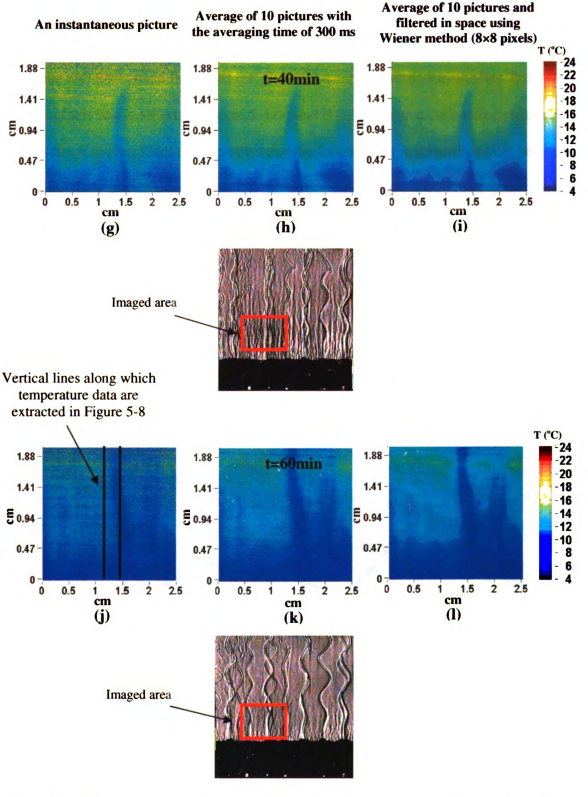

Figure 5-4: Temperature maps corresponding to the imaged area during solidification process

The temperature profiles along a horizontal line on the laser sheet at different times are extracted in Figure 5-5 in order to measure the temperature difference across the plume and understand how cold the plume is compared to its surrounding fluid. The location of this line is shown in Figure 5-4 (a) and is 2.6 cm above the cooling plate along H = 0.3 cm. It is clear from these profiles that the location of the finger that later becomes the plume does not change during the solidification process (minimum peak always remains at X = 1.5 cm). It seems that at t = 25 min the second finger from the right had moved out of the plane of illumination because the temperature profile is flat; however, it reappears later on the image plane.

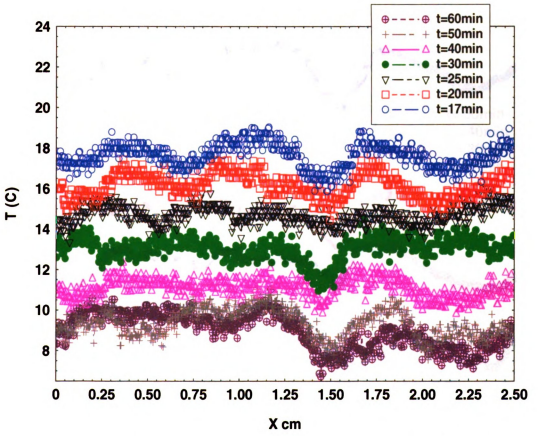

Figure 5-5: Temperature profiles along the horizontal line shown in Figure 5-4(a) (average of 10 consecutive pictures with the averaging time of 300 ms, y = 2.6cm from bottom of plate)

Figure 5-6 shows the same temperature profiles but for spatially averaged images of the time averaged temperature maps. This figure shows smoother temperature profiles due to the spatial averaging. As mentioned before, averaging reduces the error by a factor of the inverse square root of the number of averaged images or number of averaged pixels. Space averaging uses a pixelwise adaptive Wiener method based on statistics estimated from a local neighborhood of each pixel. Matlab's built in routine was used for implementing the Wiener filter. The performance of the filter depends upon the size of the N×M local neighborhood. Larger block size results in a more smoothed image;

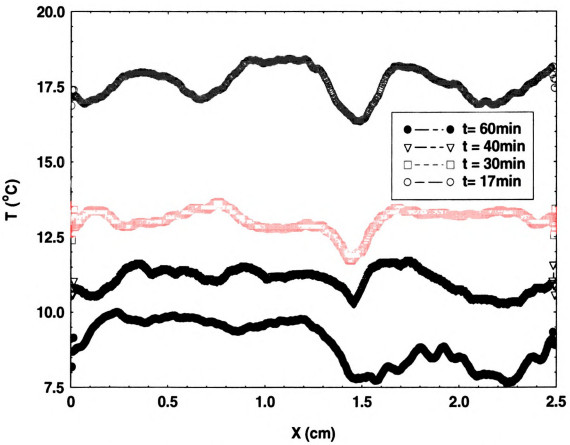

Figure 5-6: Temperature profile along the horizontal line shown in Figure 5-4(a) (y = 2.6cm from bottom of plate, average of 10 consecutive pictures with the averaging time of 300 ms and averaged in space, 8×8 pixels)

smaller block size results in a relatively sharp image. The local mean and the variance around each pixel is estimated using

$$\mu = \frac{1}{NM} \sum_{n1,n2} I_{old}(n_1, n_2) \tag{5-1}$$

$$\sigma^2 = \frac{1}{NM} \sum_{n1,n2} I^2_{old}(n_1, n_2) - \mu^2 \tag{5-2}$$

$$I_{new}(n_1, n_2) = \mu + \frac{\sigma^2 - v^2}{\sigma^2}\left(I_{old}(n_1, n_2) - \mu\right) \tag{5-3}$$

where v^2 is noise variance. n_1 and n_2 represent the row and column numbers. N and M represent the total number of pixels in each row and each column. $I_{old}(n_1,n_2)$ is the intensity value of a given pixel in the image and $I_{new}(n_1,n_2)$ is the new intensity value of this pixel after filtering. Usually, if the noise variance is not given, the average of all the local estimated variances calculated from equation (5-2) is taken as default value.

Figure 5-7 shows the temperature distributions along a vertical line on the plume and along a vertical line adjacent to the plume at t = 60 min and t = 17 min extracted from Figure 5-4 (l) (see Figure 5-4 (j) for the location of these lines). At t = 60 min, the mushy zone is right below the imaged area and the temperature of the plume is very close to the temperature of the adjacent flow at the location where the plume exits from the mushy zone. At this time there is a cold layer of fluid above the mushy layer (see Figure 5-4 (j)) and a steep temperature gradient can be observed in this layer (Figure 5-7 from H = 0 to H = 0.6cm on the black curve, H is measured from Mush-melt interface).

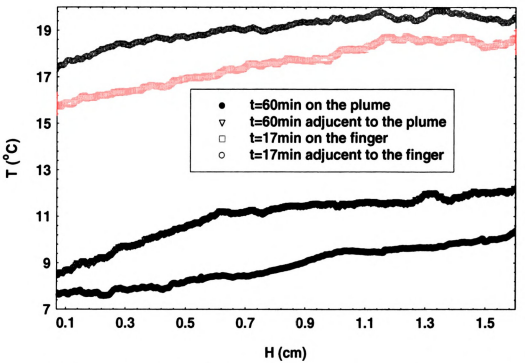

Figure 5-7: Temperature Profiles along the vertical lines shown in Figure 5-4(j) (The location of the origin (H=0) is at the bottom of the temperature map)

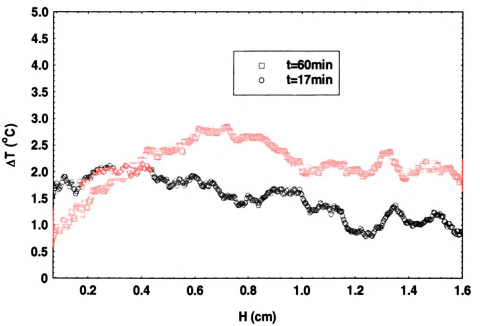

Figure 5-8: Temperature difference ΔT between vertical lines shown in Figure 5-4 (j) (The location of the origin (H=0) is at the bottom of the temperature map)

Figure 5-8 shows temperature difference ΔT between these two lines at t = 17 min and t = 60 min. The maximum temperature difference is about 2.7 °C and occurs when the plume is formed. The temperature difference right at the exit of the mushy zone (H=0mm and t=60min) is about 0.8 °C.

To understand the temperature variation with time above the mushy zone, the whole field temperature maps at different times have been obtained by Pulnix cameras over a much larger area above the first row of nucleators (Figure 5-9). The imaged area is 8×6 cm^2, and the bottom left corner of the image has a coordinate of (0.4mm, 11.71mm, 3mm) with respect to the origin. The spatial resolution of the instantaneous measurement (with no filtering in space) in the plane of illumination is, therefore, 125 μm per pixel. The results are shown in Figure 5-10.

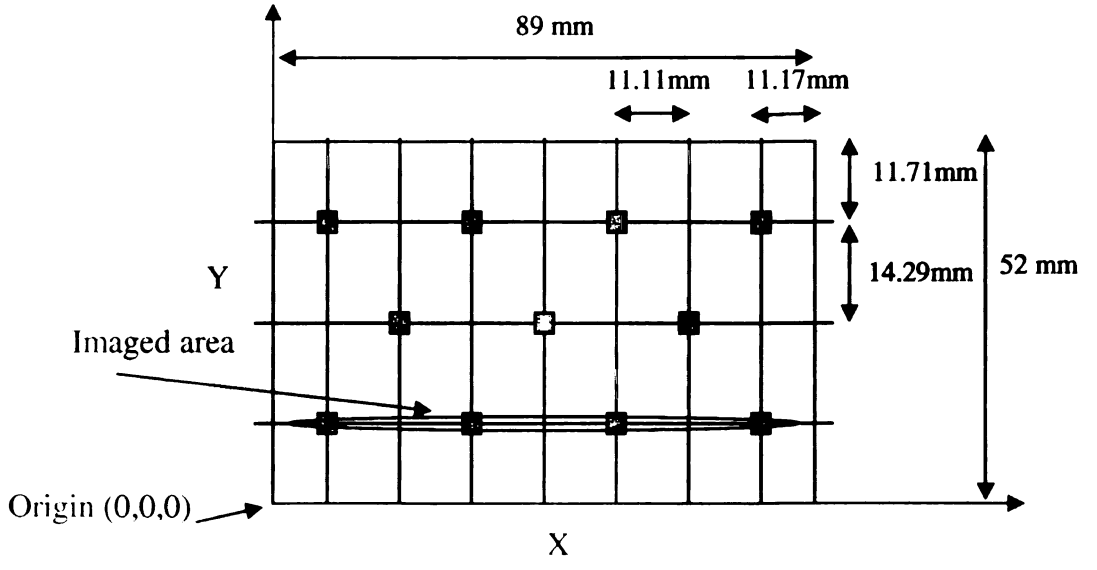

Figure 5-9: The location of the origin and the imaged area

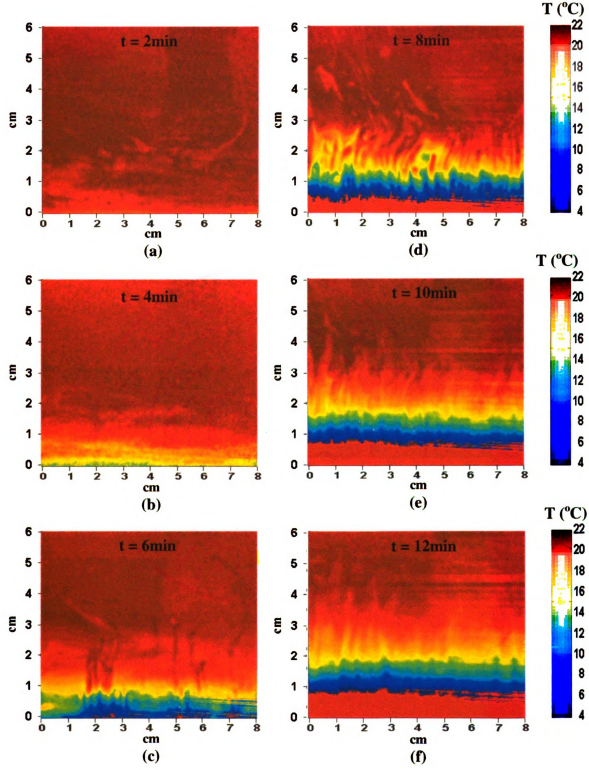

Figure 5-10: Whole field temperature measurement (average of 4 successive intensity images and averaged in space, average of 8×8 pixels)

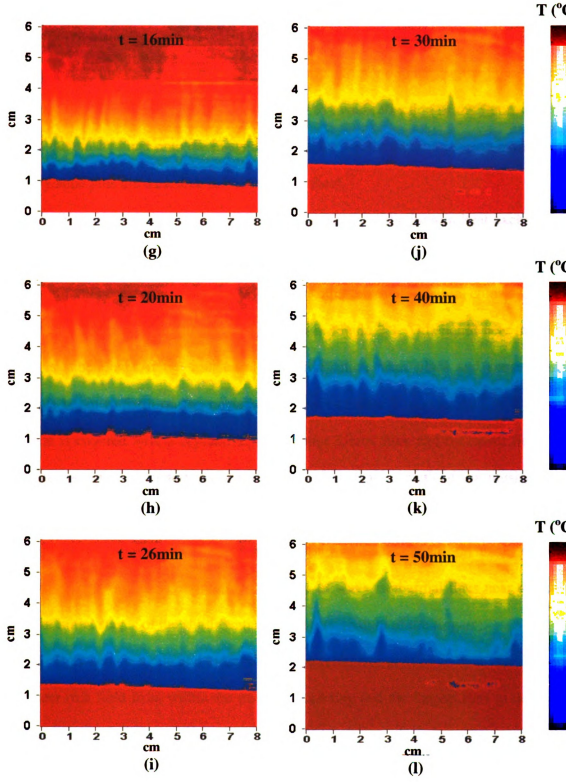

Figure 5-10: Whole field temperature measurement (average of 4 successive intensity images and averaged in space, average of 8×8 pixels)

It should be noted that the red solid region on the bottom portion of the temperature maps does not represent the thickness of the mushy layer. The mushy layer is about 4 or 5 mm below the interface of the red solid region because the laser sheet was always kept 4 or 5 mm above the mushy layer to avoid reflection of the fluorescent light off of the mushy layer onto the imaged area. Therefore, the red solid region represents the mushy zone plus the dark area below the laser sheet.

Within the first 4 minutes of applying coolant to the bottom heat exchanger, no crystals form. However, as seen in Figure 5-10 (b), the temperature of the fluid close to the bottom plate corresponding to 26% wt concentration of ammonium chloride, which is 18.6^{o} C, is well below the liquidus line shown in Figure 2-1. This liquid near the bottom plate is subcooled. At t=6 min onset of solidification takes place and some dendritic crystals begin to form on the nucleators. Within another 2 minutes (at t = 8 min), the surface is covered with a crystalline mush about 5 mm thick and the small fingers and their temperature characteristics are vigorous. The rapid growth of the mushy layer is because of the existence of substantial fluid undercooling. This is qualitatively in good agreement with the results obtained by Neilson and Incropera (1993) using numerical analysis. Their results were presented in terms of wavy isothermal lines near the mushy zone at initial stages of the solidification process (signature of the fingers).

Between t = 8 min and t = 50 min, the neighboring plumes compete for the supply of water rich fluid from within the mush surrounding and the fingers start to decrease in number. At t = 50 min all fingers have subsided and four vigorous plumes can be seen. These plumes are located right above the nucleators and remain there until the end of the experiment.

All temperature maps presented up to this point were taken using two 8-bit Pulnix cameras. As mentioned before in the noise analysis section (3.1.7), using Pulnix cameras resulted in 0.8°C uncertainty in instantaneous temperature measurement (with no filtering in time and space). The two PixelFly cameras, with described specifications, were used to carry out the rest of the experiments because of their better noise characteristic and resolution.

A smaller region above a nucleator was selected for temperature measurement in order to better characterize the temperature of the fingers (Figure 5-11). Figure 5-12 shows temperature maps of the solution during the solidification process using new Pixelfly cameras over this imaged area. The imaged area is 3×2.2 cm^2 and located above the second nucleator on the second row. The bottom left corner of the image is at (31mm, 26mm, 7mm). The spatial resolution of the instantaneous measurement (with no filtering in time and space) in the plane of illumination is, therefore, 21 μm per pixel. The origin as shown in Figure 5-11 is located at the front bottom left corner of the test section.

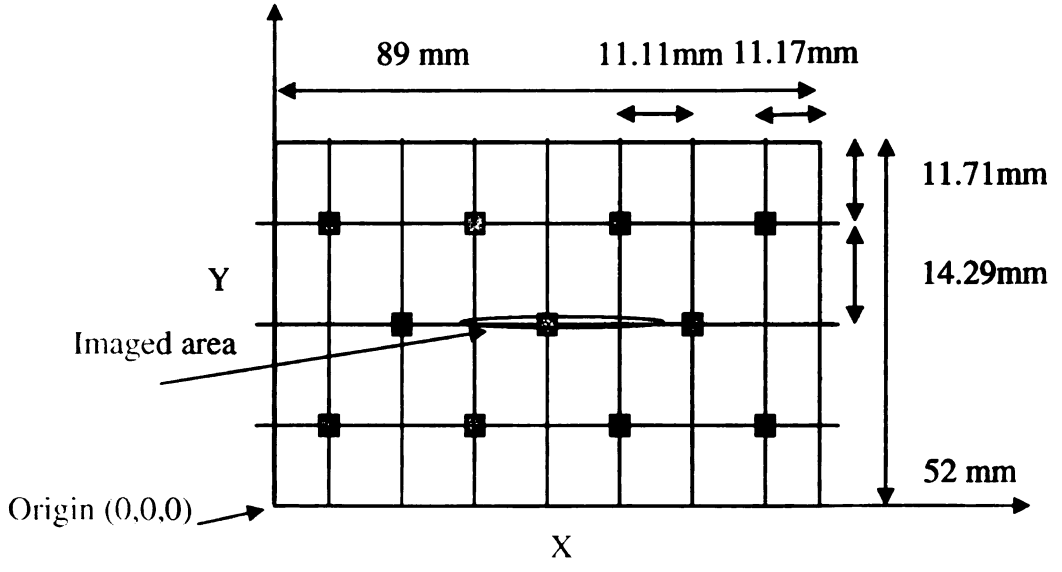

Figure 5-11: The location of the origin and the imaged area

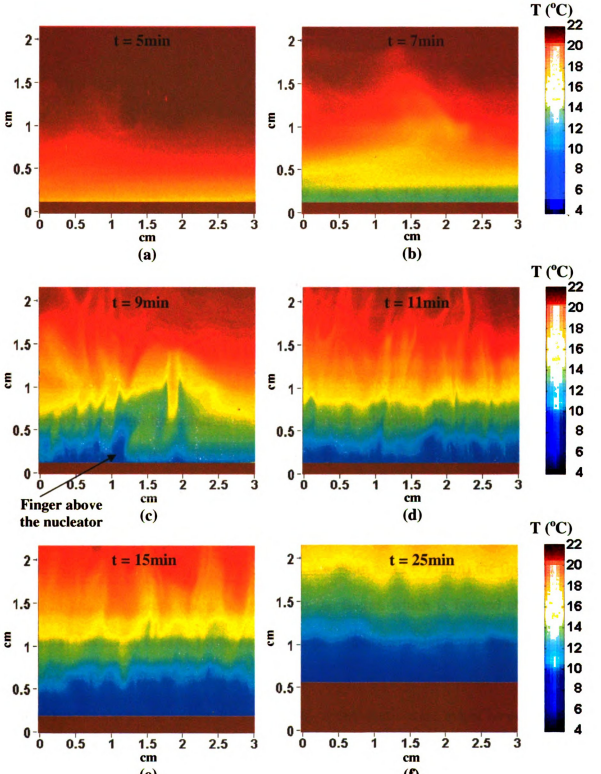

Figure 5-12: Temperature maps of the imaged area (3×2.2 cm^2), averaged in time (4 images) and averaged in space (8×8pixels)

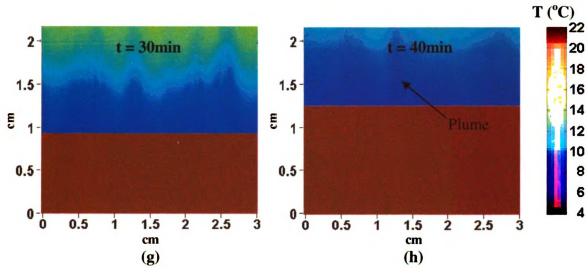

Figure 5-12: Temperature maps of the imaged area (3×2.2 cm^2), averaged in time (4 images) and averaged in space (8×8pixels)

These images show the temperature characteristic of the fingers at initial stages of the solidification process. At t = 5 and t = 7 min, temperature maps show simple diffusion of the temperature into the solution and no temperature characteristic of the fingers can be seen, even though the bottom plate is entirely covered with dendrites. Since the imaged area is 7 mm above the bottom plate, the fingers are short in length and small in velocity at the early stages; therefore, the temperature characteristics of fingers don't show up in the temperature maps. Later in time (t = 9min and t = 11min) the fingers can be seen in the temperature maps. It seems that the finger, which is formed above the nucleator at this stage, is more pronounced because of a higher solidification rate around the nucleator. Due to the formation of the plume out of the laser sheet, the temperature characteristic of the plume cannot be seen clearly in the temperature maps; however, the shadow of the plume is presented in the Figure 5-12 (h) above X = 1.3 cm. It should be noted again that the red solid region on the bottom of the temperature maps represents the mushy zone plus the dark area below the laser sheet.

Chapter 6

Comparison between numerical results and LIF results

In the literature, the issue of the temperature field in and around the plumes has not been the topic of many studies. One reason is that there has not been an existing measurement tool to measure in-situ temperature quantitatively. The task of this work is to use the measured thermal boundaries of the plume and predict the temperature distribution across the plume at different heights right above the mushy zone with numerical simulation. The results from this simulation will be compared with LIF temperature data. Hellawell *et al.* (1993) explained in their study the idea of an analytical approach which described the velocity profile associated with plumes. Following that work, Wirtz (1998) obtained the velocity profile by assuming a balance between buoyancy and friction forces in the momentum equation using appropriate boundary conditions. In this section, the energy equation will be solved numerically, based on some assumptions, and the data of this simulation will be compared to the results of the LIF experiment.

6.1 Assumptions

In order to solve the energy equation, the following assumptions are made

1) **The flow is steady (not time dependent).** This assumption is valid late into the experiment when the velocity and temperature variations are very small (t > 60min).

2) **The flow is assumed to be one dimensional flow (only one component of velocity V_z exists, therefore it is fully developed (no entrainment, Wirtz (1998)).**

3) **The plume is moving upward on a straight line.** This assumption is valid for regions very close to the mush-melt interface.

4) **The physical properties are assumed to be constant.**

5) **Average concentration across the plume is constant along the plume.** Since the Lewis number is large (small solutal diffusivity), the plume retains its compositional identity.

6) **Symmetry around z axis.**

6.2 Governing equations

The governing equations for the flow shown in Figure 6-1 can be written as

Continuity:

$$\cancel{\frac{\partial V_r}{\partial r}}^{0} + \cancel{\frac{V_r}{r}}^{0} + \frac{\partial V_z}{\partial z} = 0 \rightarrow V_z = f(r) \qquad (6\text{-}1)$$

Assuming the flow to be one dimensional dictates that V_z = f(r); therefore, the flow is fully developed. Velocity profiles of a plume at different heights obtained by Lum (2001) using the MTV technique showed that the velocity profile of the plume near the mush-melt interface for short distances (3mm) along the plume does not change with height (Figure 6-2). It is assumed that these results are valid for longer distances (1.1 cm).

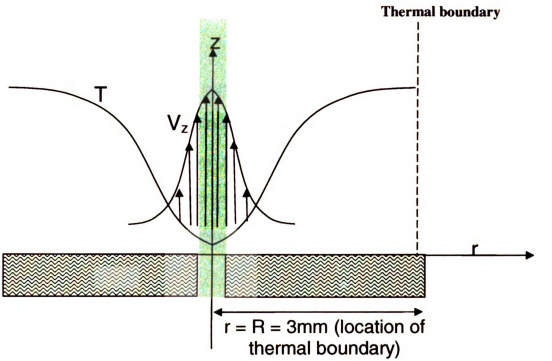

Figure 6-1: Schematic of the plume exiting the mushy zone

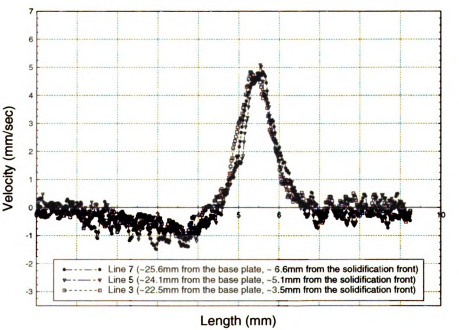

Figure 6-2: Velocity Profile of the Plume at different heights at t = 60 min (Chee Lum 2001)

Momentum:

Even though the result from this section is not used in this numerical analysis, the momentum equation will be simplified to show how Wirtz (1998) obtained the final simplified differential equation for the velocity profile of the plume. Using the Boussinesq approximation (last two terms in eq (6-2)) and assuming asymmetric flow, the z-momentum equation can be written as

$$\overset{0}{\cancel{V_r \frac{\partial V_z}{\partial r}}} + V_z \overset{0}{\cancel{\frac{\partial V_z}{\partial z}}} = \nu \left(\frac{\partial^2 V_z}{\partial r^2} + \frac{1}{r}\frac{\partial V_z}{\partial r} + \overset{0}{\cancel{\frac{\partial^2 V_z}{\partial z^2}}} \right) + \underline{g\beta_T (T - T_\infty)} + \underline{g\beta_C (C - C_\infty)} \qquad (6\text{-}2)$$

The last two terms in equation (6-2) show how the buoyancy forces, which drive the plume upward, are related to temperature and concentration differences. β_T and β_C are the volumetric thermal and solutal expansion coefficients. These thermodynamic properties of fluid provide a measure of the amount by which the density changes in response to changes in temperature and concentration under constant pressure.

From continuity $V_r = 0$ and $\partial V_z / \partial z = 0$. Since β_T is 10 times smaller than β_C for ammonium chloride solution and $\Delta T \approx \Delta C$ ($\Delta T \approx 2^oC$, base on our findings and $\Delta C \approx 2\%$ wt, specified by Hellawell *et al.* 1993), the thermal buoyancy force can be neglected compared to the solutal buoyancy force. Therefore, the momentum equation can be simplified as

$$\nu \frac{1}{r}\left(\frac{\partial}{\partial r}\left(r \frac{\partial V_z}{\partial r} \right) \right) = g\beta_C (C - C_\infty) \qquad (6\text{-}3)$$

where β_C is the solutal expansion coefficient and $(C-C_\infty)$ is the concentration difference between the plume and the surrounding fluid. Since the solutal diffusivity is very small ($\alpha_c = 1.3\times10^{-9}$ m^2s^{-1}), one can conclude from the species equation a uniform concentration across the plume, and the right term in the above equation is a constant. Therefore, the velocity V_z can be obtained by integrating the above equation. Wirtz (1998) used the exact same equation to obtain the velocity profile of the plume by using some experimental results and appropriate velocity boundary conditions. The velocity profile resulting from the above differential equation is not parabolic since the buoyancy term $(C-C_\infty \approx 0)$ outside of the plume is equal to zero (Wirtz, 1998).

In this study the analytical velocity profile obtained from the integration of the above equation cannot be used since the exact value of $(C-C_\infty)$ is unknown. However, the velocity profile obtained experimentally by Lum (2001) will be used to solve the energy equation in the next step.

Energy equation:

Assuming axially symmetrical flow, the energy equation can be written as

$$\overset{0}{\cancel{V_r}}\frac{\partial T}{\partial r} + V_z\frac{\partial T}{\partial z} = \alpha\left(\frac{\partial^2 T}{\partial r^2} + \frac{1}{r}\frac{\partial T}{\partial r} + \frac{\partial^2 T}{\partial z^2}\right) \qquad (6\text{-}4)$$

Neglecting conduction along the plume in the z direction, the energy equation can be written as the following:

$$V_z(r)\frac{\partial T}{\partial z} = \alpha\left(\frac{\partial^2 T}{\partial r^2} + \frac{1}{r}\frac{\partial T}{\partial r}\right) \qquad (6\text{-}5)$$

where α is the thermal diffusivity of the ammonium chloride solution. This partial differential equation can be solved numerically by knowing the boundary conditions and velocity profile $V_z(r)$ that was obtained by Lum (2001) experimentally.

6.3 Boundary conditions

Boundary conditions for the flow field shown in Figure 6-1 can be written as

$$T = T(r) \qquad @ \quad z = 0$$

$$T = T(z) \qquad @ \quad r = R$$

$$\frac{\partial T}{\partial r} = 0 \qquad @ \quad r = 0$$

R is the distance between the thermal boundary and the center of the plume. Figure 6-3 shows the temperature map of the plume right above the mushy zone at t = 60 min. Temperature profiles T(r) and T(z) are extracted from this temperature map. The location of the imaged area and the dimensions (2.5 × 1.9 cm^2) of this temperature map were discussed in the previous chapter (Figure 5-4 (l)). The locations of the corresponding boundary conditions are also shown as dashed lines. The vertical thermal boundary is placed at a location where the horizontal temperature profiles of the plume become flat (3mm away from the center of the plume). The temperature along the horizontal line, found experimentally at z = 0, is T = 8.4° C, except in the plume region where T = 7.8° C. The temperature profile, found experimentally along r = 3mm, is shown in Figure 6-4. A second-order polynomial function is used to curve fit the temperature data. Velocity $V_z(r)$ is found by curve fitting a velocity data set in Figure 6-2 obtained by Lum (2001)

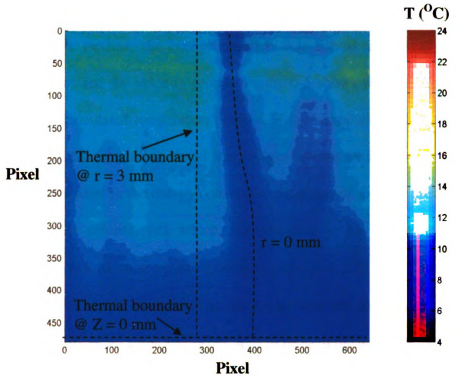

Figure 6-3: Temperature map of the plume exiting the mushy zone (t=60 min)

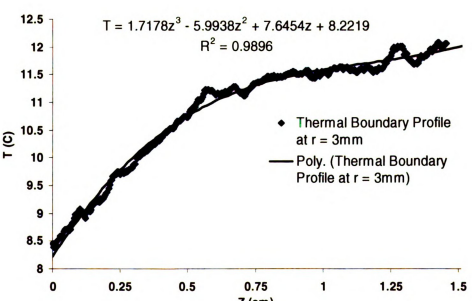

Figure 6-4: Measured temperature profile plus polynomial fit along the vertical line at r = 3mm (3.5 mm above the mushy zone).

6.4 Results and discussion

Using Euler's method, the energy equation was solved numerically with given boundary conditions and the velocity profile. Figure 6-5 shows the comparison between the measured and calculated temperature profiles of the plume along the center line. As can be seen, the measured and calculated temperature profiles are in good agreement. The only unknown parameter in the energy equation is the value of thermal diffusivity of the ammonium chloride solution (α), which was assumed to be constant. The thermal diffusivity of the 26% wt ammonium chloride is about $\alpha = 1.45 \times 10^{-7}$ m^2/s. In Figure 6-5, temperature profiles of the plume at the center line are plotted for two different values of α (1.4×10^{-7} m^2/s, 1.7×10^{-7} m^2/s). As can be seen the temperature profile is not very sensitive to the value chosen for α and both profiles are in good agreement with the experimental result. Figure 6-6 shows the comparison between measured and calculated temperature profiles across the plume at different heights. The slight deviation of the temperature profile for positive r is due to the fact that on the right hand side of the plume (seen in Figure 6-3), a finger was about to form in the plane of the measurement. Therefore, the measured temperature values of the plume are lower compared with those of the calculated values. The overall agreement between measured and calculated temperature profiles (from a simplified model) is good. These results show that the temperature profiles of a plume can be obtained for short distances along the plume using the described simplified model if appropriate boundary conditions are given.

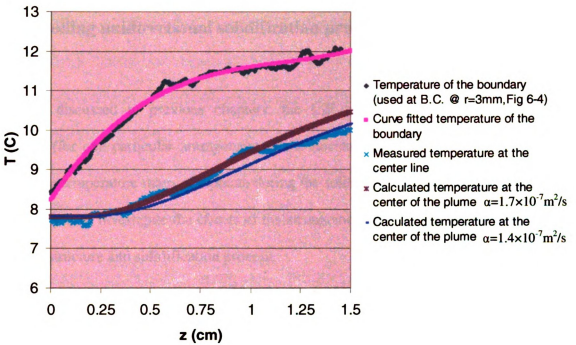

Figure 6-5: Comparison between measured and calculated temperature profiles at the center of the plume

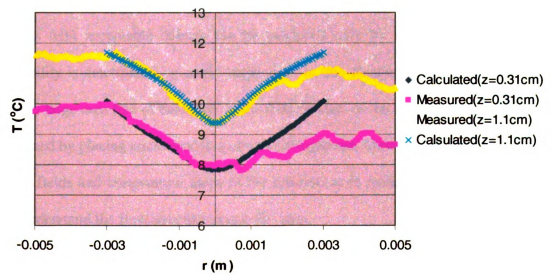

Figure 6-6: The comparison between measured and calculated temperature profiles across the plume at different heights

Chapter 7

Controlling unidirectional solidification processes using nucleators

As discussed in previous chapters, the LIF technique in combination with nucleators (for one particular arrangement of the nucleators, Wirtz, 1998) was used to quantify the temperature maps of a plume during the solidification process. The objective of this study is to investigate the effects of the arrangement and size of the nucleators on the plume structure and solidification process.

Quantitative measurements of the velocity profiles and temperature maps will be made using described diagnostic techniques to enhance our understanding of the effect of these arrangements on flow structures during the solidification process. A buoyancy-induced fluid flow, which is primarily responsible for most forms of macro-segregation (chimneys), is not easily controllable. If left uncontrolled, natural convection will contribute to nonuniform distributions of alloy constituents and grain structure in casting. Materials with acceptable defects can be produced only by trial-and-error, and their acceptability is determined by costly inspection. In this chapter, it will be shown that a relatively large area free of chimneys in the final product of the solidification process can be obtained by placing nucleators in a certain arrangement. Quantitative measurements of velocity fields and temperature maps of the solution were made for this arrangement to better understand the flow structure above this area.

7.1 Effect of size and arrangement

The shape of the test section was essentially described in previous chapters and consisted of 1/4" quartz glass measuring 52 × 89 × 100 mm placed over a stainless steel base plate (430 stainless steel). Small nucleators measuring 1.59 × 1.59 × 3.19 mm in size and big nucleators measuring 3.19 × 3.19 × 3.19 mm in size were made of Neodymium rare-earth magnets. Magnets were chosen to be nucleators so that they could be arranged and placed easily on the stainless steel bottom plate.

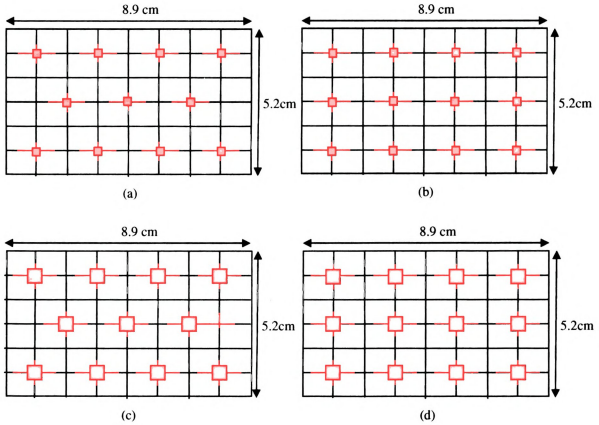

Figure 7-1: Different arrangements. (a) First arrangement with small nucleators, (b) Second arrangement with small nucleators, (c) First arrangement with big nucleators and (d) Second arrangement with big nucleators

To examine the effects of the size and arrangement of the nucleators on the solidification process of ammonium chloride, two different arrangements were used in the following experiments. The first arrangement with small nucleators, as shown in Figure 7-1(a), is the same as that used by Wirtz (1998) in his experiment. A second arrangement with small nucleators as shown in Figure 7-1(b), is used with that of Wirtz (1998) for the purpose of comparison. Figure 7-1(c) and Figure 7-1(d) show the first and second arrangement with big nucleators.

A detailed study of the general features of the solidification process of the ammonium chloride has already been described in the second chapter. Four minutes into the solidification process, small fingers started to form around the nucleators and could be seen rising. This was true for all nucleator arrangements. In the case of the first arrangement with small nucleators (Figure 7-1[a]), eleven chimneys and plumes were formed above the nucleators as expected. This is consistent with Wirtz's (1998) observation.

Figure 7-2 shows the top view of the mushy zone. The white region is the surface of the mushy zone and the dark spots are the chimneys. As can be seen, the eleven chimneys (marked with red circles) were formed above the nucleators. The second arrangement with small nucleators exhibited different behavior of the flow compared to that of the first one, even though they were only slightly different. Not all the chimneys and plumes formed above the nucleators in this arrangement (Figure 7-1[b]). As seen in Figure 7-3, four out of the twelve chimneys (marked with blue circles) formed randomly in the test section. Even though the two arrangements are only slightly different, the

results turned out to be completely different. These simple tests illustrated that the arrangement of the nucleators plays an important role during the solidification process.

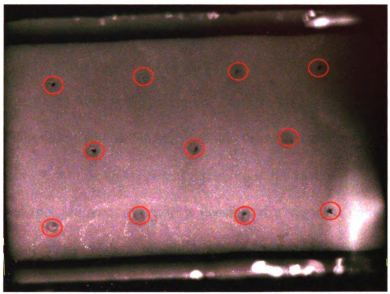

Figure 7-2: Top view of the mushy zone for the case of first arrangement with small nucleators (t = 120 min)

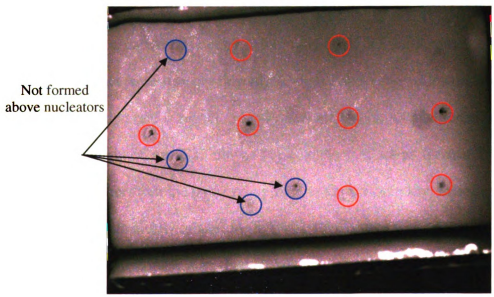

Figure 7-3: Top view of the mushy zone for the case of second arrangement with small nucleators (t = 120 min)

By keeping the same arrangement (second arrangement) but using the big nucleators (Figure 7-1 (d)), plumes and chimneys could be forced to form above the nucleators. Figure 7-4 (a) shows the location of these chimneys and, as can be seen, they were well arranged above the nucleators. This experiment clearly showed that with a bigger nucleator, more perturbation at the location of the nucleator is induced and, therefore, a plume tends to form at that location. This can be seen clearly in Figure 7-4 (b). As shown in the early stages, fingers that are formed at the mush-melt interface above the nucleators seem to be stronger and thicker than the rest of the fingers. Chen *et al* (1994) concluded that plume convection is possible if a vigorous enough salt-finger convection is present along with a mushy layer of large permeability. Sample and Hellawell (1984) reported that they could create a new plume, and from that a new chimney, by lowering down an open capillary to within 1 to 2 mm of the growth front and extracting some liquid up the tube. These fingers behave very similar to that of the capillary tube. Since these fingers are stronger, they entrain more liquid at the mush-melt interface, creating a convective circuit within the bulk liquid and interdendritic liquid. It should be noted that these stronger fingers are formed above the nucleators due to the fact that the solidification rate is higher around these nucleators. As mentioned before, these nucleators are made of metallic alloys. These nucleators act as thermal fins and they enhance heat transfer from the surrounding fluid to the bottom plate, therefore enhancing the solidification rate locally around them. These fingers also look thicker in comparison to those above the small nucleators (Figure 2-6).

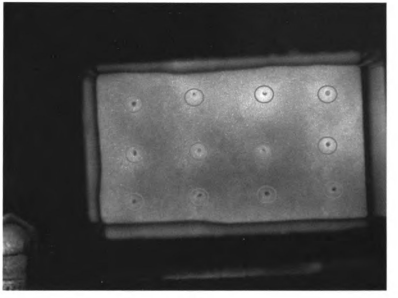

(a)

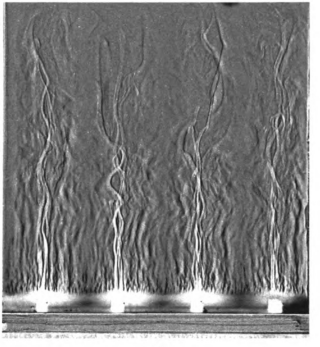

(b)

Figure 7-4: (a) Top view of the mushy zone for the case of second arrangement with big nucleators(t = 120 min), and (b) Front view (t = 10min)

7.2 Effect of spacing

To examine the effect of nucleator spacing on the plume structure, two different arrangements were used in the following experiments. Either one pair (Figure 7-5 [a]) or two pairs (Figure 7-5 [b]) of nucleators were used. In the case of two pairs, the pairs of nucleators were placed far enough apart (h > 3cm) so that one pair did not influence the other. Different experiments were carried out by changing the spacing, L, between the nucleators. It was generally observed that when the two nucleators were close to each other, the plumes generated above them were always phase locked with 180° phase difference (Figure 7-6). The reason for phase locking was due to the coupling between nearby jets. Entrainment of fluid and counter-propagating shear flow produce dynamical instabilities, and results in synchronization of phases of the nearby plumes (Dombrowski *et al.* 2004). Based on experimental results obtained by Dombrowski *et al.* (2004), it is speculated that phase locking of the plumes (with 180° phase difference) occurs when the two adjacent plumes have the same Reynolds number, and they are identical. The temperature and velocity profiles across these phase locked plumes, found experimentally, will be shown later.

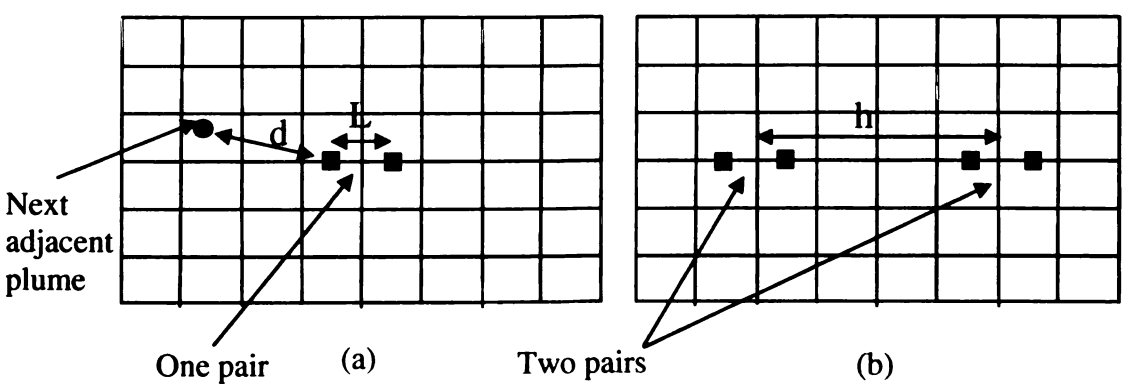

Figure 7-5: (a) One pair of nucleators, and (b) Two pairs of nucleators

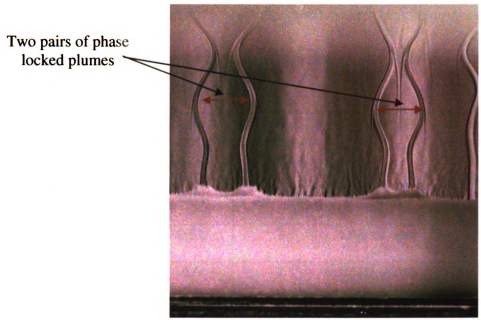

Figure 7-6: Phase locking of two nearby plumes, test # 7 (180^{o} phase difference)

Some of the experimental results are summarized in Table 7-1 with the first and the second columns containing the test number and the size of each pair. The third column indicates the distance between nucleators of each nucleator pair. The fourth column indicates whether two plumes were generated or only one was formed on each pair of nucleators. The fifth column shows whether the two generated plumes were phase locked or not, and the sixth column illustrates the time the phase locking occurred (before this locking time, two fingers or two plumes existed with no clear relationship between their phases). The last column represents the shortest distance (d) between a next adjacent plume and one of the plumes formed on the pair of nucleators (Figure 7-5[a]). It should be noted that the two adjacent plumes are phase locked with 180^{o} phase difference as long as a third randomly formed plume is far way from them; otherwise, there would be no clear relationship between their phases. It should be noted that every single arrangement was carried out four times to make sure that the results are repeatable.

Table 7-1: The summary of some of experiments carried out for pairs of nucleators

Test #	Test on Nucleators	Distance apart L (cm)	Final number of plumes	Phase status	Time when phase locking occurred (min)	d (cm)
1	A pair of big ones	0.42	1 oscillatory			1.2
2	A pair of big ones	0.52	2	Locked and 180°	30	1.6
3	A pair of big ones	0.6	2	Locked and 180°	35	1.21
4	A pair of big ones	1	2	Not Locked		0.8
5	A pair of small ones	0.6	1 oscillatory			1.19
6	A pair of small ones	1	2	Locked and 180°	35	1.31
7	Two pairs of big ones	0.52 0.76	2 2	Locked and 180°	30 30	1.4 1.67
8	A pair of big ones A pair of small ones	0.46 0.48	1 1			1.24 1.25

From Table 7-1 and other observations, the following results were concluded:

For a pair of small nucleators:

If the distance between nucleators of each pair was less than about 0.6 cm, only one plume was formed on one of the nucleators. The transition from fingers to plume formation was either oscillatory or non-oscillatory. In oscillatory mode, initially two fingers were formed above the nucleators. Later in time, one of the fingers on the first nucleator disappeared while the other one on the second nucleator was still ascending.

After some time, the finger that had disappeared grew back again on the first nucleator. This process only repeated itself once or twice. The finger that survived became a plume later in time. Figure 7-7 shows the sequence images of the oscillatory mode of test # 5. Initially, two fingers were formed above the nucleators. Later in time, one of the fingers on the left nucleator disappeared while the other one on the right nucleator was still ascending (t = 12 min). After a while (t = 16 min), the finger that disappeared grew back again on the left nucleator. At t = 18 min this finger started to get weaker again and disappeared at t = 20 min. The finger that survived became the plume on the right nucleator.

In non-oscillatory mode, two fingers grew initially and later one disappeared while the other remained and later formed a plume until the end of the experiment. Most of the time, for distances in the range of 0.6 cm $\leq$ L $\leq$ 1.2 cm, two plumes were formed above the nucleators. If the distance between the next adjacent plume and one of these plumes was larger than d = 1.2 cm, then the plumes on the pair of nucleators were always phase locked with 180^{o} phase difference and had the same amplitude of oscillation until the end of the experiment. If another plume randomly formed closer than d = 1.2 cm to the pair of plumes, the phase between the plumes was no longer locked. They were out of phase until the end of experiment. The coupling of nearby plumes becomes complicated with the existence of the third plume.

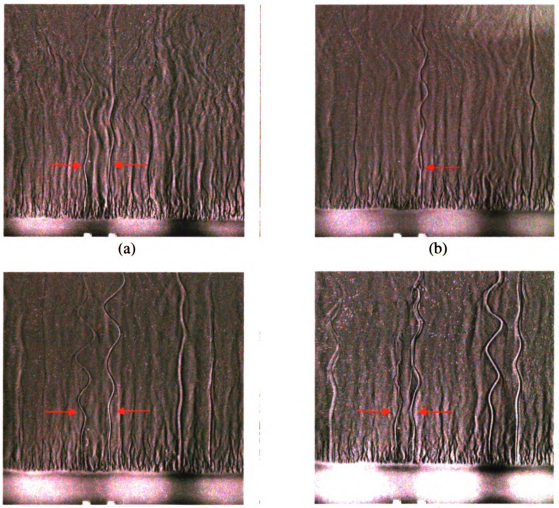

Figure 7-7: Sequence images of the oscillatory mode. (a) t = 8min, (b) t = 12min, (c) t = 16 min and (d) t = 18 min

For a pair of big nucleators:

The results for pairs of big nucleators are similar to those for small ones, except that the minimum distance between nucleators that can generate two separate plumes becomes shorter (L = 0.5 cm). This indicates that the bigger the nucleators are, the closer they can be brought to obtain two separate plumes. The summary of the conclusions is written in Table 7-2.

Table 7-2: The summarized conclusions

Big nucleators 3.19 x 3.19 x 3.19 mm	**Small nucleators 1.59 x 1.59 x 3.19 mm**
One plume oscillatory or non-oscillatory when $L \leq 0.5$ cm	One plume oscillatory or non-oscillatory when $L \leq 0.6$ cm
Two Plumes Phase locked with the same amplitude when $0.5 \text{ cm} \leq L \leq 1.2$ cm	Two Plumes Phase locked with the same amplitude when $0.6 \text{ cm} \leq L \leq 1.2$ cm
No relationship between phases and amplitude. They don't see each other when $1.2 \text{ cm} \leq L$	No relationship between phases and amplitude. They don't see each other when $1.2 \text{ cm} \leq L$
Not phase locked with different amplitude of oscillation When $d < 1$ cm	Not phase locked with different amplitude of oscillation When $d < 1$ cm

As ammonium chloride solution crystallizes, the height of the mushy zone increases, which reduces the weight percentage of the solute. The height of the mushy zone with time for some of the tests in Table 7-1 is provided in Figure 7-8. The height of the mushy zone at a given time is measured to be the distance from the base stainless steel plate to the average location of the mush-melt interface. It is clear from this figure that all of the experiments carried out had the same solidification growth rate. Even though the spacing and the size of the nucleators is different from one test to another, the resulting mushy growth rate is about the same for all of them. It should be noted that in these tests only two or four nucleators were placed on the bottom plate and plumes associated with them were forced to form above them. The rest of the plumes were free to form randomly anywhere in the test section.

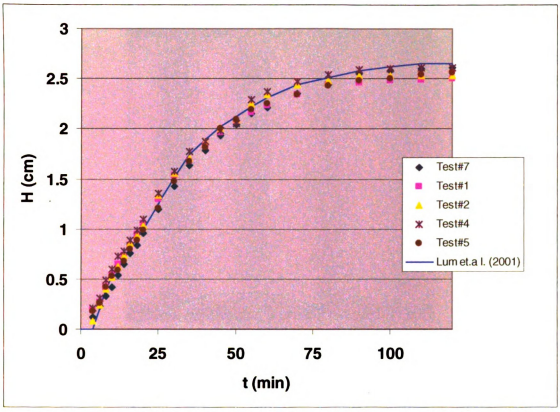

Figure 7-8: Height of mushy zone vs. time

In order to verify the previous conclusion regarding the phase locking of two adjacent plumes, an experiment was carried out by placing 7 equally spaced big nucleators in a row as shown schematically in Figure 7-9. The front view is shown in Figure 7-10.

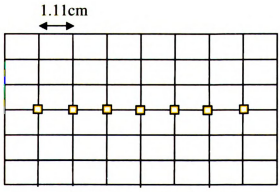

Figure 7-9: Schematic top view of one row of nucleators

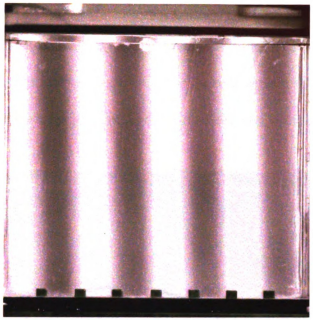

Figure 7-10: Schematic front view of one row of nucleators

As expected, initially (t = 6 min), some fingers that are stronger (more water rich fluid) than the rest of the other fingers were formed above the nucleators and can be seen in Figure 7-11.

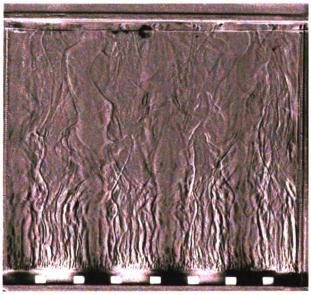

Figure 7-11: Stronger fingers were formed above the nucleators compared to others formed at mush melt interface at t = 6 min

These fingers became plumes at t = 20 min; however, some remained out of phase. Figure 7-12 shows these plumes at t = 30 min, where some were out of phase and the amplitudes were different. Other plumes seen in the test section were formed randomly (since only seven of the eleven plumes are controlled, the rest will form randomly).

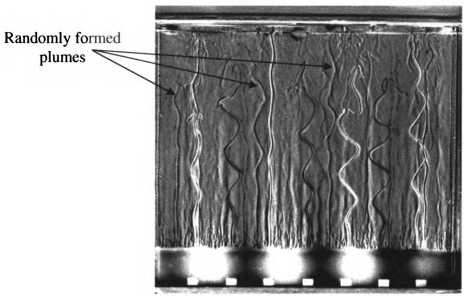

Figure 7-12: Plumes were formed above the nucleators (t = 30 min)

At t = 35 min these plumes started to become equal in amplitude, but with 180° phase difference with respect to each other. This is shown in Figure 7-13. At t = 40 min these 7 plumes are equal in amplitude, but 180° out of phase. They remained phase locked until the end of the experiment. Figure 7-14 shows this phase locking at t = 70 min. Some of the randomly formed plumes disappeared and a new one formed after t = 40 min.

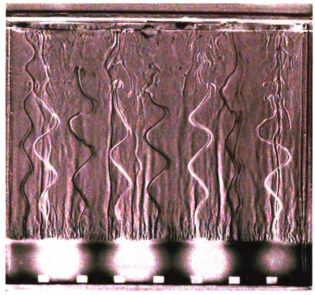

Figure 7-13: Plumes becoming phase locked (t = 35 min)

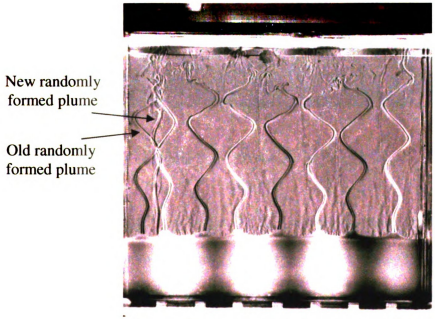

Figure 7-14: Plumes were phase locked at t = 70 min

As mentioned before, in the absence of nucleators, the experimental trial would yield approximately 11 chimneys within the test section. In this experiment, seven plumes were forced to be formed above the row of nucleators; therefore, the remaining plumes would be free to form randomly within the test section. Two additional chimneys associated with these plumes (seen on the left side of the Figure 7-14) were formed randomly within the test.

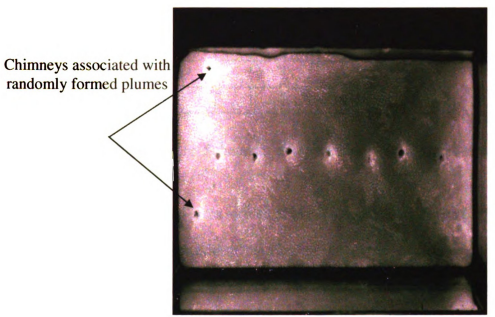

Figure 7-15: Top view of the chimneys

As can be seen clearly from Figure 7-15, 7 chimneys were formed above the row of nucleators. The reason the chimneys were not exactly in a straight line was due to the fact that the plume formation could occur at any location around the periphery of the nucleators. The two chimneys on the left side, which are not in the row, show the locations of the two randomly formed plumes described in Figure 7-14.

7.3 Obtaining relatively large area free of chimneys

In order to obtain a relatively large area free of chimneys and to push out the chimneys to the sidewalls, some big nucleators were placed at locations specified in Figure 7-16.

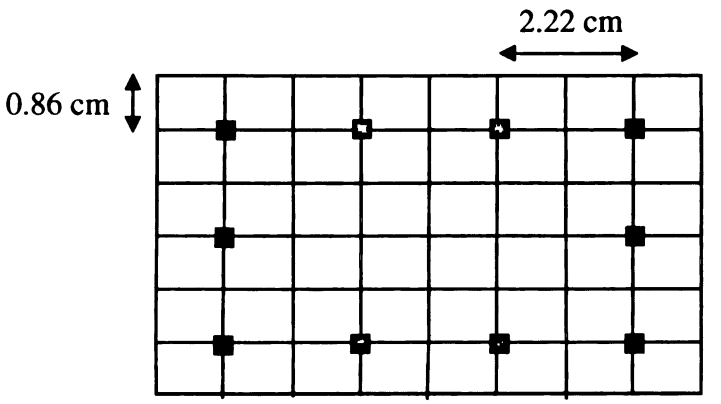

Figure 7-16: Schematic of the locations of the placed nucleators

In this case, ten plumes were formed above the nucleators as seen in Figure 7-17. A more uniform composition profile of the final product (free of chimneys) would be obtained over a relatively large area (6.66 cm × 3.44 cm). In the next chapter the temperature maps and velocity fields will be shown to qualitatively confirm this relative uniformity. This is an interesting result since materials with acceptable defects can be produced only by trial-and-error process development, or by costly inspection knowing the location of the defects (chimneys) has obvious economic and environmental benefits. Other researchers have used "artificial" means to redirect the formation of chimneys through rotation (Sample and Hellawell, 1982) or vibration (Garimella *et al*, 1995) of the test section. The advantage of the present use of nucleators in dictating the formation of the chimneys is that it is less intrusive and more cost effective in implementation.

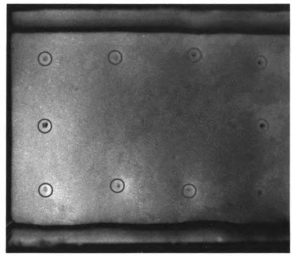

Figure 7-17: Top view of the chimneys

Another experiment was carried out by keeping the same number of nucleators and placing them slightly closer to the side walls (Figure 7-18). With the exception of one, all of the plumes formed above the nucleators; however, some more plumes were formed in the middle of the test section (marked with blue circles) as can be seen from the top view in Figure 7-19. A total number of 13 plumes formed during the solidification process.

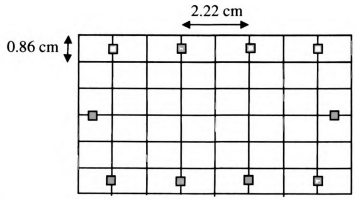

Figure 7-18: Schematic of the locations of the placed nucleators

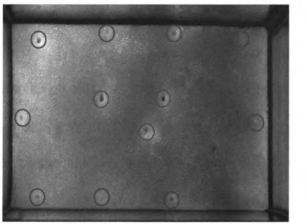

Figure 7-19: Top view of the chimneys

For this case, placing more nucleators on the periphery next to the other nucleators did not change the results. Still, some chimneys were observed in the middle of the test section. This experiment shows how sensitive the results are to the wall boundary condition and when the nucleators are placed very close to the side walls. The results presented in this study are valid for the case of 26% wt ammonium chloride solution cooled from below with a bottom temperature of -14^{o}C. It is obvious that changing any physical property of the fluid would affect these results. The size of an area free of chimneys that one can obtain depends on the pumping effect of the plumes (caused by buoyancy difference between the plumes and the surrounding fluid) and the permeability of the mushy zone. More pumping effect of the plumes and more permeability of the mush could result in a larger area free of chimneys by placing nucleators around the periphery of that area.

7.4 Average spacing between plumes

As mentioned before, based on our observations and other researchers' reports, the average spacing between plumes, in the absence of nucleators, is approximately 1cm. It should be possible to calculate in a quantitative manner the maximum area of the mushy zone around the plume that can provide the supply flow of water to the plume. From that, the average spacing between the plumes would be known.

Figure 7-20 shows a schematic of the proposed model. Since there is a continuous circulation in the system, it is necessary to identify the pressures that are available to drive the system. It is assumed that the flow is in steady state condition.

In Figure 7-20, P is the pressure, ρ_B is the bulk density of ammonium chloride solution, ρ_E is the density of the ammonium chloride solution at the eutectic point at the bottom plate and ρ_P is the density of the plume at the exit of the mushy zone. The radius of the chimney is r_1, and r_2 is the radius of the plume when it exits the chimney. The radius r_2 is larger than r_1 due to the expansion of the jet flow at the exit of the mush. The parameter 2L is the diameter of the source area. H is the height of the container and h represents the mushy zone height. Referring to Figure 7-20, it can be seen that the driving force for circulation must come from the total density difference between the plume and its surrounding fluid. The following equations can be written for this system:

the pressure balance can be expressed in terms of an identity equation

$$(P6-P1)+ (P5-P6) + (P3-P5) + (P2-P3) + (P1-P2) = 0 \qquad (7\text{-}1)$$

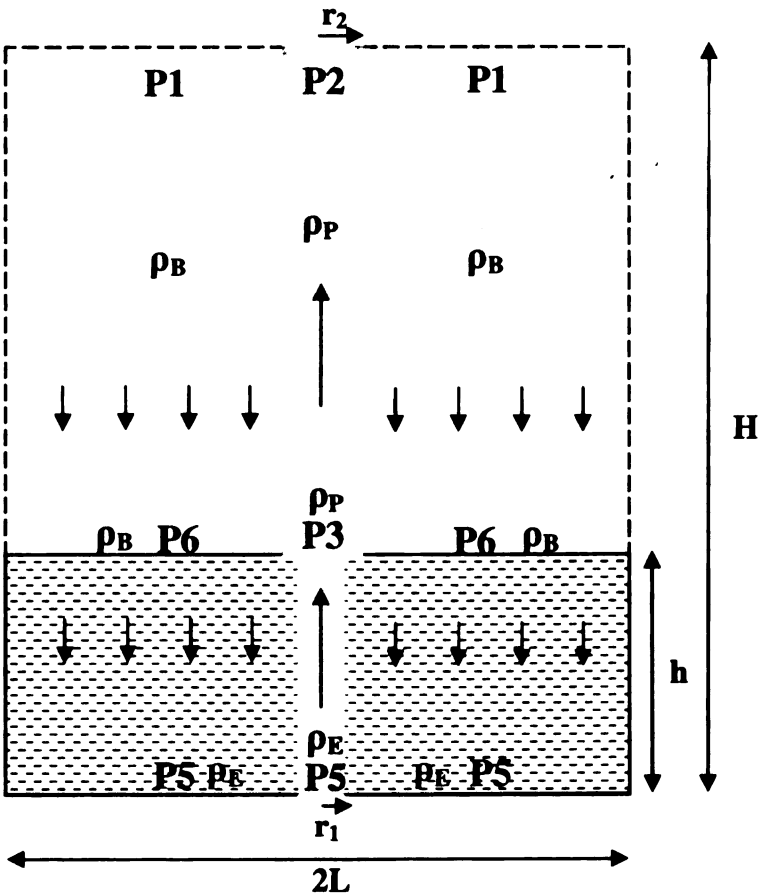

Figure 7-20: Schematic of the liquid circulation in the system

At the top of the container, the fluid is open to the ambient air. Therefore,

$$P2 \approx P1 \approx P_{atm} \tag{7-2}$$

Since the downward velocity of bulk fluid surrounding the plume is very small, we can assume that the pressure is dictated by the hydrostatic pressure, therefore

$$P6 \approx \rho_B g(H-h) + P1 \tag{7-3}$$

There is a pressure drop across the mushy zone due to its porous nature; therefore, from Darcy's law we have

$$P5 = P6 + \int_0^h \left(\rho_E + \frac{\rho_B - \rho_E}{h} z \right) g dz - \frac{Q\mu h}{\pi \left(L^2 - r_1^2 \right) K} \tag{7-4}$$

where K is the average permeability of the mush, Q the volume flow rate and μ is the viscosity of the ammonium chloride solution (assumed to be a constant everywhere in the test cell). The second term takes into account the hydrostatic pressure and it is assumed that the density is changing linearly across the mushy zone. The last term in eqution (7-4) is the pressure drop across the mushy zone and is obtained by integrating Darcy's law across the depth of the mushy zone. Assuming the plume is a flow in a circular pipe, the pressure drop along the plume in the mush can be found from Poiseuille's equation (Liu and Hellawell, 1999)

$$P3 = P5 - \int_0^h \left(\rho_E + \frac{\rho_P - \rho_E}{h} z \right) g dz - \frac{8 f Q \mu h}{\pi r_1^4} \tag{7-5}$$

Since the flow rate in the chimney varies from 0 to Q, the Poiseuille equation was modified by introducing a factor f, which varies from 0 to 1 in this region and can be seen in the second term of equation (7-5). The integral of this equation is based on the assumption that the density of the plume in the mushy zone varies linearly with height.

Assuming the plume is a flow in a circular pipe outside of the mushy zone, the pressure drop along the plume can be also found from Poiseuille's equation (Liu and Hellawell, 1999)

$$P2 = P3 - \rho_P g (H - h) - \frac{8 Q \mu (H - h)}{\pi r_2^4} \tag{7-6}$$

Substituting all equations into equation (7-1) yields

$$\rho_B g(H-h)+\int_0^h\left(\rho_E+\frac{\rho_B-\rho_E}{h}z\right)gdz-\frac{Q\mu h}{\pi\left(L^2-r_1{}^2\right)K}$$

$$-\int_0^h\left(\rho_E+\frac{\rho_P-\rho_E}{h}z\right)gdz-\frac{8fQ\mu h}{\pi r_1{}^4}-\rho_P g(H-h)-\frac{8Q\mu(H-h)}{\pi r_2{}^4}=0 \qquad (7\text{-}7)$$

which reduces to

$$(\rho_B-\rho_P)g(H-h)+\int_0^h\left(\frac{\rho_B-\rho_P}{h}z\right)gdz=\frac{Q\mu h}{\pi\left(L^2-r_1{}^2\right)K}$$

$$+\frac{8Q\mu(H-h)}{\pi r_2{}^4}+\frac{8fQ\mu h}{\pi r_1{}^4} \qquad (7\text{-}8)$$

the density difference (ρ_B- ρ_P) in equation (7-7) can be written in terms of a concentration difference as shown in equation(7-8). β is the volume solutal expansion coefficient; ρ_o is the reference density; ΔC is the concentration difference between plume and bulk fluid.

$$\rho_o\beta\Delta C(H-h)+\rho_o\beta\Delta C\,h/2=\frac{Q\mu h}{\pi\left(L^2-r_1{}^2\right)K}+\frac{8fQ\mu h}{\pi r_1{}^4}+\frac{8Q\mu(H-h)}{\pi r_2{}^4} \qquad (7\text{-}9)$$

$$\frac{Q\mu h}{\pi\left(L^2-r_1{}^2\right)K}=\rho_o\beta\Delta C(H-h)+\rho_o\beta\Delta C\,h/2-\frac{8fQ\mu h}{\pi r_1{}^4}-\frac{8Q\mu(H-h)}{\pi r_2{}^4} \qquad (7\text{-}10)$$

From equation (7-10), L can be estimated using available experimental data on the various parameters need in the model. The following parameters shown in Table 7-3 are used to calculate L.

Table 7-3: Parameters used to calculate L

Parameter	Value	Reference
H	10 cm	Lum (2001)
h	2 cm	Lum (2001)
Δc	4 wt%	Liu and Hellawell (1999)
μ	1.2×10^{-3} m^2s^{-1}	
ρ	1000 kg/m^3	
r_1	0.5 mm	Lum (2001)
r_2	1 mm	Lum (2001)
f	0.5	
Q	11 mm^3/s	Lum (2001)
β	2.82×10^{-3} $wt\%^{-1}$	Liu and Hellawell (1999)
K	2×10^{-9} m^2	Chen and Chen (1991)

Using specified parameters in table 3 results in

$2\times L = 1.0491$ cm

This result is in good agreement with meaured average spacing between plumes (1 cm). This work illustrates that the proposed simple model can be used to predict the spacing between plumes using available experimental data on the various parameters. It should be noted that most of the parameters used in this model can be measured easily using experimental methods. However, permeability K is a parameter that people have had difficulties in measuring experimentally. Keeping all the variables constant, Figure 7-21 shows the variation of the spacing 2xL with K (average permeability).

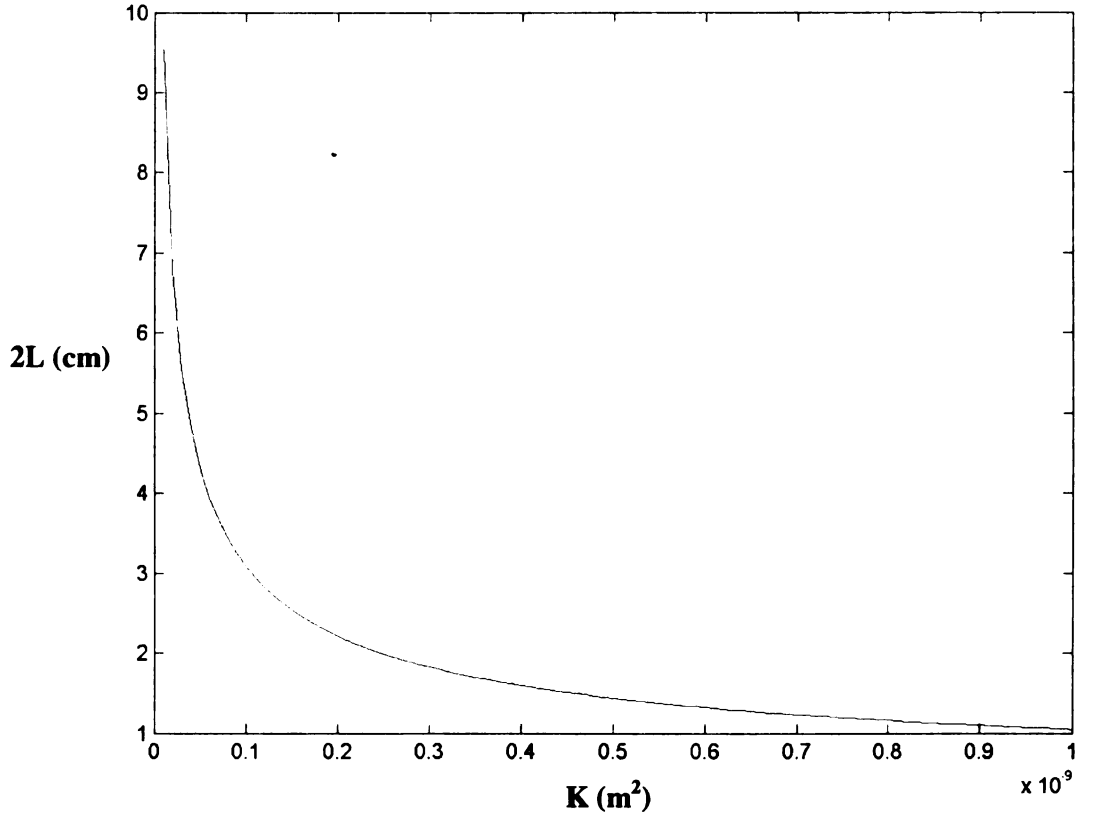

Figure 7-21: variation of the distance 2xL with K (average permeability)

This figure shows that as K decreases (resistivity to flow current increases), the distance L increases. To have the same pressure drop in the mushy zone, the velocity of flow in the mushy zone must decrease as resistivity to flow current increases. Therefore, a larger source is needed to feed the plume.

The average spacing between plumes can also be predicted based on stability analysis of the system. As described before, linear stability of a mushy layer analyzed by Worster (1992) in directional solidification showed two modes of convection. One, called the boundary-layer mode, is associated with the compositional buoyancy in a thin boundary layer above the mush-liquid interface (fingers). The other, called the mushy-layer mode, is driven by the buoyancy in the interior of the mushy layer (plumes). It was

also mentioned that once the mushy layer has become thick enough, it must become unstable to the mushy-layer mode; and it will do so irrespective of the pre-existence of the boundary-layer mode (fingers) of instability. In other words, the existence of fingers above the mush-melt interface does not cause the formation of the plumes inside the mushy zone. If this is true, then the formation of plumes can be explained in a simpler way. Imagine a porous layer with thickness of H that has a lower concentration of solution on the bottom and higher concentration of the solution on the top as shown in Figure 7-22. The flow in this region can become unstable in the presence of perturbations.

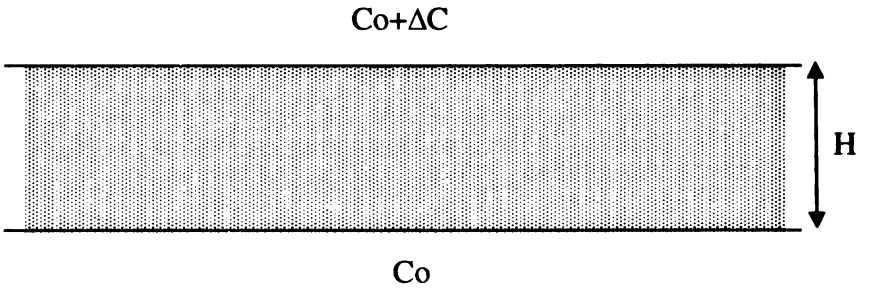

Figure 7-22: Two dimentional porous layer

The detailed analysis of this flow can be found in Bejan (1995) for a porous layer heated from below and cooled from above. Since the energy and solutal equations are similar, the analysis described in Bejan (1995) is also valid for this case. Assuming a linear concentration distribution across the porous layer, this flow is neutrally stable when

$$Ra_H = \frac{\left(n^2\pi^2 + \alpha^2\right)^2}{\alpha^2}$$

where Ra_H is the Rayleigh number based on H, $Ra_H = \frac{Kg\beta H\Delta C}{Dv}$ and α is the wave number of disturbances. K is an empirical constant called permeability, D is the effective solutal diffusivity of the medium, v is dynamic viscosity, β is the volume solutal expansion coefficient, and g is gravity.

The above equation says that the assumed disturbance (n,α) is likely to exist, neither growing nor decaying, if the Rayleigh number is as high as in the above equation. As Ra_H increases above zero, the first chance of flow convection materializes (minimum Ra_H) at n = 1 and $\alpha = \pi$ found by setting $\frac{\partial Ra_H}{\partial \alpha} = 0$. The minimum value of Rayleigh number for these values would be $Ra_H = 39.5$.

As shown in Figure 7-23 and mentioned by Bejan (1995), the disturbance (n = 1, $\alpha = \pi$) represents rolls with square cross-sections; that is, rolls whose horizontal dimension is equal to the porous layer thickness H. This means the average spacing between the plumes is more likely to be equal to the mushy zone thickness.

Experimental results obtained by Chen *et al.* (1994) showed that the onset of plume convection for different concentration of ammonium chloride solution occurred when the height of the mushy zone was about 1cm (our experimental observations confirm their results). Therefore, the average spacing of the plumes based on the above stability analysis should be 1cm. This is indeed in good agreement with experimental results that show the average spacing between plumes is approximately 1cm.

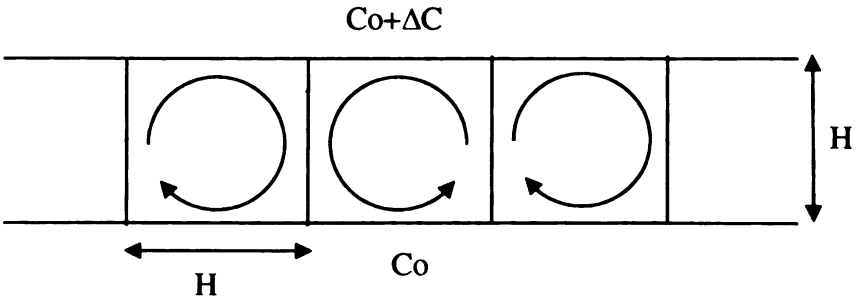

Figure 7-23: Rolls with square cross-sections for minimum Rayleigh number for neutrally stable cellular convection

Chapter 8

Temperature maps and velocity fields of some of the flow features for different arrangements of the nucleators

As mentioned before, the reason for phase locking with 180^{o} phase difference is believed to be due to the coupling between nearby plumes. To understand whether or not the two adjacent plumes are identical in their features and behavior, the temperature and velocity characteristics of two phase locked plumes with 180^{O} phase difference were quantitatively measured.

It was also proven in previous chapters that it is possible to obtain a relatively large area free of chimneys and plumes. The velocity vectors and temperature maps of the flow above this area will be studied to better understand the difference between the velocity vectors and temperature distribution of the flow above this area and that of randomly distributed plumes.

8.1 Temperature of phase locked plumes

To understand whether or not the two adjacent plumes are identical, temperature measurements of the plumes were made using the LIF technique for the cases of big-big and big-small nucleator pairs as shown in Figure 8-1. The spacing between nucleators was 1.1 cm. The imaged area is 3×4 cm^2, and the bottom left corner of the image has a coordinates of (29.5mm, 26mm, 28mm) with respect to the origin. The origin is located at the front bottom left corner of the test section. Figure 8-2 shows the location of the

imaged area at t = 70 min for the case of big-big nucleators at t = 70 min. The imaged area was 4mm above the mushy zone at this time.

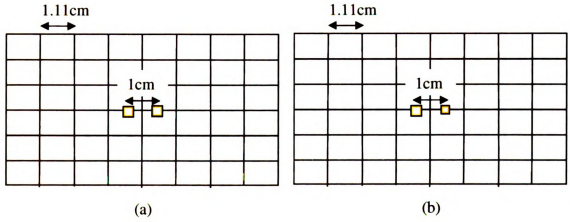

Figure 8-1: Schematic of the location of the nucleators (a) two-big nucleators and (b) big-small nucleators

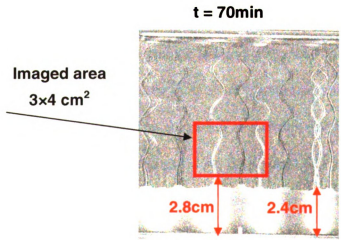

Figure 8-2: the location of the imaged area. (t=70min)

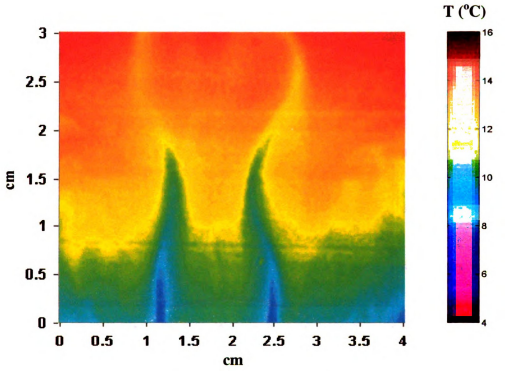

Figure 8-3: Temperature map of the plumes at t = 70 min for the case of two-big nucleators (average of 8×8 pixels)

Figure 8-3 shows a temperature map of two plumes at t=70min. Phase locking with 180° phase difference can be clearly seen in this figure. Since plumes rise vertically in helical motions, they move in and out of the laser sheet continuously. That is why the temperature characteristic of the plumes is less pronounced in the upper portion of this temperature map for heights greater than 3 cm (the temperature of the plumes slightly fades out in the upper portion). The animation of the temperature maps of the plumes, as they rise up, has been obtained and saved on an attached CD to this thesis. The duration of the movie is 5 seconds in real time. Temperature profiles of the plumes along horizontal lines on the laser sheet at different times are shown in Figure 8-4 for both cases (two-big and big-small nucleators). The locations of these lines are shown in Figure 8-5.

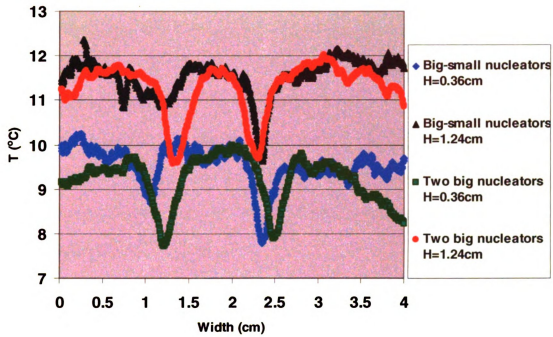

Figure 8-4: Temperature profiles along horizontal lines for two cases two big and big-small nucleators

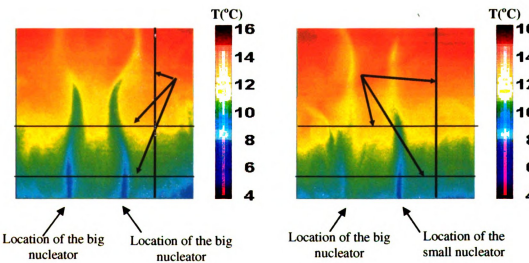

(a) Two big nucleators (t=70min)

(b) Big-small nucleators (t=70min)

Figure 8-5: Temperature profiles along designated lines

As can be seen in Figure 8-4, temperature profiles of two plumes are very similar for the case of big-big nucleators, which are shown with green and red dots for different heights. For the case of big-small nucleators, the plume on the big nucleator was formed slightly out of the laser sheet (The left plume in Figure 8-5 (b)) and temperature characteristic of the plume could not be obtained. However, by comparing the temperature profiles of the plume on the small nucleator (case (b)) with that of the plumes on the big nucleator (case (a)), one can see that they are similar, even though they were obtained from different experiments.

Temperature profiles along indicated vertical lines are shown in Figure 8-6. Since there is a good agreement in temperature profiles, it can be concluded that the solidification processes were similar for both cases.

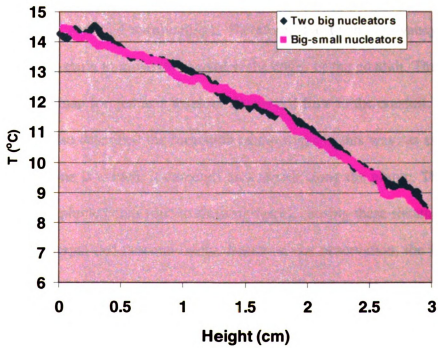

Figure 8-6: Temperature profiles along the indicated vertical lines

As mentioned before, one of the interesting features of the solidification process of ammonium chloride is falling wisps. In order to obtain a temperature map of these wisps, the temperature map of the plumes was obtained five seconds after the image in Figure 8-3 was taken. During this time plumes had ascended from below; and the bends had moved slightly upward. Therefore, the temperature characteristic of these wisps started to appear on the temperature map. Figure 8-7 demonstrates the temperature map of these wisps. As described by Dombrowski *et al.* (2004), the complex flow fields arise from remarkably simple ingredients. Due to the small solutal diffusivity of ammonium chloride, the water-rich plumes retained their compositional identity and moved upward. As the plume ascends into the density stratified surroundings, the entrained flow around the plume (jet) builds a conduit in which flow moves upward with the jet. However, as the heavier flow in the conduit moves upward, it encounters the surrounding fluid that is less dense (density stratified surrounding). Therefore, due to the buoyancy effect, the flow in the conduit starts to move downward at the edges of the conduit. The wisps seen in the temperature map formed as a result of downward flow in the conduit. Magirl and Incropera (1993) also described the formation of the wisps in this way: as salt-rich fluid adjacent to the plume is cooled, it descends as a sheath along the plume. These sheaths cannot traverse the plume bends (due to shearing force), causing these sheaths to separate from the plume (wisps) and descend freely. Based on our observation, the formation of these wisps is a combination of both phenomena described by Dombrowski *et al.* (2004) and Magirl and Incropera (1993).

The image of these wisps as obtained from a different experiment using the shadow graph technique is shown in Figure 8-8.

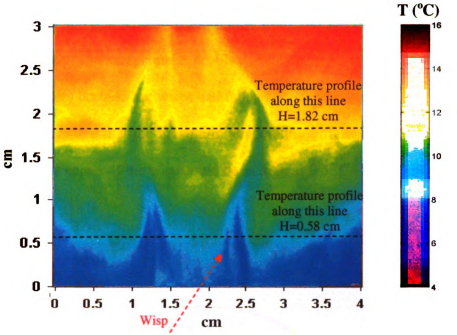

Figure 8-7: Temperature map of the plumes five seconds later

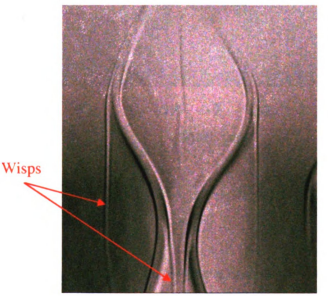

Figure 8-8: Shadow graph image of the plumes and wisps

Temperature profiles along the horizontal lines at different heights corresponding to Figure 8-7 are shown in Figure 8-9. The temperature profile of each plume has two

spikes in it. One spike is related to the plume itself and the other belongs to the wisp (blue dotted line). The temperature profiles of the wisps are not clear at H=1.82cm (yellow dotted line) because the wisps had fallen and were mixed with the solution. From Figure 8-9 one can see that the maximum temperature difference between the center of the plume and the center of the wisp could be as high as 0.5° C.

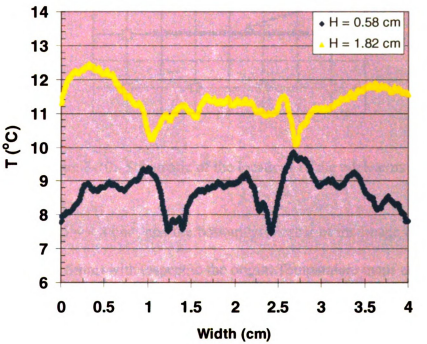

Figure 8-9: Temperature profiles along horizontal lines

8.2 Temperature measurement above the area free of chimneys

Up to now, temperature maps of the solution above the nucleators, where the plumes exist, were obtained and presented. In the previous chapter it was proven that by arranging the nucleators as shown in Figure 8-10, a relatively large area free of chimneys was obtained. In order to verify that a more uniform composition profile of the final

product of the solidification process can be obtained with such an arrangement of the nucleators, an experiment was carried out to measure the temperature of the solution above this area, which is free of plumes.

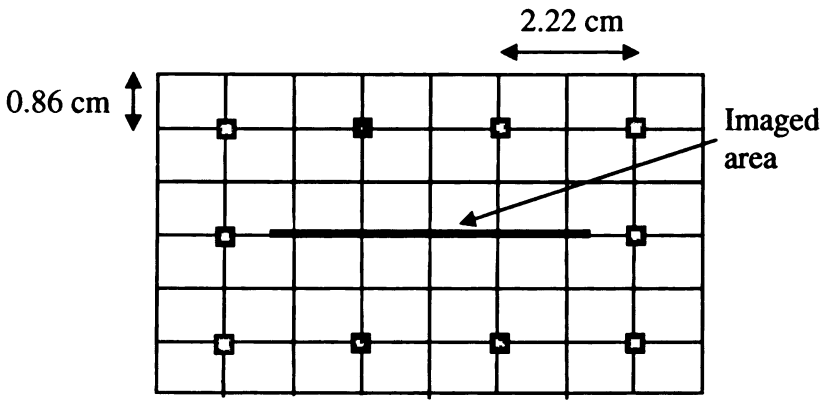

Figure 8-10: Schematic of the locations of the nucleators

The imaged area is 5.4×4 cm^2, and the bottom left corner of the image has a coordinate of (17.5mm, 26mm, 5mm) with respect to the origin. Temperature maps at different times are shown in Figure 8-11. At early stages of the solidification process, the temperature maps are very similar to those obtained above the nucleators in the previous chapters because fingers exist at mush-melt interfaces for all cases. However, after t = 60 min, the temperature becomes stratified and, unlike the previous cases, there is no signature of plumes in the temperature maps (Figure 8-11 (g)) and (h)). Since temperature is almost uniform laterally at this time, it is expected to produce a more uniform composition profile of the final product. The velocity fields associated with this area will be presented later.

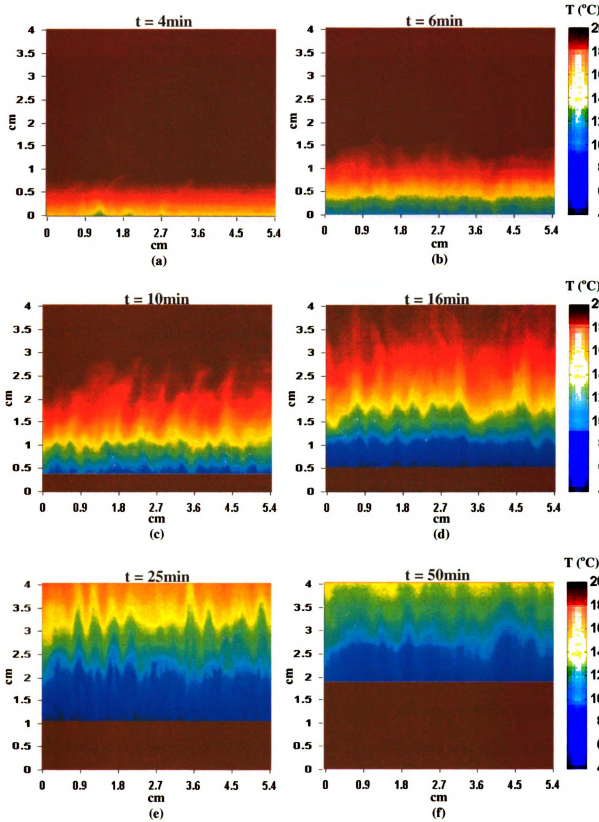

Figure 8-11: Temperature maps of the imaged area (5.4×4 cm^2, average of 8×8 pixels)

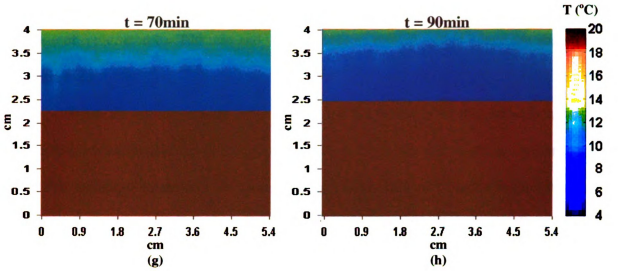

Figure 8-11: Temperature maps of the imaged area (5.4×4 cm^2, average of 8×8 pixels)

8.3 Velocity measurement around a single plume using Particle Image Velocimetry (PIV) technique

Detailed and accurate velocity measurements obtained by Lum (2001) for small regions of some plumes revealed some interesting flow features in and around those plumes. However, in this section, in order to better understand the flow structure around a single plume, velocity fields will be presented that were obtained by using the PIV technique during the solidification process for a larger imaged area.

The PIV images were processed with 50% overlap for enhanced spatial sampling and 21 × 21 pixel interrogation window and 31 × 31 pixel search window sizes. This resulted in a vector spacing of 0.259 mm. Overall, the vector field map covered an area of 29.3 mm x 21.3 mm. Usually, the flow medium must be seeded with particles, droplets, or bubbles. However, in this case, particles already existed as impurities in the ammonium chloride solution and were used for velocity measurements. The size of the

impurities or particles in the solution was less that 20 μm. Figure 8-12 shows the PIV image of a plume at t = 120 min and velocity vectors related to this image are shown in Figure 8-13.

Since the vector spacing is 0.259 mm and the diameter of the plume is about 1 mm, four vectors would fall in the plume area. A problem that one might encounter using the PIV technique to measure the plume velocity is the lack of particles in the plume as seen in Figure 8-12. As particles move into the mushy zone, they become nucleation sites and crystals form around them. As they grow, they attach to the mushy zone and cannot flow into the chimney, or into the plume from there. If there is a particle in the plume, it is due to the fact that entrainment takes place as the plume exits the mushy zone and particles are entrained from the surrounding into the plume. Usually, the number of particles in the plume is not high enough to get accurate velocity measurements. Therefore, a larger interrogation window size is needed to include more particles. This results in averaging the actual velocity of the plume.

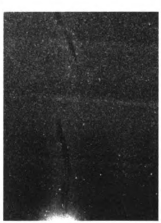

Figure 8-12: PIV image of a plume at t = 120 min (imaged area is 29.3 mm x 21.3 mm)

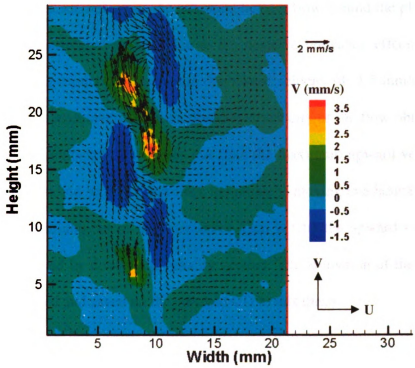

Figure 8-13: Measured velocity vectors of the plume at t = 120 min

It should be emphasized that the purpose of these measurements is not to obtain accurate velocity fields of the plume itself, but of the surrounding fluid.

Figure 8-13 shows the velocity vectors associated with the imaged area of Figure 8-12. The color bar represents the magnitude of the v-component of the velocity vector. The height axis is measured from the bottom of the imaged area, not from the bottom plate. It is clear from Figure 8-13 that as the plume moves upward in a helical motion (red areas), the fluid moves downward in an opposite helical motion wrapping itself around the plume. As described before, the downward flow is a result of both thermal and solutal buoyancy effects. In the case of thermal effect, the fluid in contact with the plume becomes cooler than the bulk fluid. The cooler fluid has a higher density than the bulk fluid, causing it to move downwards. In the case of solutal effect, as the plume ascends

into the density stratified surroundings, the entrained heavier flow around the plume (jet) encounters the lighter surroundings and, due to the negative buoyancy effect, it starts falling downwards. This results in a maximum downward velocity of -1.5 mm/s. This is in good agreement with measured maximum downward velocity of the flow obtained by Lum (2001) and is approximately four times less than the maximum upward velocity of the plume (6mm/s). It should be noted that since the plume is moving in a helical motion, it continuously moves in and out of the laser sheet. That is why the upward velocity is discontinued and replaced by downward velocity vectors. The animation of the velocity vectors has been obtained and saved on the attached CD to this thesis.

8.4 Velocity measurement above a row of nucleators using Particle Image Velocimetry (PIV) technique

In order to understand some of the flow features between two phase locked plumes, a similar experiment to that in the previous chapter (Figure 7-9) was carried out to obtain whole field velocity vectors above the mushy zone and on a row of nucleators using the PIV technique. The imaged area (8.5 × 6.2 cm^2) is 3 cm above the bottom plate, and it is directly above the mushy zone. A 15 ×15 pixel interrogation window and a 21 × 21 pixel search window were used to obtain these velocity vectors. This resulted in a vector spacing of 0.44 mm. Not all of the plumes formed within the laser sheet. Only five of them seemed to form on the imaged plane. Figure 7-14 shows the PIV image of the solution.

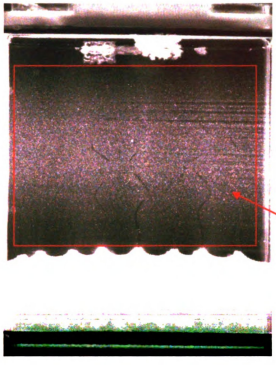

Figure 8-14: PIV image of the solution at t = 120 min

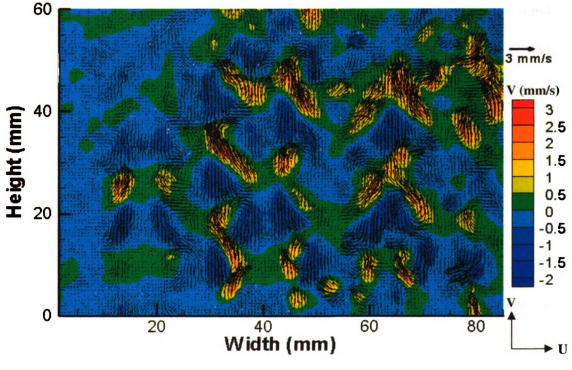

Figure 8-15: Measured velocity vectors of the flow above a row of nucleators

It is clear from the PIV image that there is a lack of particles in the plumes; therefore, accurate velocity measurements can be obtained only in the surrounding fluid, not in the plumes. As can be seen in Figure 8-15, when two adjacent phase locked plumes diverge as they move upward in a helical motion, the velocity of the flow between them is downward with a negative sign (blue color). As the plumes get closer, the velocity of the flow starts to increase and, eventually, the velocity at the regions of closest approach between the two plumes is upward (green color).

8.5 Velocity fields above an area free of plumes

It was shown by using the LIF technique in section 8.2 that after t = 60 min the temperature of the flow above the mushy zone and above an area free of chimneys is almost uniform laterally. This is expected to result in a more uniform composition profile of the final product of the solidification process. In order to have a better understanding of the velocity fields above this area, an experiment similar to that discussed in section 8.2 was carried out to measure the velocity vectors in an area where plumes do not form (Figure 8-16). The bottom left corner of the image is at (27.75mm, 30mm, 4mm). The images were processed with a 50% overlap for enhanced spatial resolution, and 11 x 11 pixel interrogation window and 17 x 17 pixel search window sizes. This resulted in a vector spacing of 0.41 mm. Overall, the vector field map covered an area of 52 mm x 38 mm. Since no plume exists on the image plane, accurate velocity values can be obtained using the PIV technique. Velocity vectors measured at different times are shown in Figure 8-17. The height is measured from the bottom of the imaged area, not from the

bottom of the plate, and the color bar shows the magnitude of the v-component of the velocity vectors.

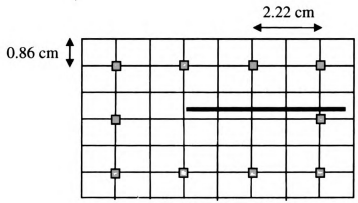

Figure 8-16: Arrangement of the nucleators and location of the laser sheet

Figure 8-17: PIV image of the imaged area above an area free of plumes

Right before crystallization begins (t = 4min), there is an evidence of large scale flow circulation in the container as shown in Figure 8-18(a) due to the thermal buoyancy effect. Once the fingers are formed, the upward velocity vectors next to the downward flow can be observed as seen in Figure 8-18(b). The maximum velocity of these fingers is about 1.5 mm/s. As time goes by, the number of fingers increases, but their maximum velocities remains constant. At t = 20 min, the maximum velocity of the fingers starts to decrease and the fingers become weaker. This is due to the fact that the plumes are forming on the arranged nucleators and more flow has to penetrate into the mushy zone to feed the plumes through the chimneys within the mushy zone. Later in time, fingers decrease in number as they get weaker (Figure 8-18 (g)) and some disappear. At t = 60 min, no fingers can be observed on the imaged plane. The upward velocity vectors seen at this time are very small (compared with that of the fingers, 1.5 mm/s). A small maximum positive V-velocity component of 0.06 mm/s exists because solidification is still taking place at the mush-melt interface; therefore, some water-rich fluid ascends locally at the interface. Velocity vectors seen at this time are small in magnitude.

The flow structure at t = 90 min is similar to that of t = 60 min, and the height of the mushy zone has increased. The fact that flow is calm and temperature is uniform laterally above this area suggests that the solidification process is uniform above this area, and better quality of the final product can be obtained. As was mentioned before, velocity profile of the plume cannot be obtained accurately by using PIV measurements due to the lack of particles inside the plume. Molecular Tagging Velocimetry has the potential to give additional insight by providing valuable data that quantifies the velocity field within and around phase locked

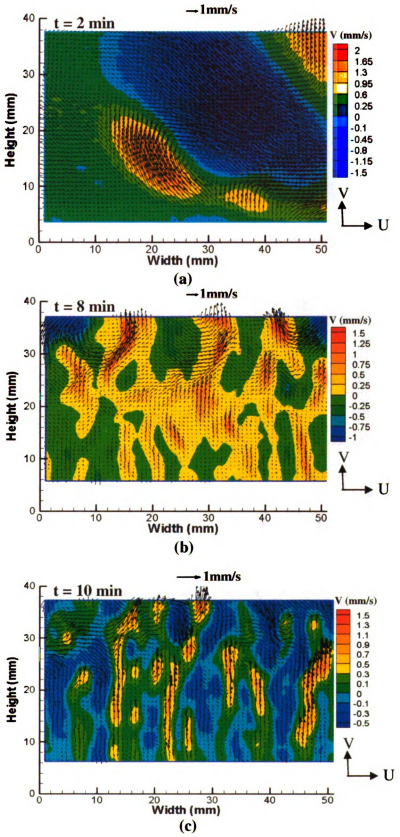

Figure 8-18: Velocity vectors at different times above and area free of plumes

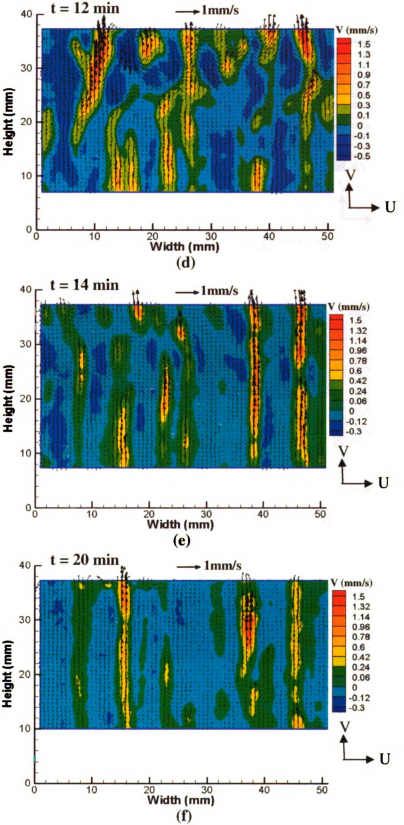

Figure 8-18: Velocity vectors at different times above and area free of plumes

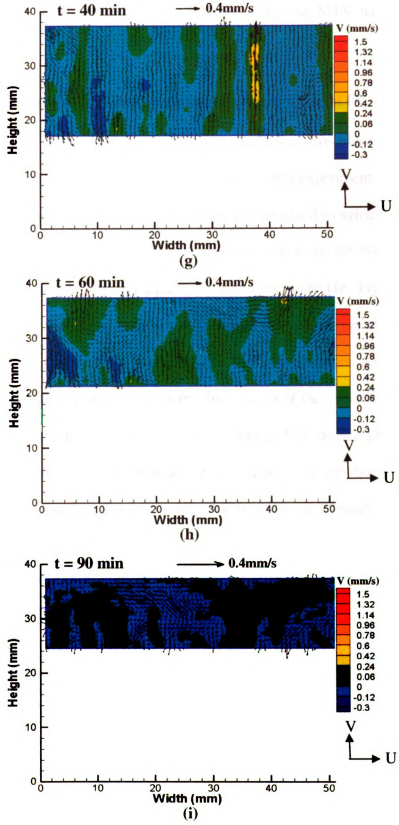

Figure 8-18: Velocity vectors at different times above and area free of plumes

plumes. In the following section, the results from using the MTV technique will be described.

8.6 Velocity measurement of two phase locked plumes using MTV technique

It was shown before that the temperature profiles of two phase locked plumes with 180° phase difference were the same. The aim of this experiment was to find out whether or not the two phase-locked plumes were also identical in velocity profile. Two big nucleators were placed in the middle of the test section on the bottom plate with spacing of 1.2 cm. The UV laser had a pulse repetition rate of 10 Hz. Figure 8-19 shows the delayed image of the tagged lines at t = 25 min in the test section above the mushy zone. This image is obtained from averaging five successive images. As can be seen in this figure, the maximum displacement of the lines occurs at the locations where plumes exist. At this time the plumes were phase locked with a 180° degree phase difference. Velocity profiles of the plumes 5.3mm above the mushy zone are shown Figure 8-20. Both plumes have almost the same maximum velocity values of 3.5mm/s.

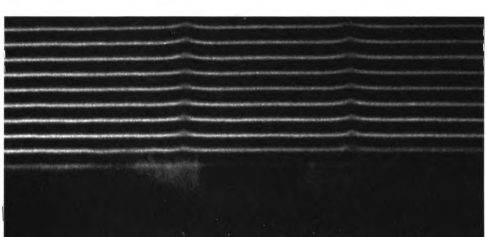

Figure 8-19: Line tagging above the mushy zone at t = 25 min for the case of two phase locked plumes above two big nucleators with a spacing of 1.2 cm

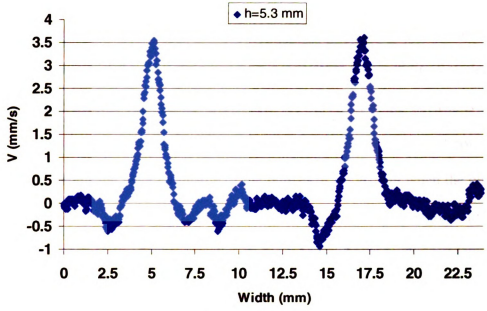

Figure 8-20: Velocity profiles of the plumes at t = 25min for the case of two phase locked plumes above two big nucleators with a spacing of 1.2cm

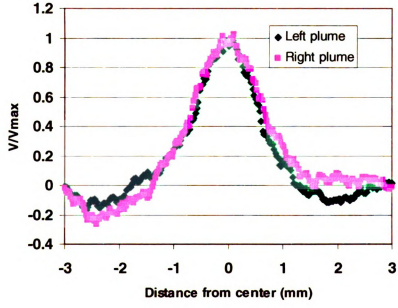

Figure 8-21: Overlapped velocity profiles of the plumes for the case of two big nucleator pair

A similar experiment was carried out by using the big-small nucleator pair in the middle of the test section. The spacing between nucleators was 1.2 cm. An initial observation revealed that most of the time the two plumes generated above the two nucleators were phased locked with a 180° phase difference. However, in some occasions during the experiment, they fell out of phase (is not clear why) with no relation between phases. Figure 8-22 shows the velocity profile of the plumes at t = 40 min when the plumes were phase locked with 180° phase difference. Again, delayed and undelayed images were obtained from averaging five successive images. As can be seen, the maximum velocity values of the plumes are almost identical. The velocity profile on the left belongs to the plume formed above the small nucleator and the one on the right belongs to that formed above the big nucleator.

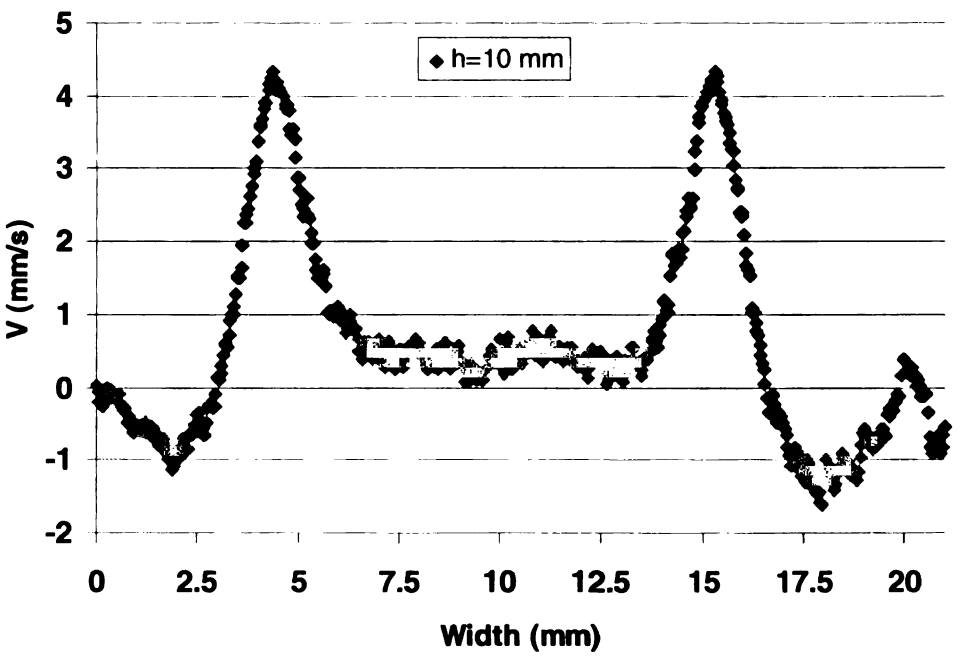

Figure 8-22: Velocity profiles of the plumes at t = 40min for the case of big-small pair

At t = 60 min suddenly the two plumes fell out of phase. Figure 8-23 shows the velocity profiles of these plumes at this time. The maximum velocity values changed slightly. The velocity of the plume above the small nucleator slightly decreased; whereas, the one above the big nucleator slightly increased.

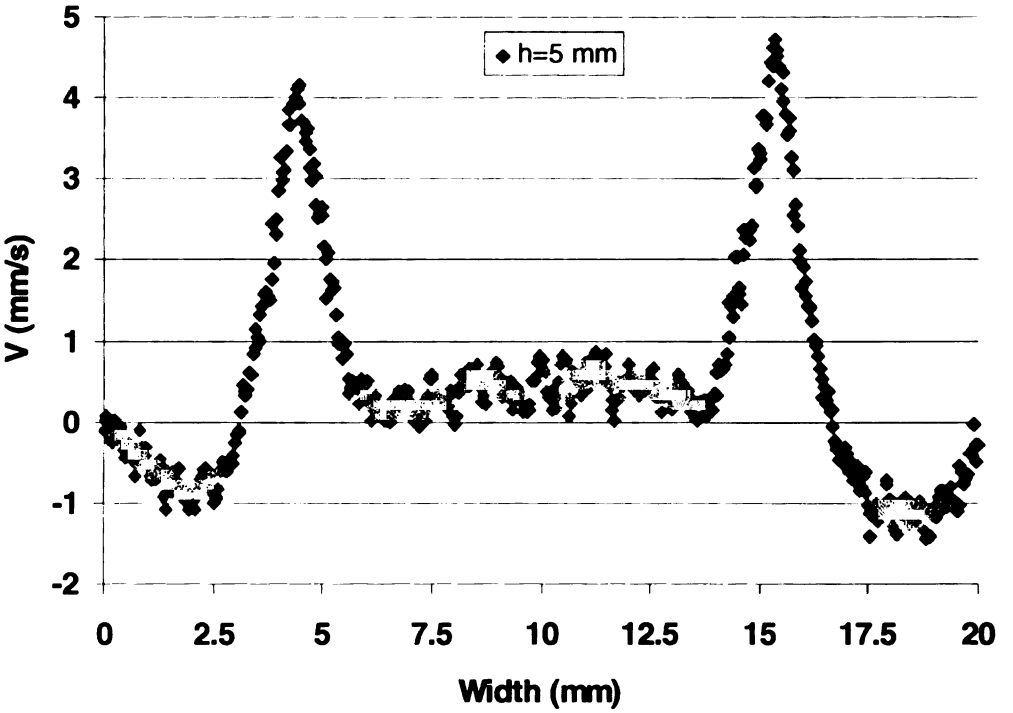

Figure 8-23: Velocity profiles of the plumes at t = 60min for the case of big-small pair

It seems that this small variation in velocity difference (0.5mm/s) was enough to force the two plumes out of phase. These results show that when the two plumes are phase locked with 180° phase difference their velocity profiles are very similar.

A Molecular Tagging Velocimetry and Thermometry (MTVT) technique has been developed recently at the TMUAL (Turbulent Mixing and Unsteady Aerodynamics Laboratory) at Michigan State University by Hu and Koochesfahani (2002). This technique is capable of measuring velocity and temperature of the flow simultaneously.

Unfortunately, because the sensitivity of the life time to temperature variation was small, and also because the lifetime of the chemical depends on the concentration of ammonium chloride, the MTV&T technique could not be used to obtain simultaneous temperature and velocity measurements of the plumes. This optical diagnostic technique and its reasons for not being applicable to this study are detailed in the Appendix D.

Chapter 9

Conclusions

In the solidification process of a simple binary alloy, solutal and thermal buoyancy forces play an important role in the creation of plumes and imperfections (freckles) in the final product. Therefore, it is important to know the temperature distribution in the liquid regions during the solidification of aqueous ammonium chloride. Whole-field temperature maps have not been obtained in the past for the liquid region in a conventional size container during solidification process. The temperature map obtained by Solomon and Hartley (1997) using thermochromic liquid crystal paints (TLC) was in a Hele-Shaw cell. The flow field velocities in Hele-Shaw cells are different from those in conventional size containers due to the viscous effect imposed by walls on the flow. Since liquid crystals were painted on the wall surface, the temperature map obtained was not the actual temperature map of the fluid itself but of the wall boundaries.

To address the lack of appropriate experimental data in this field, a two-color LIF technique was developed and used to measure temperature distribution during the solidification process of aqueous ammonium chloride. As the plume rises vertically in helical motion, the curved edge of the plume causes the laser sheet to diverge and results in dark streak patterns in certain areas of the image. It was shown that the two-color LIF technique can suppress the effect of these streaks on the measured temperature values. Two color bands should usually be chosen such that one is temperature sensitive and the other is temperature insensitive (Sakakibara and Adrian 1999). The fluorescence signal of temperature sensitive dye provides the temperature distribution in the measurement region and that of the temperature insensitive dye provides the intensity distribution of

the incident illumination laser light. For the first time in two-color LIF technique, temperature resolution has been improved and doubled by using two temperature sensitive dyes with opposite sensitivity to temperature variation. The two dyes used were fluorescein and kiton red. The calibration curve showed that if exited at 514nm, the intensity of fluorescein decreases with decreasing temperature and that of kiton red increases.

The initial measurements of the solidification process yielded some interesting results. The temperature distribution in the plume region was clearly captured and the temperature profile indicated a minimum temperature value at the center of the plume. The temperature of the center of the plume and that of the surrounding fluid monotonically increased as the plume was moving upward away from the mushy zone and merging eventually at the top section of the container. The maximum temperature difference between plume and the surrounding fluid was found to be 2.7^{o} C.

The energy equation was simplified based on some assumptions and solved numerically. It was shown that the simplified energy equation could be used to obtain the temperature profiles across a plume for a short portion of the plume close to the mushy zone when appropriate boundary conditions were given (found experimentally). The temperature profiles obtained from the numerical study agreed well with the measurements. Most of the proposed numerical models for solidification processes of ammonium chloride use equilibrium phase diagram to find temperature and concentration values of the solution within the mushy zone, assuming that the flow is in equilibrium state. However, whole-field temperature measurement showed that within 4 minutes of applying coolant to the bottom heat exchanger, when no crystals are formed, the

temperature of the solution (7° C) close to the bottom plate corresponding to 26% wt concentration of ammonium chloride was well below the liquidus line (18.6° C). Therefore, the liquid close to the bottom plate was subcooled and not in equilibrium. The fact that the fluid is subcooled near the bottom cooling plate needs to be taken into account in numerical modeling. Whole-field temperature measurement also clearly showed the temperature characteristic of the fingers for the first time. Due to the existence of the fingers above the mushy zone, the temperature distribution was non-uniform, which was in good qualitative agreement with numerical results obtained by Neilson and Incropera (1993). The evolution of fingers into the plumes could be seen from the whole field temperature maps. As salt-rich fluid adjacent to the plume is cooled, it descends as a sheath along the plume. These sheaths cannot traverse the plume bends, causing them to separate from the plume and descend freely. The sheaths are called wisps. The temperature of the wisps was captured by using the LIF technique and the results showed that these wisps could be approximately 0.5° C warmer than the center of the plume itself.

It was shown experimentally that the location of the plumes and chimneys can be controlled during the solidification process of ammonium chloride by placing metallic nucleators on the bottom cooling plate. Plumes could be formed above the nucleators because, at initial stages of the solidification process, stronger fingers were formed above the nucleators. This was due to the fact that these nucleators acted as thermal fins and they enhanced the solidification rate locally. This enhanced heat transfer from the surrounding fluid to the bottom plate would trigger one of the instability modes at the locations of the nucleators. It was not clear if this instability mode was in the form of the

'mushy-layer' mode or 'boundary layer' mode as identified by Worster (1992) mathematically.

To examine the effects of size and arrangements of nucleators on the solidification process of ammonium chloride, two different arrangements and sizes (big and small nucleators) were used. The experiments clearly showed that with a bigger nucleator, more perturbation at the location of the nucleator was induced and therefore, a plume was more probable to form at that location. When the distance between two nucleators was less than 0.5 cm for big nucleators and 0.6 cm for small nucleators, only one plume formed above them. If the distance between nucleators was less than 1.2 cm, the two plumes were always phase locked with 180^{o} phase difference. The phase locking was due to the hydrodynamic coupling between nearby jets. Entrainment of fluid and counter-propagating shear flow produce dynamical instabilities, and result in synchronization of phases of the nearby plumes. It was also demonstrated that it is possible to obtain a relatively large area free of chimneys by placing nucleators around the side walls but not very close to the walls. It is not clear yet why more plumes were formed randomly elsewhere when nucleators were placed very close to the side walls. The size of an area free of chimneys that can be obtained depends on the pumping effect of the plumes (caused by buoyancy difference between the plumes and the surrounding fluid) and the permeability of the mushy zone. With a larger concentration difference between the plumes and the surrounding fluid (more pumping effect), and more permeability of the mush, a larger area free of chimneys can be obtained by placing nucleators around the periphery of that area. This experiment has demonstrated a novel, cheap, and easy technique to enhance the quality of unidirectionally solidified binary

alloys and obtain a more uniform composition profile of the final product of the solidification process by pushing the chimneys out to the sidewalls and leaving a large area in the center free of defects.

To have a better understanding of flow structure around the plume, particle image velocimetry (PIV) technique was used to measure the velocity vectors in the solution during the solidification process. The problem that one might encounter using the PIV technique to measure the plume velocity is the lack of particles in the plume. As particles move into the mushy zone, they become nucleation sites and crystals form around them. As they grow, they attach to the mushy zone and cannot flow into the chimney and from there into the plume. Thus, the plumes are left out without particles in them and PIV measurements can not be carried out inside the plumes. Our PIV measurements around the plumes in the surrounding fluid showed that as the plume moved upward in helical motion, another flow adjacent to it moved downwards with slower speed (3 to 4 times slower than the maximum velocity of the plume) in helical motion and both flows were twisted around each other.

The PIV measurements also showed that the maximum velocity of the fingers was 1.5 mm/s at initial stages of the solidification process located above a relatively large area free of plumes (in good agreement with results obtained by Lum, 2001). After t = 60min the upward velocity of the flow was very small 0.06 mm/s (no finger was observed). The whole field temperature maps also showed that in this region, where no plume existed after t = 60min, the temperature was well stratified. The fact that the flow was calm and the temperature was uniform laterally above this area suggested that the solidification

process was taking place uniformly at mush-melt interface, resulting in a better quality of the final product.

To compare the velocity profiles of two adjacent phase locked plumes, molecular tagging velocimetry (MTV) technique was used to obtain one dimensional velocity profiles of the plumes. The PIV technique could not be implemented to measure the velocity of the plumes due to the lack of particles in the plume. The results showed that the velocity of the two phase locked plumes with 180^{O} phase difference is identical (the overlapping between two velocity profiles was good.). The LIF technique also showed that their temperature profiles were identical. When the two plumes were out of phase, the velocity profiles looked slightly different. In one example the difference between maximum velocities of two plumes was about 0.5mm/s. That small variation in velocity difference was enough to force the two plumes out of phase.

It is believed that the nucleators can be used in other solidification processes to enforce the freckle formation at desired locations. However, experiments need to be conducted to confirm this hypothesis.

Chapter 10

References

Adrian Bejan 1995. "*Convection Heat Transfer*". John Wiley & Sons, Inc.

Bergman, T.L., and Ungan, A., 1988, "A note on lateral heating in a double-diffusive system", *J. Fluid Mech*, Vol. 194, PP. 175-186.

Chee Leong Lum, 2001, "Velocity field measurement for a uni-directional solidification of an ammonium chloride (NH4Cl) solution using Molecular Tagging Velocimetry (MTV)", *master thesis*, conducted at Mechanical Engineering Department, Michigan State University.

Chen, C.F., and Chen, F., 1991, "Experimental Study of directional Solidification of Aqueous Ammonium Chloride Solutions", *J. Fluid Mech*, Vol. 227, PP. 567-586.

Chen, Y. M., and Liou, J. K. (1997). "Time-dependent double-diffusive convection due to salt-stratified fluid layer with differential heating in an inclined cavity" *Int. J. Heat Mass Transfer* 40, 711-725.

Chen, F., Lu, J.W., and Yang, T.L., 1994, "Convection Instability in Ammonium Chloride Solution Directionally Solidified from Below", *J. Fluid Mech*, Vol. 276, PP. 163-187.

Dombrowski, C., Lewellyn, B., Pesci A. I., Restrepo, J. M., Kessler, J. O., and Goldstein, R. E., (2004). "Coiling, Entrainment, and Hydrodynamic Coupling of Decelerated Fluid Jets" *Int. J. Heat Mass Transfer* 33, 367-380.

Falin Chen, (1997). "Formation of double-diffusive layers in the directional solidification of binary solutions" *Journal of Crystal Growth* 179, 277-286.

Garimella, S.V., McNulty, J.P., and Schlitz, L.Z., 1995, "Formation and Suppression of Channels during Upward Solidification of a Binary Mixture", *Metallurgical and Materials Transactions A*, Vol. 26A, PP. 971-981.

Gendrich, C. P. and Koochesfahani, M. M., 1996, "A spatial correlation technique for estimating velocity fields using Molecular Tagging Velocimetry (MTV)," *Exp. in Fluids*, 22(1), 67-77.

Hellawell, A., Sarazin, J. R., and Steube, R. S., 1993."Channel convection in partly solidified systems" *Phil. Trans. R. Soc. Lond.* A345, 507-544.

Hu, H., Koochesfahani, M.M., 2002, "A novel Technique for quantitative temperature mapping in liquid by measuring lifetime of laser induced phosphorescence", *The 10th International Symposium on Flow Visualization*, August 26-29, Kyoto, Japan. .

Kay Wirtz, 1998, "Experimental study of convection phenomena associated with solidification processes", *master thesis*, RWTH-Aachen, conducted at Mechanical Engineering Department, Michigan State University.

Kim, H.J. and Kihm, K.D., 2001, "Application of a Two-Color Laser Induced Fluorescence (LIF) Technique for Temperature Mapping", *Proceedings of ASME IMECE*, November 11-16 - New York, USA.

Koochesfahani, M. M., 1999, "Molecular Tagging Velocimetry (MTV): Progress and Applications", AIAA Paper No. AiAA-99-3786 (invited).

Kou, S., Poirier, D. R., and Flemings, M. C., 1978, "Macrosegregation in rotated remelted ingots". *Metall. Trans.*, B 10B, 331-339.

Kranenborg, E. J., and Dijkstra, H. A. 1998, "On the evolution of double-diffusive intrusions into a stably stratified liquid: a study of the layer merging process" *Int. J. Heat Mass Transfer* 41, 2743-2756.

Lum, C.L., Koochesfahani, M.M., and McGrath, J.J., 2001, "Measurements Of The Velocity Field With MTV During The Solidification Of An Alloy Anolog With Mushy Region", *Proceedings of ASME IMECE*, Vol. 31, PP. 1-7.

Magirl, C.C., and Incropera F.P., 1993, "Flow and Morphological Conditions Associated With Unidirectional Solidification of Aqueous Ammonium Chloride", *Transactions of the ASME*, Vol. 115, PP. 1036-1043.

Neilson, D. G., and Incropera, F. P. 1993, "Effect of rotation on fluid motion and channel formation during unidirectional solidification of binary alloy" *Int. J. Heat Mass Transfer* 36, 489-505.

Neilson, D. G., and Incropera, F. P.,1990, "Numerical simulation of solidification in a horizontal cylindrical annulus charged with an aqueous salt solution" *Int. J. Heat Mass Transfer* 33, 367-380.

Pera, L., and Gebhart, B., 1971, "On the stability of laminar plumes: some numerical solutions and experiments" *Int. J. Heat Mass Transfer* 14, 975-984.

Popvich, A. T., Hummel, R.L. 1967, "A New Method for Non-Disturbing Turbulent Flow Measurement Very Close to Wall" Chem. Eng. Soc, Vol. 22, 21-25.

Pringsheim P. 1949, "*Fluoresence and Phosphorescence*", Interscience publishers, INC. New York.

Sakakibara, J. and Adrian, R. J.1999, "Whole field measurement of temperature in water using two-color laser induced fluorescence", *Experiments in Fluids*, 26, 7-15.

Sample, A. K., and Hellawell, A.,1982, "The effect of mold precession on channel and macro-segregation in ammonium chloride-water analog castings", *Metall. Trans.*, B 13B, 495-501.

Sample, A. K., and Hellawell, A. 1984, "The mechanisms of formation and prevention of channel segregation during alloy solidification", *Metall. Trans.*, A 13A, 2163-2173.

Shafii, M. and Koochesfahani, M. M. 2003, "Temperature Measurement of Aqueous Ammonium Chloride Solution during Solidification Process Using Laser Induced Fluorescence (LIF)", *Bull. Am. Phys. Soc.*, 48(10), 180.

Tanny, Y., and Yakubov, B., (1999), "Experimental study of a double-diffusive two-layer system in a laterally heated enclosure", *Int. J. Heat Mass Transfer* 42, 3619-3629.

Worster, M.G., 1992, "Instabilities of the liquid and mushy regions during directional solidification of alloys", *J. Fluid Mech*, Vol. 237, PP. 649-669.

Appendix A

Some Experimental Reports on Double-Diffusive Layer

The nature of double-diffusive natural convection, seen in the solidification process of ammonium chloride, will be explained in this section. The formation of double diffusive layers (DDL) is a result of the interaction between the vertical concentration gradient and the horizontal temperature gradient. When a parcel of liquid near a heated wall moves upward, it retains almost all of its salt due to the very small salt diffusivity. The parcel rises to a level where its density is equal to that of the surrounding liquid, and because of the buoyancy effect, it is then forced to move laterally, and a layered flow pattern eventually results. These flow patterns create double diffusive cells.

Bergman and Ungan (1988) performed experiments of double-diffusive convection in a two-layer, salt-stratified solution (Figure A-1, $C_1 > C_2$) destabilized by lateral heating and cooling of side walls. Two fluid layers with two different concentrations were contained within an enclosure and the sidewall temperature were kept at T_1 and T_2 ($T_1>T_2$). Polystyrene-encapsulated liquid crystals were mixed with solutions to visualize temperature changes in the layers. The interface was the location of significant upward heat transfer and thermally unstable density distributions, resulting from cool fluid traveling from the cold wall to the warm wall above the interface. Bergman and Ungan (1988) mentioned that the salinity interface was not horizontal. Figure A-1 below shows a schematic of their experimental observation. The salt transport continuously occurred from the salty bottom layer to the water-rich top layer. After some

time, the vertical boundary layers on the heated and cooled sidewalls began to penetrate the salinity interface as seen in Figure A-2.

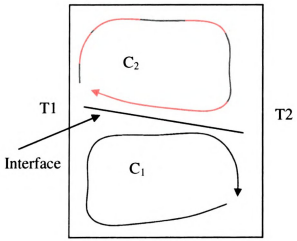

Figure A-1: Two-layer salt-stratified solution (C_1 and C_2) destabilized by lateral heating and cooling

At this time the interface was tilted and secondary flow at the interface became very evident. Eventually, both fluids got mixed and no double-diffusion effect was observed.

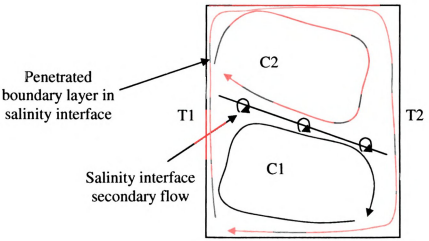

Figure A-2: Double diffusive layers and secondary flow at the interface

This mixing time (complete mixing) was characterized by three parameters: Rayleigh number, Solutal to Thermal buoyancy forces, and Fourier numbers. Fourier number is a time scale associated with mixing.

$$Ra_T = \frac{g\beta_T (T_1 - T_2)}{\nu\alpha} L^3 \qquad \text{(A-1)}$$

$$R_\rho = \frac{\beta_C (C_2 - C_1)}{\beta_T (T_1 - T_2)} \qquad \text{(A-2)}$$

$$Fo = \frac{Dt_m}{L^2} \qquad \text{(A-3)}$$

In these expressions, C_2-C_1 is the difference in the layer solute concentration, α is the thermal diffusivity, ν is the kinematic viscosity , β_C and β_T are solutal and thermal expansion coefficients of the solution, L is the width of the container and D is species diffusivities. The dimensionless mixing time decreases as Ra_T increases. This seems to be obvious since a more salt is transferred through the interface due to an increase of ΔT and natural convictive velocities. The dimensionless mixing time increases as R_ρ increases due to more stable interface.

Kranenborg and Dijkstra (1998) performed a direct numerical simulation. They assumed liquids initially stratified through a constant salt gradient. Their numerical results showed that as time proceeded, convection cells formed near the heated left wall and gradually filled up the cavity forming double-diffusive cells. Their results showed that as R_ρ decreased, the number of convection cells decreased and as a result the

convective transport of salt became stronger. It was also shown that the concentration within each convective cell was uniform.

An experimental study was carried out by Tanny and Yakubov (1999) to investigate the mixing process of a two-layer stratified fluid in a laterally heated enclosure. They concluded that the appearance of vortices at the interface separating the layers was an instability phenomenon. The critical Rayleigh number for the onset of interfacial instabilities shown in Figure A-2 was proposed as

$$Ra_c = 10^{8.2} \times R_\rho{}^{1.28} \qquad \text{(A-4)}$$

Chen and Liou (1995) performed a numerical study on time-dependent double-diffusive convection of NaCl-H_2O concerning the stably stratified salt fluid layer with lateral heating in an inclined cavity. Their results showed that at early time, the convective cells are generated near the bottom and top walls, and then, some simultaneous cells appear in the middle portion at the hot wall and intrude toward the interior region. The onset of instability was more pronounced at the negative angles (hot wall on top) than the positive ones (hot wall at the bottom). When the angle increased, the effect of heating-from-below was more and more vigorous. The fluid parcel near the hot wall raised up more and more along the sidewall, making the bottom cell larger in size and reducing the cell numbers in the cavity. The convective flow would occupy the whole domain at positive angles, but only part of the domain at negative angles. Their

results showed that the average Nusselt number was higher for positive angles than for negative angels.

The double diffusive layers formed in this study during the solidification process of ammonium chloride were a result of the concentration gradient along the test section and the temperature difference between the plumes and the surrounding fluid. It was shown in previous chapters that the double-diffusive layers usually formed around the plumes and the side walls, where lateral temperature gradients existed.

Falin Chen (1997) carried out some experiments on the solidification process of ammonium chloride. From his observations, several features were delineated as summarized below. DDLs (double diffusive layer) were observed in the upper half of the bulk fluid. As a new layer was formed on top, the layer interface moved downward continuously until it reached the melt/mush interface and broke down. The flow pattern of the plume was not changed by the presence of the DDLs. The onset of the formation of DDLs occurred a couple of minutes after the salt fingers vanished (50 min, bottom plate temperature T_b= -9.8° C, H = 10cm, top plate temperature T_t = 29.6° C, initial concentration 28% wt). There were 7 layers in the system with an average thickness of 0.7 cm each (almost constant during the experiment). The averaged propagating speed was about 0.075 cm/min initially and decreased with time (minimum of 0.043 cm/s). As a general rule, they found out that the onset of DDL occurred when the number of plumes reached the maximum. Due to the break down of the DDLs at the mush/melt interface, the overall thickness of the mush decreased about 0.15 cm. The reason for remelting is that the concentration of DDLs formed on the top region remained unchanged during their propagation downwards because of the small diffusivity across the layer interfaces.

The less-concentrated fluid of the DDL interacted with the mush/melt interface and remelted it. After plumes formed, the concentration of ammonium chloride was less at the top of the test section and uniform in the center. This resulted in a negative concentration gradient on the top region of the test section. The lower concentration gradient was due to the fact that the plumes brought less-concentrated fluid into the upper region. The DDL thickness (0.6-1cm) did not change with constant bottom plate temperature. However, the time evolution of the plumes was influenced by the bottom plate temperature, T_b. The DDL appeared when the concentration gradient was negative everywhere in the test section. If plumes broke up before they reached the top region, it caused a positive gradient on the top region and from the consequence of that, no DDL formed. It should be noted that the experimental set up of Chen was slightly different from that of used in this study since the top boundary of his was fixed at 30^{o} C and that of in this study is open to ambient.

Appendix B

Synchronization of Two Cameras

To capture two simultaneous images from the two Pulnix cameras (8-bit, 30 frames/s), the outputs of the two cameras are connected to the red and green channels of an RGB frame grabber (Mutech MV-1300) and then digitized (8 bits) as a color image and saved on a disk. The green and red intensities of this color image are subsequently separated using a MATLAB code to restore the two images captured by the two cameras. To acquire a color image, two cameras have to be synchronized by means of an external SYNC generator (standard RS-170). The framing rates of these cameras are fixed at 30 frames/second. Figure B-1 shows the schematic for synchronizing two cameras.

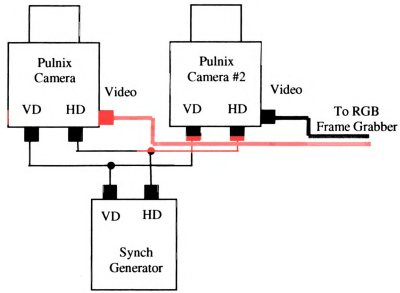

Figure B-1: Schematic for synchronizing two Pulnix cameras

In order to capture two simultaneous images from two PixelFly (12-bit) cameras, the cameras are connected to two separate PCI boards on two separate computers. Each camera can be controlled on each computer separately by related software (CamWare). To synchronize the two cameras, the provided SYNC cables are first connected to each separate PCI board. The other ends of the cables, which are BNC type, are connected to a signal generator that generates TTL signals (5 Volts). Then, the trigger of each camera is set to external mode (Extern) through the software (CamWare). When the record buttons are selected on the software, the cameras are ready to take images. For every TTL signal, each camera takes one image. A burst of signals can also be given, but one should make sure that the time delay between each TTL signal is longer than 80ms + exposure time. Figure B-2 shows the schematic for synchronizing the two PixelFly cameras.

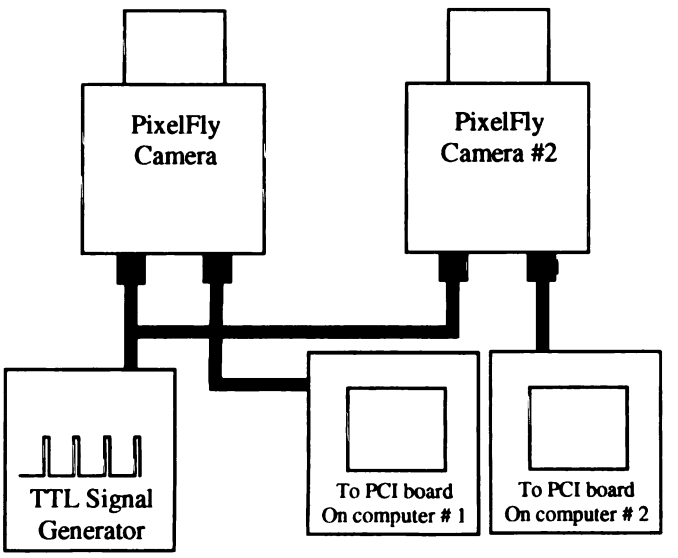

Figure B-2: Schematic for synchronizing two PixelFly cameras

Appendix C

On the Stability of Laminar Plumes

As mentioned before, plumes move upward in helical motion during the solidification process of ammonium chloride solution. The helical motion of these plumes, which has a resemblance to the stability of buoyant jet flows, is due to the hydrodynamic instability.

An investigation of the hydrodynamic stability of a laminar plume arising from a horizontal line source of heat was carried out by Pera and Gebhart (1970). Inviscid solutions of the Orr-Sommerfeld equation were obtained for both symmetric and asymmetric disturbances. They assumed a steady locally periodic flow (the amplitude of disturbances does not vary with time, but with x). The computed neutral stability curve (α) for coupled governing equations and asymmetric disturbances was presented in terms of modified Grashof number (G) and Prandtl number (Pr).

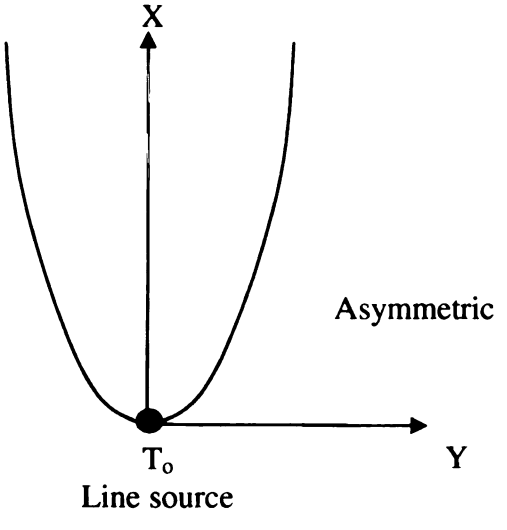

Figure C-1: Schematic of laminar plume rising from a horizontal line source

The modified Grashof number G was defined as

$$G = 2\sqrt{2}(Gr)^{0.25} = 2\sqrt{2}\left(\frac{g\beta x^3(T_o - T_\infty)}{\nu^2}\right)^{0.25} \qquad \text{(C-1)}$$

where g is gravity, β is coefficient of volumetric expansion, T_o is the temperature of the base flow (source), T_∞ is surrounding temperature, and ν is kinematic viscosity of the fluid. It was shown that

$$\frac{\lambda}{x} = \frac{8\pi}{\alpha G} \qquad \text{(C-2)}$$

where x is distance from the source in the vertical direction and α and G parameters were obtained from the computed neutral curve. Since the energy and species equations are very similar, one can use the same theory to calculate the wavelength of the oscillation of a plume as a function of height (x). For this scenario, ΔT and thermal expansion β in Equation (C-1) has to be replaced by ΔC and solutal expansion coefficent. Schmidt number (analogous to the Prandtl number in heat transfer) also needs to be used. The physical properties of the plume are summarized in Table C-1

Table C-1: Properties of the Plume

ΔC (%wt)	**solutal expansion β ($\%wt^{-1}$)**	**ν (m^2/s)**	**Schmidt number**
2%	0.003	10^{-6}	800

Assuming the location of the point source to be at the exit of the plume on the mush-melt interface, one can use Equation (C-2) and the plotted curve by Pera and Gebhart (1970) to calculate the wavelengths of the disturbances as a function of height (Figure C-2). This is a valid assumption since the Reynolds number is very small at the exit of the mush-melt interface (Re=4)

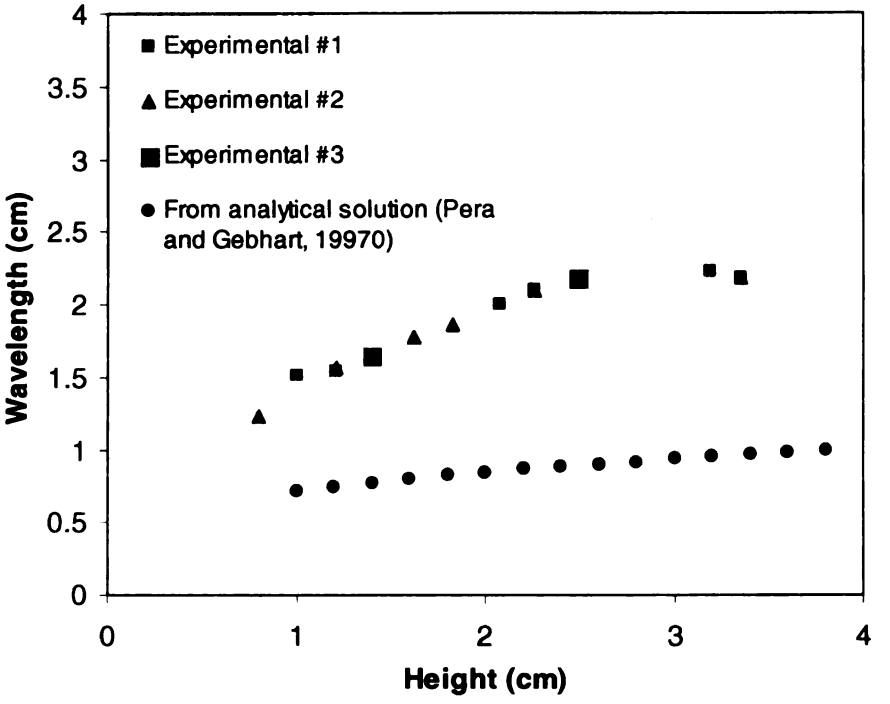

Figure C-2: Wavelength as a function of height along the plume

As can be seen in Figure C-2, the calculated wavelengths of the plumes based on Pera and Gebhart (1970) predictions are almost twice as small as those measured experimentally (Figure C-3). This mismatch is due to the fact that the plume is bounded

on the top surface of the container, which influences the motion of the plume. The shearing force between the plume and the descending fluid also makes the plume more unstable.

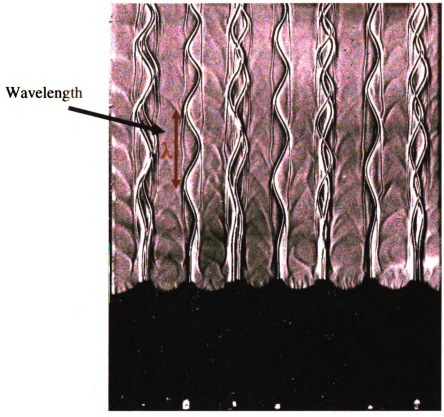

Figure C-3: Wavelength of a plume measured from peak to peak

Appendix D

Molecular Tagging Velocimetry and Thermometry (MTV&T)

Molecular Tagging Velocimetry and Thermometry (MTV&T) has been developed at Michigan State University by Hu and Koochesfahani (2002). As mentioned in the body of this work, when a substance is exposed to incident photons, a fraction of the molecules in the appropriate lower energy level absorbs the incident light and are excited to a higher energy state. These molecules return to the equilibrium ground state by emitting photons. Compared with fluorescence, which typically has a lifetime in the order of nanoseconds, phosphorescence has a much longer lifetime in the order of microseconds to minutes. As described in this work, the emitted phosphorescent can be used in the MTV technique to measure the velocity vectors in the flow field. The lifetime of the phosphorescent dye used in MTV technique (1-BrNp-Gβ-CD-ROH) is also temperature dependent. As in the MTV measurements, the phosphorescence signal is imaged at two successive times within the lifetime of the tracer. The phosphorescence lifetime, estimated from the intensity ratio of the two images at each point, is calibrated against the temperature. While the displacements of the tagged regions between two interrogations provide the estimate of flow velocity vectors, the intensity ratio of the two images represents the fluid temperature distribution. Therefore, simultaneous velocity fields and temperature maps can be obtained.

Phosphorescence life time

According to quantum theory, the decrease of emission intensity follows an exponential law (Pringsheim 1949). Therefore, the intensity decay of a photoluminescence process (fluorescence or phosphorescence) can be expressed as

$$I_{em} = I_o e^{\frac{-t}{\tau}} \qquad \text{(D-1)}$$

Where lifetime (τ) refers to the time when the intensity drops to 37% (1/e) of the initial intensity. Therefore, the ratio intensity at two different times, t_1 and t_2 will be

$$\frac{I_{em2}}{I_{em1}} = e^{\frac{-(t_2 - t_1)}{\tau}} \qquad \text{(D-2)}$$

From Equation (D-2), it is clear that the intensity ratio of the two successive phosphorescence images is only a function of phosphorescence lifetime, not the initial intensity I_o (or laser power). It should be noted that the Equation (D-2) is valid when the exposure times for two successive phosphorescence images are the same. If the exposure times are different, this equation will change slightly and the expression for it can be found in Hu and Koochesfahani (2002). Thus, the lifetime of the chemical, τ, can be found by two successive images with known delay time ($\Delta t = t_2 - t_1$) and equal exposure time. This lifetime is temperature dependent and can be calibrated against temperature.

Lifetime with ammonium chloride

During initial experimental trials of the solidification process of the ammonium chloride solution, Lum (2001) observed that in the presence of ammonium chloride, the phosphorescent intensity of the MTV Triplex (chemical used in our experiments)

appeared brighter and yielded longer delay times between the undelayed and delayed images. This prompted the investigation of lifetime variation of the MTV chemicals in aqueous ammonium chloride solutions. The lifetime of the MTV Triplex (chemical used here) in the presence of different concentrations of ammonium chloride was determined and the results are shown in Figure D-1. The lifetime is normalized with the lifetime of the chemicals at T = 20° C.

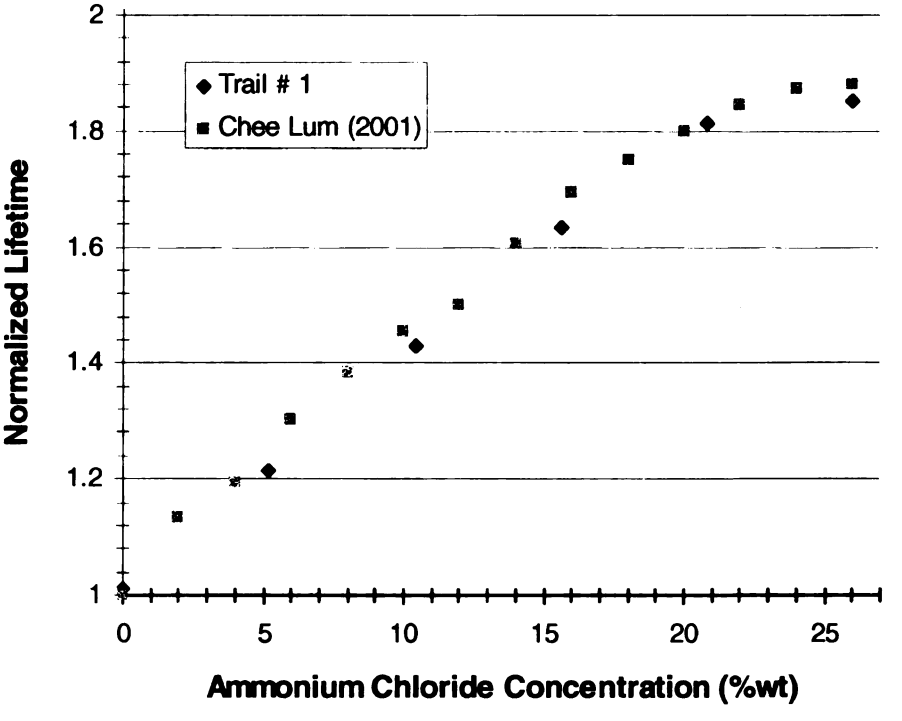

Figure D-1: Normalized lifetime as a function of weight percentage of the ammonium chloride

It can be seen that the lifetime increases significantly by adding ammonium chloride to the solution. The lifetime tapers off at 20% wt and after 22% wt it is almost constant. The lifetime at this point is approximately 6.7 ms. Interestingly, based on the equilibrium phase diagram of ammonium chloride solution, the concentration of the solution never

goes below 21% wt during the solidification process. Therefore, one can conclude that the lifetime of the MTV chemicals is almost independent from the ammonium chloride concentration during the solidification process, which that simplifies the application of MTV&T.

Calibration of the lifetime of MTV Triplex with temperature variation

In order to know if the MTV&T technique could be used to measure velocity and temperature profiles of two phase-locked plumes simultaneously, the lifetime of the MTV Triplex was calibrated with temperature variation. A XeCl excimer ultraviolet (UV) laser (wavelength λ = 308 nm, energy 50 mj/pulse) and appropriate optics were used to illuminate the test section (the same container used in the solidification studies), containing an aqueous solution of 1-BrNp-Gβ-CD-ROH complex, with a laser sheet. The solution was stirred to achieve thermal equilibrium. A thermocouple was placed in the solution to measure the actual temperature. The same camera used in MTV measurement was used here to conduct phosphorescence image recording. To acquire temperature data, the aqueous solution of the 1-BrNp-Gβ-CD-ROH complex was cooled from below. After the thermal equilibrium was established, the phosphorescence lifetime was measured by taking two successive images with a 5 ms delay between them, 500 μs after the laser pulse, and 500 μs exposure time for each image. Then, Equation (D-2) was used to calculate lifetime (t_2-t_1 = 5 ms). Figure D-2 shows the variation of the normalized lifetime with temperature. As can be seen, the sensitivity of the normalized lifetime to temperature in the absence of ammonium chloride was very high (10%$^{o}C^{-1}$). Adding ammonium chloride to the solution reduced this sensitivity significantly. After 22% wt,

the sensitivity ($1.5\%^{o}C^{-1}$) no longer decreased with additional ammonium chloride. Therefore, the maximum sensitivity one can have during the solidification process of ammonium chloride for temperature measurement is $1.5\%\ ^{o}C^{-1}$. This sensitivity is three times less than the LIF technique described in previous chapters. Besides, the intensified cameras (DiCam-Pro) usually have less signal/noise ratio than the non-intensified (Pixelfly) CCD cameras, which were used for the LIF technique.

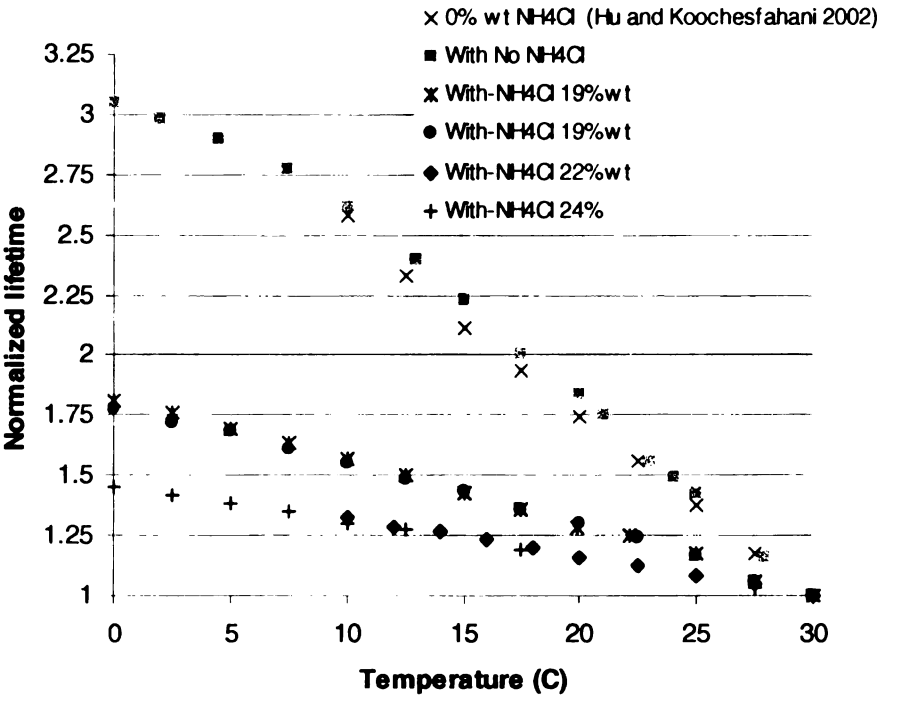

Figure D-2: Variation of normalized lifetime with temperature

MTV&T technique was used to measure the temperature of a plume at t = 25 min. the tagged line was 5 mm above the mushy zone. The delayed time used to take two successive images was 30 ms with 3 ms exposure time for each image. Unfortunately, the measured temperature profile of the plume showed the plume being warmer than the

surroundings. As can be seen in Figure D-3, the intensity of the tagged line in the plume region looks dimmer compared with that of the surroundings. Assuming the intensity of the tagged line in the undelayed image to be uniform and referring to the calibration curve, this

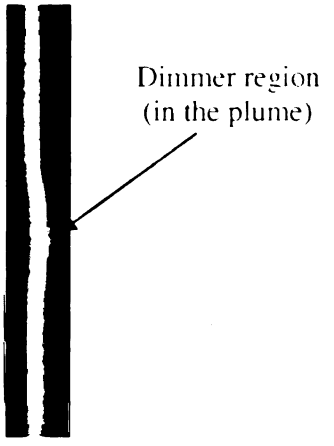

Figure D-3: Delayed image of a line tagged region

means that the lifetime should be shorter in the plume and should look warmer. This discrepancy is because of low sensitivity of the calibration curve to temperature variation ($1.5\%^{\circ}C^{-1}$). Suppose that the concentration of the plume is 3% wt less than that of the surrounding. This will result in 0.1 difference in normalized life time, as seen in Figure D-2 which is a 5% variation in normalized lifetime (0.1/1.8 ×100). Thus, as seen in Figure D-2, the plume will appear $3^{\circ}C$ warmer than what it should be. Unfortunately, 1-BrNp-Gβ-CD-ROH cannot be used in ammonium chloride solution due to its unique characteristics. For implementation of the MTV&T technique in ammonium chloride solution, an alternative chemical needs to be found and studied in the future.

Appendix E

Error Analysis

In two-color LIF technique, the temperature mapping relies on the temperature dependence of fluorescence intensity, estimated from the intensity ratio of two temperature sensitive dyes. The actual value of temperature would correspond to an equivalent $\frac{R_f(T)}{R_f(T_o)}$ value from the calibration profile if the CCD cameras are free of noise. However, due to the noise of the CCD cameras the measured $\frac{R_f(T)}{R_f(T_o)}$ value is not the actual value, and the predicted temperature is not exactly correct. As mentioned before, the fluorescence intensity can be written as a function of the temperature and reference conditions:

$$\ln\left(\frac{R_f(T)}{R_f(T_o)}\right) = (B_1 - B_2)\left(\frac{1}{T} - \frac{1}{T_o}\right) \tag{E-1}$$

the above equation can be rewritten as

$$T = \frac{1}{\frac{1}{\Delta B}\ln\left(\frac{R_f(T)}{R_f(T_o)}\right) + \frac{1}{T_o}} \tag{E-2}$$

The "error" in the $\left(\frac{R_f(T)}{R_f(T_o)}\right)$, associated with the noise of the CCD cameras, will result in an error ΔT, which can be found from $\Delta T = \frac{\partial T}{\partial R_f(T)} \Delta R_f(T) + \text{HOT}$.

Therefore from equation (E-2) one can show that

$$\Delta T = \frac{\frac{1}{\Delta B}\frac{1}{R_f(T)}}{\left(\frac{1}{\Delta B}\ln\left(\frac{R_f(T)}{R_f(T_o)}\right)+\frac{1}{T_o}\right)^2}\Delta R_f(T) \qquad \text{(E-3)}$$

or

$$\frac{\Delta T}{T^2} = \frac{1}{\Delta B}\frac{\Delta R_f(T)}{R_f(T)} \qquad \text{(E-4)}$$

in which ΔB = 2682 K (in this study).

From equation (E-4) one can conclude that 1% variation in intensity ratio ($\frac{\Delta R_f(T)}{R_f(T)}$=1%) at room temperature (T=300 K) will result in ΔT = 0.3 K error in the measured temperature value.